PROBLEMS IN THE STATICS AND DYNAMICS OF NEMATIC LIQUID CRYSTALS

By

S. M. Kamil

The Institute of Mathematical Sciences, Chennai.

A thesis submitted to the
Board of Studies in Physical Sciences

In partial fulfillment of the requirements

For the Degree of

DOCTOR OF PHILOSOPHY

of

HOMI BHABHA NATIONAL INSTITUTE

July 2010

Homi Bhabha National Institute

Recommendations of the Viva Voce Board

As members of the Viva Voce Board, we recommend that the dissertation prepared by **Syed Mohammad Kamil** entitled "Problems in the Statics and Dynamics of Nematic Liquid Crystals" may be accepted as fulfilling the dissertation requirement for the Degree of Doctor of Philosophy.

--- **Date :**
Dean : T. R. Govindarajan

--- **Date :**
Convener : Gautam I. Menon/Sudeshna Sinha

--- **Date :**
Member : M. V. N. Murthy

--- **Date :**
Member : Rajesh Ravindran

--- **Date :**
Member : Ronojoy Adhikari

--- **Date :**
External Examiner : Chandan Dasgupta

Final approval and acceptance of this dissertation is contingent upon the candidate's submission of the final copies of the dissertation to HBNI.

I hereby certify that I have read this dissertation prepared under my direction and recommend that it may be accepted as fulfilling the dissertation requirement.

--- **Date :**
Guide : Gautam I Menon/Sudeshna Sinha

DECLARATION

I hereby declare that the investigation presented in the thesis has been carried out by me. The work is original and the work has not been submitted earlier as a whole or in part for a degree/diploma at this or any other Institution or University.

S. M. Kamil

ACKNOWLEDGEMENTS

Abstract

Liquid crystalline states of matter provide a useful testing ground for statistical mechanical theories of ordered states, since a variety of ordered phases can be accessed in experiments and computer simulations. They also constitute simple model systems for studying the interplay between internal structure and an externally imposed flow, thus illuminating rheological studies of a large class of complex fluids.

In this thesis, we study some problems in the statics and dynamics of nematic liquid crystals. Nematics, typically formed in solution by rod-like molecules with an aspect ratio which deviates sufficiently from unity, exhibit orientational order in the absence of translational order. Such orientational order is quantified through a traceless, symmetric tensor $Q_{\alpha\beta}$. The free energy which quantifies the cost of deformations is the Ginzburg-Landau-de Gennes (GLdG) free energy functional, obtained *via* a gradient expansion in $\mathbf{Q}$.

This thesis studies two broad classes of problems using the GLdG approach. The first class deals with the static properties of the isotropic-nematic interface. The problem of interface structure for the nematic is particularly interesting since it provides a simple illustration of how the structure of an interface can differ substantially from structure in the bulk.

The second class of problems involves the study of the dynamics of $Q_{\alpha\beta}$ for a nematic fluid in an external shear flow. Our study of the dynamics of $Q_{\alpha\beta}$ impacts experiments on the flow behaviour of fluids with orientational order, a prototypical model for the understanding of complex fluid rheology, in particular of chaos associated with unsteady rheological response or "rheochaos". Such rheochaos is a consequence of constitutive and not convective non-linearities, originating in the coupling of the flow to structural or orientational variables describing the local state of the fluid

A powerful approach to understanding complex spatio-temporal dynamics is based on the study of coupled map lattices, a numerical scheme in which maps placed on the sites of a lattice evolve both via local dynamics as well as through couplings to neighbouring sites. However, the utility of this methodology in a specific context is often severely limited by the availability of local maps able to comprehensively describe the spatially uniform case. In this thesis, we discuss this

requirement in the context of a model for rheochaos, proposing a local map as well as a coupled map description of the regular and chaotic states obtained in sheared nematics.

The thesis is organized as follows. In the first chapter, the Introduction, we briefly review the GLdG order parameter theory of the isotropic-nematic transition. We survey the literature which deals with the isotropic-nematic interface and briefly describe methodologies for studying the rheology of complex fluids, in particular nematogenic fluids. The results presented in the chapters which follow are summarized in more detail below, chapterwise. Finally, we end this thesis with a conclusion and point to further work.

Isotropic-Nematic interface with Planar Anchoring

In the second chapter of this thesis we revisit the classic problem of the structure of the isotropic-nematic interface within Ginzburg-Landau-de Gennes theory, refining previous analytic treatments of biaxiality at the interface. We present results for the uniaxial and biaxial profiles, specialized to the case of planar anchoring, showing how a term in the Euler-Lagrange equations neglected in previous work contributes substantially to determining the structure of the interface. We use results from a fast and highly accurate spectral collocation scheme for the solution of the Landau-Ginzburg-de Gennes equations to test these analytic results. In comparison to earlier work, we obtain improved agreement with numerics for both the uniaxial and biaxial profiles, with our results being increasingly accurate as κ is reduced. We also provide accurate asymptotic results for the decay of the S and T order parameters deep into the nematic and isotropic phases.

Isotropic-Nematic Interface with an Oblique Anchoring Condition

In the third chapter of this thesis, we study the case where a general anchoring condition is imposed on the nematic side of the interface, reproducing results of previous work in the limit in which this anchoring condition reduces to the planar or homoeotropic case. Our approach uses variational methods, based on physically motivated and computationally flexible variational profiles for uniaxial and biaxial order, as well as for the variation of the angle between the nematic axis

and the coordinate normal to the interface. Results from our analysis are compared to numerical results obtained from a direct numerical minimization of the Ginzburg-Landau-de Gennes free energy. While spatial variations of the uniaxial and biaxial order parameters are approximately confined to the neighbourhood of the interface, nematic elasticity requires that the director orientation interpolate smoothly between planar anchoring at the location of the interface and the imposed boundary condition at infinity. Our variational results are in close agreement with numerical results as well as results from molecular simulations. Our methods access the nontrivial structure of the biaxiality at the interface including the large tail towards the isotropic side and the change in the sign of the biaxial order parameter across the interface. This approach also captures the inversion of the profile of biaxiality as the elastic coefficient L_2 crosses zero.

Local Map Description of Nematic Liquid Crystals

In chapter four of this thesis, we propose and study a local map capable of describing the full variety of dynamical states, ranging from regular to chaotic, obtained when a nematic liquid crystal is subjected to a steady shear flow. The map is formulated in terms of a quaternion parametrization of rotations of the local frame described by the axes of the nematic director, subdirector and the joint normal to these, with two additional scalars describing the strength of ordering. Our model yields kayaking, wagging, tumbling, aligned and coexistence states, in agreement with previous formulations based on coupled ordinary differential equations. The phase diagram we obtain using our methods contains all non-trivial dynamical states obtained in previous work. Moreover, it closely resembles, even at the quantitative level, phase diagrams obtained in previous work which used ordinary differential equations formulated in continuous time. Our approach makes an extension to the case in which the shear rate is periodically modulated, possible. Our work thus supplies a crucial ingredient required for the construction of coupled map lattice approaches to the spatio-temporal aspects of rheological chaos, a problem currently at the boundaries of our understanding of the dynamics of complex fluids.

A Coupled Map Lattice Model of Rheological Chaos.

In chapter five of this thesis we devise and study a coupled map lattice model for a nematogenic fluid in a passive shear flow. We begin with a local map which contains all the states predicted using a ODE-based methodology. We then couple these maps together spatially, using standard techniques, in one and two dimensions. Our results provide evidence for spatially and temporally uniform states, as well as states which are spatially uniform but temporally periodic. In a restricted regime of parameter space, we find evidence for spatio-temporally chaotic behaviour, which we characterize in detail. We obtain a phase diagram in the space of the coupling constant for the spatial coupling of sites as well as a paramter which enters our map, illustrating how the different spatio-temporal phases are connected to each other. Previous work on rheochaos has been based on methodologies which use partial differential equations, which are then solved (typically in one dimension) in the passive advection approximation. Our results here obtain the same states found in approaches which use PDE's, but allow a numerically tractable extension to two and higher dimensions. Our results for this model indicate that behaviour in the one dimensional and two dimensional cases are qualitatively similar, although the larger number of neighbours in two dimensions suppresses spatial irregularity. We have checked that our results are qualitatively similar for different choices of spatial coupling schemes. Our results include the complete characterization of phases and the phase diagram as well as the demonstration of spatio-temporal intermittency in this system. More centrally, our work shows that coupled map lattice models of rheological chaos can provide accurate yet computationally tractable descriptions of the steady state behaviour of driven complex fluids.

List of publications/preprints

1. **Regular and Chaotic States in a Local Map description of Nematic Liquid Crystals**,
   S.M. Kamil, Sudeshna Sinha and Gautam I. Menon, *Physical Review E* **78**, 011706(2008).
   (arXiv:0801.3876v2)

2. **Biaxiality at the Isotropic-Nematic Interface with Planar Anchoring.**

S. M. Kamil, A. K. Bhattacharjee, R. Adhikari and Gautam I. Menon

Phys. Rev. E **80**, 041705(2009)

(http://arxiv.org/abs/0906.2899)

3 **The isotropic-nematic interface with an oblique anchoring condition.**

S. M. Kamil, A. K. Bhattacharjee, R. Adhikari and Gautam I. Menon

The Journal of Chemical Physics, **131**, 174701(2009)

(http://arxiv.org/abs/0908.2517)

4 **A Coupled Map Lattice Model for Rheological Chaos in Sheared Nematic Liquid Crystals.**

S.M. Kamil, Gautam I. Menon and Sudeshna Sinha

Chaos **20** 043123 (2010)

(http://arxiv.org/abs/1005.2041)

Contents

II Lattice Models For Rheological Chaos in Sheared Nematics 51

List of Figures

List of Tables

Part I

Biaxiality at the Isotropic-Nematic Interface

1

Introduction

1.1   Soft Matter Systems

Soft condensed matter physics deals with systems in which characteristic energy scales for some classes of structural deformations are comparable to $k_B T$. Such systems include colloids, polymer solutions, emulsions, foams, surfactant solutions, powders and a several other examples. The following materials familiar from daily life qualify as soft condensed matter: polymer gels (Jello), emulsions (mayonnaise), viscoelastic detergent solutions (shampoo), fat crystal networks (margarine), concentrated colloids (paint), polymer solutions (multigrade engine oil) and lyotropic liquid crystals (such as the slime created when a bar of soap is left in a pool of water).

Liquid crystals constitute an extensively studied example of soft matter. The liquid-crystalline state of matter is a state intermediate between a crystalline solid and a liquid. This state of matter has been the subject of much research since its discovery by the Austrian botanist Reinitzer at the end of 19th century. Apart from its technological importance in devices and displays, the study of liquid crystals has stimulated considerable progress in the understanding of subjects as diverse as the rheological behaviour of complex fluids, the existence of novel defect states, the presence of unusual orders and many others. Nematic liquid crystals, typically formed in suspensions of rod-like molecules whose aspect ratio deviates sufficiently from unity, exhibit orientational order in the absence of translational order[39, 25, 78]. An example of a molecule which exhibits a liquid crystalline phase is shown in Fig. 1.1, together with its phase diagram. Liquid crystals can be divided into
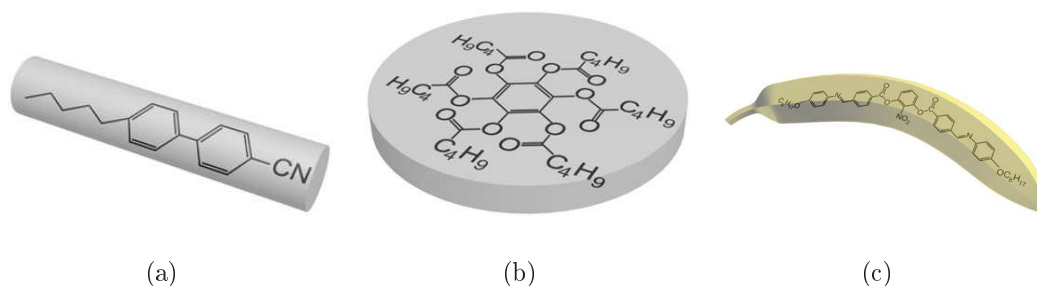
Figure 1.1: (a) Molecular structure of 5CB, (b) Benzene-hexa-n-alkanoate derivatives, (c) Banana-shaped molecules. Figure adapted from
http://dept.kent.edu/spie/liquidcrystals/maintypes.html
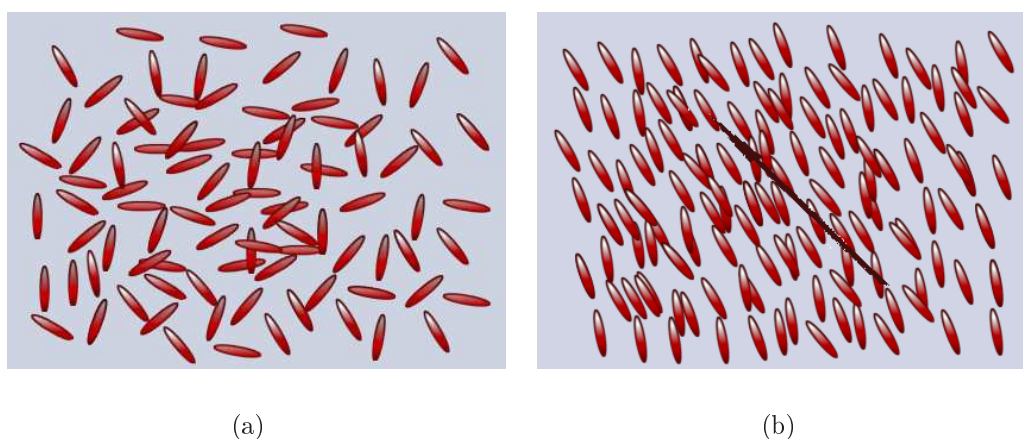
Figure 1.2: (a) Isotropic and (b) nematic phases of anisotropic molecules

lyotropic and *thermotropic*, depending on the parameter whose variation drives the phase transition. In lyotropic systems, such as a hard rod mixture, the variable is the concentration, whereas in the thermotropic case, illustrated in Fig. 1.2, the tunable variable is the temperature.

Liquid crystals are composed of long, rod-like molecules. In the isotropic fluid phase, the orientation and positions of molecules are random. In the nematic phase, the positions of molecules are still random, but their long axes are oriented, on average, along a specific direction specified by a unit vector **n** called the **director**. Nematics are often conveniently idealized as being composed of molecules which are up-down symmetric. Thus, a vector order parameter appropriate for describing, say, a spin system, is inappropriate here, since only an axis is picked out in the

nematically ordered state and not a direction *i.e.* the state has the symmetry $\mathbf{n} \equiv -\mathbf{n}$. Since the order parameter must be covariant under changes of coordinate system used to describe it, it must transform as a scalar, vector or tensor quantity.

In Fig. 1.4 the distribution of the long axis of the molecule ν is shown. The long axis is confined within the cones AOB and $A'OB'$. The average distribution of the long axis is along the z axis, defining the director $\hat{\mathbf{n}}$. Since the molecule has up-down symmetry $-\hat{\mathbf{n}}$ is an equivalent choice. Thus the order parameter describing this phase should be invariant with respect to $\hat{\mathbf{n}}$ going to $-\hat{\mathbf{n}}$.

The z component of the long axis of the molecules ν as shown in Fig. 1.4(a), is equal to $\cos\vartheta$, where ϑ is the angle between the Z axis and the vector ν. If the projection of the molecule on the XY plane makes an angle ϕ from the X axis, the other two components ν_x and ν_y are given by $\sin\vartheta\cos\phi$ and $\sin\vartheta\sin\phi$ respectively. The state of the alignment of the rods can be described by a distribution function $f(\vartheta,\phi)\, d\Omega$ giving the probability of finding an orientation of the rod within a small solid angle $d\Omega = \sin\vartheta\, d\vartheta\, d\phi$ around the direction $(\vartheta,\ \phi))$.

The distribution of the projection of the long axis of molecules on th XY plane may be asymmetric about the Z axis, as shown in Fig. 1.4(c). In this case one can associate one more vector $\hat{\mathbf{m}}$ along the maximum of the distribution of the projections, shown by the line MM' in Fig. 1.4(c). This phase is called a biaxial phase. For a rod-like molecule which is symmetric about its long axis, this is not an allowable distribution in the absence of any symmetry breaking. However, such a distribution function obtains in the presence of suitable external fields such as the magnetic field or a flow field which introduces an additional direction into the problem, breaking orientational symmetry about the director axis. In the case of molecules which have an extra axis, such as the block-shaped molecules shown at the bottom of Fig. 1.4, a biaxial phase can be obtained in the absence of such fields.

If this distribution is symmetric, then the distribution function $f(\vartheta,\ \phi) \equiv f(\vartheta)$ does not depend on ϕ. From the up-down symmetry of the molecule, $f(\vartheta) = f(\pi - \vartheta)$.

While the most complete characterization of the orientational order uses the full function $f(\vartheta)$, it can also be specified using one or a few of the moments of

(a)   (b)
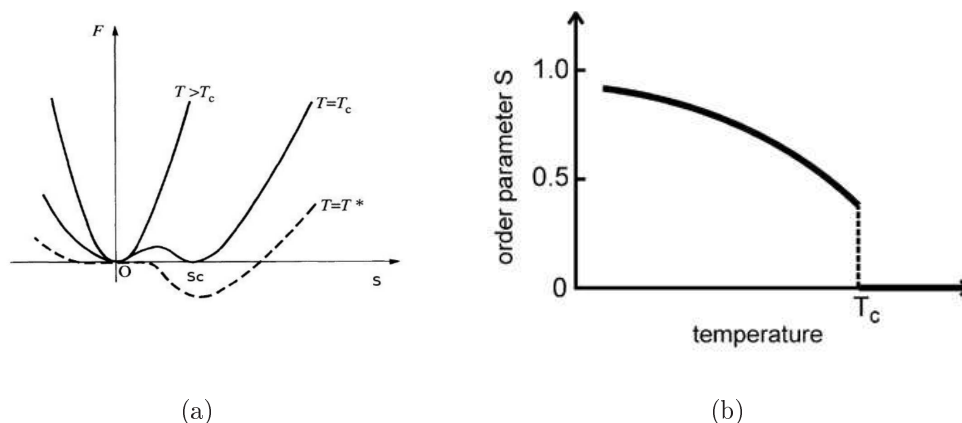
Figure 1.3: Schematic of (a) Free energy as a function of the scalar order parameter at different temperatures above and below the isotropic-nematic transition and (b) Scalar order parameter minimizing the free energy as a function of temperature.

this distribution function. The first idea would be to use the average

$$\langle \cos \vartheta \rangle = \langle \nu.\hat{\mathbf{n}} \rangle = \int f(\vartheta) \cos \vartheta \, d\Omega, \tag{1.1}$$

However, since $f(\vartheta) = f(\pi - \vartheta)$ the integral vanishes identically and there is no dipole moment. The first multipole which gives a non-trivial answer is the quadrupole, $i.e.$

$$S = \frac{1}{2} \langle (3 \cos^2 \vartheta - 1) \rangle = \int f(\vartheta) \frac{1}{2} (3 \cos^2 \vartheta - 1) \, d\Omega \tag{1.2}$$

If $f(\vartheta)$ is strongly peaked around $\vartheta = 0$ and $\vartheta = \pi$ (all the molecules are parallel), $\cos \vartheta = \pm 1$ and $S = 1$. If $f(\vartheta)$ is strongly peaked around $\vartheta = \pi/2$ (all the molecules are perpendicular to Z axis), $S = -\frac{1}{2}$. In the isotropic case the orientation is random. Hence, $f(\vartheta)$ is independent of ϑ and the average value of $\cos^2 \vartheta = \frac{1}{3} \Rightarrow S = 0$. Thus S is a parameter which can characterize the nematic and isotropic phases separately.
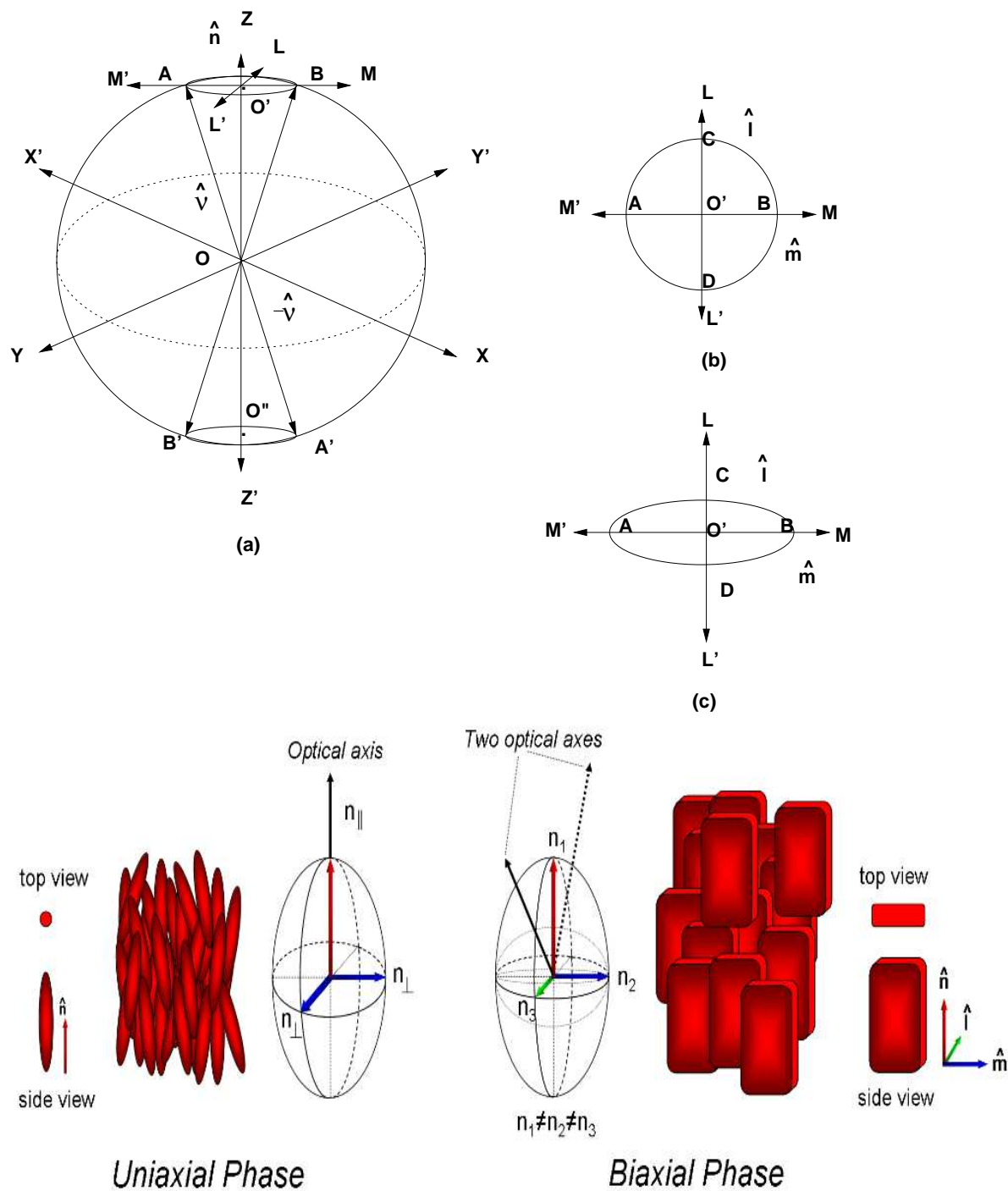
Figure 1.4: (a) Distribution of molecular orientation on the unit sphere, (b) Distribution function for a uniaxial nematic (c) Distribution function for a biaxial nematic. Bottom figure shows examples of molecules showing uniaxial and biaxial phases. (Bottom figure taken from M. Lehmann and J. Seltmann, Beilstein J. Org. Chem. 2009, 5, No. 73. doi:10.3762/bjoc.5.73)

1.2   Order Parameter Description of Nematics

In its most general form, the order parameter of a liquid crystal is given by

$$Q_{ij} = \frac{V}{N} \sum_{\alpha=1}^{N} (\nu_i^\alpha \nu_j^\alpha - \frac{1}{3}\delta_{ij})\delta(\mathbf{x} - \mathbf{x}^\alpha), \tag{1.3}$$

where ν^α is an unit vector pointing along the long axis of the molecule α, located at the location $\mathbf{x}^\alpha$, V is the total volume and N is the total number of molecules. By definition the order parameter is symmetric and trace less. In a co-ordinate system with one axis along the director the matrix is diagonal

$$\langle \mathbf{Q} \rangle = \begin{pmatrix} \frac{2}{3}s & 0 & 0 \\ 0 & -\frac{1}{3}s + \eta & 0 \\ 0 & 0 & -\frac{1}{3}s - \eta \end{pmatrix} \tag{1.4}$$

If η is nonzero, $\langle \mathbf{Q} \rangle$ is biaxial and there are two preferred directions.

We can reparameterise the $\mathbf{Q}$ in the following way

$$\langle \mathbf{Q} \rangle = \begin{pmatrix} S & 0 & 0 \\ 0 & -\frac{1}{2}(S - T) & 0 \\ 0 & 0 & -\frac{1}{2}(S + T) \end{pmatrix} \equiv \frac{3}{2}S(\mathbf{nn} - \frac{1}{3}\mathbf{I}) + \frac{1}{2}T(\mathbf{mm} - \mathbf{ll}) \tag{1.5}$$

If $T = 0$ the system is uniaxial, with a principal axis of alignment $\mathbf{n}$, and $S = \frac{2}{3}\langle P_2(\cos\theta) \rangle$. For $T \neq 0$ the system is biaxial, with $\mathbf{m}$ and $\mathbf{l}$ the major and minor axes of alignment in the plane normal to $\mathbf{n}$.

1.3   Ginzburg-Landau Description of the Isotropic-Nematic Transitions

The description of the early stages of phase-ordering upon quenches from the isotropic phase, the properties of nematic droplets within the isotropic phase and the structure of the isotropic-nematic interface are all problems which require that nematic and isotropic phases be treated within the same framework. The inhomogeneous order parameter configurations obtained in these cases are weighted by

the Ginzburg-Landau-de Gennes (GLdG) free energy, obtained *via* a gradient expansion in $\mathbf{Q}$ in which only low-order symmetry allowed terms are retained[39, 38].

To construct the GLdG free energy, we enumerate the symmetries of the problem.

1.3.1 Symmetries

Two relevent symmetries of the problem are

1. (Lack of) Inversion symmetry. Consider a uniaxial state:

$$\mathbf{Q} = \begin{pmatrix} S & 0 & 0 \\ 0 & -\frac{1}{2}S & 0 \\ 0 & 0 & -\frac{1}{2}S \end{pmatrix} \quad \text{(Prolate uniaxial)} \qquad (1.6)$$

Under change of sign

$$-\mathbf{Q} = \begin{pmatrix} -S & 0 & 0 \\ 0 & \frac{1}{2}S & 0 \\ 0 & 0 & \frac{1}{2}S \end{pmatrix} \quad \text{(oblate uniaxial)} \qquad (1.7)$$

Hence the degree of order is qualitatively different under the transformation $\mathbf{Q} \to -\mathbf{Q}$, thus permitting odd invariants in the free energy.

2. In a homogeneous and isolated system the direction of nematic director is arbitrary. This implies that the free energy is rotationally invariant. Because $\mathbf{Q}$ is a dyad of unit vectors which rotate as usual, it behaves like a tensor under rotation.

$$Q_{\alpha\beta} \to R_{\alpha\lambda}R_{\beta\rho}Q_{\lambda\rho} \qquad (1.8)$$

For this transformation the free energy should remain invariant. For a 3D tensor $\mathbf{Q}$, there are two non-trivial invariants, $Tr\mathbf{Q}^2$ and $Tr\mathbf{Q}^3$.

1.3.2 Free Energy

With the above symmetries and invariants, the free energy is

$$f_L = \frac{1}{2}A(t - T^*)\, Tr\mathbf{Q}^2 + \frac{1}{3}B\, Tr\mathbf{Q}^3 + \frac{1}{4}C\, (Tr\mathbf{Q}^2)^2 \qquad (1.9)$$

8

Inserting the general form of **Q**, Eq. (1.22).

$$f_L = F_1 + F_2 \tag{1.10}$$

with

$$F_1 = \frac{3}{4}A(t - T^*) \; S^2 + \frac{1}{4}B \; S^3 + \frac{9}{16}C \; S^4 \tag{1.11}$$

$$F_2 = \frac{1}{4}T^2[A(t - T^*) - 2B \; S + \frac{1}{6}C \; T^2] + \frac{1}{16}C \; T^4 \tag{1.12}$$

$$f_L = \frac{3}{4}A(t - T^*) \; S^2 + \frac{1}{4}B \; S^3 + \frac{9}{16}C \; S^4 + \frac{1}{4}T^2[A(t - T^*) - 2B \; S + \frac{1}{6}C \; T^2] + \frac{1}{16}C \; T^4 \tag{1.13}$$

For equilibrium one has to find the minima of f_L as a function of S and T. F_1 gives minima at $t > T^*$, for $B \; S$ negative and $T = 0$, due to the cubic term. With these conditions F_2 is positive, so the system is stable for $T \neq 0$. It is, in fact, a uniaxial state. Considering $T = 0$ and minimising with respect to S, we obtain

$$\left(\frac{\partial F_1}{\partial S}\right)_{T=0} = 0 \rightarrow S_c = \begin{cases} 0 \\ \frac{1}{3C}(-B + \sqrt{B^2 - 24A \; C}) \end{cases} \tag{1.14}$$

On lowering the temperature, the free energies of the isotropic and uniaxial state become equal at S_c. At this point the system makes a first order phase transition to the nematic state. The values are

$$S_c = -\frac{2B}{9C}, \quad \Delta t = T_{IN} - T^* = \frac{B^2}{27AC} \tag{1.15}$$

1.4 The Ginzburg-Landau-de Gennes Approach to the Isotropic-Nematic Transition

To recapitulate, nematic order is quantified through a traceless, symmetric tensor $Q_{\alpha\beta}$ defined at every point in space[39, 53]. In the (biaxial) nematic phase, the order parameter is

$$Q_{\alpha\beta} = \frac{3S}{2}\left(n_\alpha n_\beta - \frac{1}{3}\delta_{\alpha\beta}\right) + \frac{T}{2}(l_\alpha l_\beta - m_\alpha m_\beta) \tag{1.16}$$

where the director $\mathbf{n}$ is defined as the normalized eigenvector corresponding to the largest eigenvalue of $\mathbf{Q}$, the subdirector $\mathbf{l}$ is associated with the sub-leading eigenvalue, and their mutual normal $\mathbf{m}$ is obtained from $\mathbf{n} \times \mathbf{l}$. The quantities S and T represent the strength of uniaxial and biaxial ordering: $|S| \neq 0$, $T = 0$ is the uniaxial nematic whereas $S, T \neq 0$ with $T < 3S$ defines the biaxial case[39]. The biaxial nematic arises when the molecule has two distinct axes of symmetry. Alternatively, it can also arise when an additional direction, such as that imposed by a shear flow, is imposed on the system, even for molecules which are uniaxially symmetric.

The Ginzburg-Landau-de Gennes free energy functional $F = F_h + F_{el}$ [38] is obtained from a local expansion in powers of rotationally invariant combinations of the order parameter $\mathbf{Q}(\mathbf{x}, t)$,

$$\mathcal{F}_h[\mathbf{Q}] = \frac{1}{2} A \, Tr\mathbf{Q}^2 + \frac{1}{3} B \, Tr\mathbf{Q}^3 + \frac{1}{4} C \, (Tr\mathbf{Q}^2)^2 + E' \, (Tr\mathbf{Q}^3)^2 \ldots, \qquad (1.17)$$

The restriction to the terms shown above are sufficient to yield a first-order transition between isotropic and nematic phases as well as a stable biaxial phase, obtained when $E' \neq 0$[53].

To this local free energy, non-local terms arising from rotationally invariant combinations of gradients of the order parameter must be added. The choice of the following two lowest-order gradient terms is common[38, 104, 105]:

$$\mathcal{F}_{el}[\partial \mathbf{Q}] = \frac{1}{2} L_1 (\partial_\alpha Q_{\beta\gamma})(\partial_\alpha Q_{\beta\gamma}) + \frac{1}{2} L_2 (\partial_\alpha Q_{\alpha\beta})(\partial_\gamma Q_{\beta\gamma}), \qquad (1.18)$$

where α, β, γ denote the Cartesian directions in the local frame, and L_1 and L_2 represent the elastic cost for distortions in $\mathbf{Q}$[53]. The fact that there are only two terms which appear to this order implies that only two of the three Frank constants are independent. The limit in which $L_2 = 0$, or of zero elastic anisotropy corresponds to the case in which all Frank constants are equal. The relationship between L_1 and L_2 and the Frank constants K_1, K_2 and K_3 are the following: $K_1 = K_3 = 9/4(2L_1 + L_2)S^2$ and $K_2 = 9/2L_1S^2$[39, 53]. Note that $\kappa = L_2/L_1$ negative is allowed, although $\kappa < 1.5$ must be satisfied to ensure positivity of the elastic constants. be satisfied to ensure positivity of the elastic constants. The Frank constants are the elastic constants for a liquid crystal which account for the

free energy penalty for creating an inhomogeneous director configuration. K_1 is related to the twist of the nematic director, *i.e.* configurations in which neighboring molecules are forced to be angled with respect to one another, rather than aligned. K_2 is related to splay, where bending occurs perpendicular to the director and K_3 is related to bend of the material. These constants are named after *Frederick Charles Frank*, who pioneered the elastic continuum theory of liquid crystals.

In the free energy density of Eq. 1.17, $A = A_0(1 - T/T^*)$, where T^* denotes the temperature that represents the limit of supercooling in mean field theory. From the inequality $\frac{1}{6}(Tr\mathbf{Q}^2)^3 \geq (Tr\mathbf{Q}^3)^2$, higher powers of $Tr\mathbf{Q}^3$ can be excluded for the description of the uniaxial phase. Thus the uniaxial case is described by $E' = 0$ whereas $E' \neq 0$ for the biaxial phase. We will assume that $E' = 0$, thus ensuring that the stable ordered phase is the uniaxial nematic. For nematic rod-like molecules $B < 0$ whereas for disc-like molecules, $B > 0$; for concreteness, we will assume $B < 0$ here. The quantity C must be positive to ensure stability and boundedness of the free energy in both the isotropic and nematic phases.

1.5   Properties of the Isotropic-Nematic Transition

The first order isotropic to uniaxial nematic transition at the critical value $S = S_c$ is thus obtained from,

$$A \;=\; \frac{3}{4}CS_c^2 \tag{1.19}$$

$$B \;=\; -\frac{9}{2}CS_c. \tag{1.20}$$

We have chosen the values $B = -0.5, C = 2.67$ and $A = B^2/27C$, thus enforcing phase coexistence between an isotropic and uniaxial nematic phase [53], in our discussion for the isotropic-nematic interface.

1.6   Anchoring at Surfaces and Interfaces

Nematic ordering is strongly influenced by confining walls and surfaces, which impose a preferred orientation or "anchoring condition" on the nematic state. Such a preferred orientation yields an anchoring angle, defined as the angle made by the

director in the immediate neighbourhood of the surface with the surface normal. Anchoring normal to the surface is termed as homoeotropic, whereas anchoring in the plane of the surface is termed as planar. The general case is that of oblique anchoring.

As is the case with surfaces, the interface between a nematic and its isotropic phase can also favour a particular anchoring. The problem of interface structure for the nematic is particularly interesting since it illustrates how the structure in the interfacial region can differ substantially from structure in the bulk. It is known, for example, that a region proximate to the interface can exhibit biaxiality within the LGdG theory, even if the stable nematic phase is pure uniaxial[105], provided planar anchoring is enforced. Such biaxiality is absent if the anchoring is homoeotropic[38]. These two limits, of homoeotropic and planar anchoring, lead to interface profiles of S and T which vary only in the vicinity of the interface, as well as orientations which are uniform across the interface[38].

Can oblique anchoring be stabilized, within GLdG theory, at the interface between a bulk uniaxial nematic and its isotropic phase? Suppose we introduce boundary conditions that impose a specified oblique orientation deep into the nematic phase, where the magnitude of the order parameter is saturated. The question, then, is whether such an imposed orientation is relaxed to a preferred value in the vicinity of the interface. The difficulties with this problem stem from the fact that changes in the local frame orientation on the nematic side of the interface come with an elastic cost arising out of nematic elasticity. This is an effect sensitive, in principle, to system dimensions, since gradients can be smoothed out by allowing the changes to occur over the system size. While this cost can be reduced by suppressing the order parameter amplitudes in regions where order parameter phases vary strongly, the precise way in which this might happen, if at all, is an open question.

1.7 The Isotropic-Nematic Interface

1.7.1 Previous Work

The isotropic-nematic transition is weakly first order. Hence, it is reasonable that its central features can be adequately explained by Landau-de Gennes theory

[24]. The study of the isotropic-nematic interface was initiated in an insightful paper by de Gennes, who introduced a simple uniaxial ansatz for the tensor order parameter $Q_{\alpha\beta}$ which describes nematic order [38]. The de Gennes ansatz is exact in the absence of elastic anisotropy. However, the description of the interface in the presence of such anisotropy poses a formidable analytic and numerical problem, since the partial differential equations for the five independent components of $Q_{\alpha\beta}$ contain non-linear couplings, while $Q_{\alpha\beta}$ is itself constrained by symmetry and the requirement that its trace vanish.

Popa-Nita, Sluckin and Wheeler (PSW) [105] studied the I-N interface incorporating elastic anisotropy in the limit of planar anchoring, adapting a parametrization introduced by Sen and Sullivan[119]. In this parametrization, the principal axes of $Q_{\alpha\beta}$ remain fixed in space, and the problem reduces to the solution of two coupled non-linear partial differential equations in the dimension perpendicular to the interface. These equations represent the variation of the amplitude of uniaxial and biaxial ordering across the interface. PSW showed that the solutions of these equations exhibited biaxiality in a region about the interface [105]. The uniaxial order parameter (S) was adequately represented by a tanh profile, as in the original calculation of de Gennes, while the biaxial order parameter (T) exhibited more complex behaviour, peaking towards the isotropic side and with a trough on the nematic side. The biaxial profile was also shown to have a long tail towards the isotropic side, a feature hard to anticipate on physical grounds.

Popa-Nita, Sluckin and Wheeler (PSW)[105] also commented on the case of oblique anchoring, studying this problem numerically within a GLdG approach. They used a set of variables η_s and μ_s introduced in Ref. [119]. Although the focus of their study was the emergence of biaxiality at the interface with a planar anchoring condition, PSW remarked, based on their numerical studies, that if the asymptotic orientation of the director in the nematic phase was set to any value other than 90° (planar anchoring) or 0 (homoeotropic anchoring) for large z, then η_s and μ_s approached this value with non-zero slope. PSW thus concluded that there could be no stable anchoring if the orientation of the director in the nematic phase was neither planar nor homoeotropic, but oblique. The precise nature of the resulting state obtained upon applying an oblique anchoring condition was not addressed by PSW[104, 105].

Density functional calculations on hard-rod systems using Onsager's theory ap-

plied to the free isotropic-nematic interface indicate that the minimum surface free energy is obtained when the rods lie parallel to the isotropic-nematic interface, the case of planar anchoring[91, 5]. Molecular simulations of a system of hard ellipsoids, in which an anchoring energy fixes the director orientation in the nematic phase at a variety of angles, indicate that the isotropic-nematic interface favours planar anchoring. These simulations, and a mean-field calculation based on the Onsager functional, find that the angle profile is approximately linear as one moves away from the boundary condition imposed by the wall at one end of the simulation box[134, 129]. These results, in particular concerning the stability of planar anchoring, are consistent with those from other treatments[12, 32, 31, 4, 130]. However, several other papers indicate specific regimes in which homoeotropic or oblique anchoring may be stable. Moore and McMullen[94] numerically evaluate the inhomogeneous grand potential within a specific approximation scheme finding that planar anchoring is preferred at the interface for long spherocylinders, but oblique or homoeotropic anchoring may be an energetically favourable alternative for smaller aspect ratios. Holyst and Poniewierski study such hard spherocylinders in the Onsager limit, noting that oblique anchoring is favoured over a considerable range of aspect ratios[63]. Finally, experiments provide evidence for both oblique[46] and planar anchoring[86], with electrostatic effects possibly favouring oblique anchoring.

1.7.2   Results of this thesis: Static Behaviour

In Chapter 2 we extend the calculation of biaxiality in the case of planar anchoring in several new ways. First, we show that terms dropped by PSW in their simplification of the Ginzburg-Landau-de Gennes (GLdG) equations are, in fact, comparable in magnitude to the terms they retain, especially for small values of $\kappa = L_2/L_1$, the ratio of the coefficients of the two lowest-order gradient terms in the GLdG expansion. Thus, a more accurate treatment of the interface requires that these terms be retained. The resulting equations have closed form solutions in terms of hypergeometric functions. We show that such solutions provide a better description of the numerical data than the original calculation of PSW. We benchmark our analytic results through an accurate numerical procedure, based on a Chebyshev polynomial expansion, for the study of these equations.

In the third chapter we present numerical and analytic results for uniaxial and biaxial orders at the isotropic-nematic interface within Ginzburg-Landau-de Gennes theory, in the situation where an oblique anchoring condition is imposed asymptotically on the nematic side of the interface, reproducing results of previous work when this condition reduces to planar or homeotropic anchoring. We construct physically motivated and computationally flexible variational profiles for uniaxial and biaxial orders, comparing our variational results to numerical results obtained from a minimization of the Ginzburg-Landau-de Gennes free energy. While spatial variations of the scalar uniaxial and biaxial order parameters are confined to the neighborhood of the interface, nematic elasticity requires that the director orientation interpolate linearly between either planar or homeotropic anchoring at the location of the interface and the imposed boundary condition at infinity. The selection of planar or homeotropic anchoring at the interface is governed by the sign of the Ginzburg-Landau-de Gennes elastic coefficient L_2. Our variational calculations are in close agreement with our numerics and agree qualitatively with results from density functional theory and molecular simulation.

1.7.3   A Note Concerning Conventions

As mentioned earlier, we parameterise the $\mathbf{Q}$ order parameter in the following way

$$\langle \mathbf{Q} \rangle = \begin{pmatrix} S & 0 & 0 \\ 0 & -\frac{1}{2}(S-T) & 0 \\ 0 & 0 & -\frac{1}{2}(S+T) \end{pmatrix} \equiv \frac{3}{2}S(\mathbf{nn} - \frac{1}{3}\mathbf{I}) + \frac{1}{2}T(\mathbf{mm} - \mathbf{ll}) \quad (1.21)$$

The quantities S and T are related to the amounts of uniaxial and biaxial order respectively. We will follow this labeling convention in Chapters 2 and 3 which follow.

However, an alternative labeling convention is often used, in terms of which

$$\langle \mathbf{Q} \rangle = \begin{pmatrix} s_1 & 0 & 0 \\ 0 & -\frac{1}{2}(s_1-s_2) & 0 \\ 0 & 0 & -\frac{1}{2}(s_1+s_2) \end{pmatrix} \equiv \frac{3}{2}s_1(\mathbf{nn} - \frac{1}{3}\mathbf{I}) + \frac{1}{2}s_2(\mathbf{mm} - \mathbf{ll}) \quad (1.22)$$

Here s_1 and s_2 replace S and T notationally, while retaining the same physical

meaning. This convention is used in Chapters 5 and 6, in conformity with the vast literature on the dynamics of nematic liquid crystals. The use of each convention should be clear from the context.

Biaxiality at the Isotropic-Nematic Interface with Planar Anchoring

2.1 The de Gennes result for the Nematic-Isotropic interface

Assuming that biaxiality was absent and that the orientation of the director remained fixed across the interface, de Gennes provided a comparison of the free energy for the cases of planar and homeotropic anchoring. In both the cases one can write the free energy as follows.

$$F_{P,H} = \int_{-\infty}^{\infty} dz \left[F_b + \xi_{P,H}^2 \left(\frac{dS}{dz} \right)^2 \right], \tag{2.1}$$

where the subscripts P and H denote planar and homeotropic anchoring respectively, and F_b is the bulk free energy in both cases. We have $\xi_P^2 = \frac{3}{4}(3L_1 + \frac{1}{2}L_2)$ and $\xi_H^2 = \frac{3}{4}(3L_1 + 2L_2)$ For $L_2 > 0$, $\xi_P < \xi_H$. Minimizing the above equation

$$2\xi_{P,H}^2 \frac{d^2S}{dz^2} = \frac{\partial F_b}{\partial S}. \tag{2.2}$$

This equation has a first integral given by

$$\xi_{P,H}^2 \left(\frac{dS}{dz} \right)^2 = F_b(S) \tag{2.3}$$

The integration constant must vanish, since both dS/dz and F_b are zero far from the transition layer. Inserting this result into Eq. 2.1, we get

$$F_{P,H} = 2 \int_{-\infty}^{\infty} \xi_{P,H}^2 \frac{dS}{dz} dS = 2\xi_{P,H} \int_0^{S_c} [F_b(S)]^{1/2} \ dS \qquad (2.4)$$

Thus, $\xi_P < \xi_H \Rightarrow F_P < F_H$. de Gennes was able thus to calculate which anchoring would prevail under the appropriate conditions.

2.2 Equation for Isotropic-Nematic Interface with Planar anchoring

We begin with the GLdG expansion of the free energy for a general $Q_{\alpha\beta}$

$$\begin{aligned}
\mathcal{F} &= \int dz d\mathbf{x}_\perp [\frac{1}{2} A Tr \mathbf{Q}^2 + \frac{1}{3} B Tr \mathbf{Q}^3 + \frac{1}{4} C (Tr\mathbf{Q}^2)^2 \\
&\quad + \frac{1}{2} L_1 (\partial_\alpha Q_{\beta\gamma})(\partial_\alpha Q_{\beta\gamma}) + \frac{1}{2} L_2 (\partial_\alpha Q_{\alpha\gamma})(\partial_\beta Q_{\beta\gamma})].
\end{aligned} \qquad (2.5)$$

Here A, B and C are expansion parameters, while L_1, L_2 are elastic constants. We choose $B = -0.5, C = 2.67$ and $A = B^2/27C$, thus enforcing phase coexistence between an isotropic and uniaxial nematic phase [53]. The interface is taken to be flat and infinitely extended in the $x - y$ plane. The spatial variation of the order parameter only occurs along the z direction[119]. We scale $Q_{\alpha\beta} \to Q_{\alpha\beta}/S_c$ where $S_c = -\frac{2B}{9C}$, $\mathcal{F} \to \frac{16}{9CS_c^4}\mathcal{F}$, and measure lengths in units of $l_c = \sqrt{54C(L_1 + 2L_2/3)/B^2}$; we choose $L_1 = 10^{-6}$ in our numerics and obtain L_2 from our choice of κ. In the case of planar anchoring, the ordering at infinity is purely uniaxial and taken to be along the x axis. In this case, as shown by Sen and Sullivan, uniaxial and biaxial order vary only with z and the principal axes of the $\mathbf{Q}$ tensor remain fixed in space. The form of $\mathbf{Q}$ is then

$$\mathbf{Q} = \begin{pmatrix} S & 0 & 0 \\ 0 & \frac{1}{2}(-S + T) & 0 \\ 0 & 0 & -\frac{1}{2}(S + T) \end{pmatrix}. \qquad (2.6)$$

Inserting this form of $\mathbf{Q}$ into the free energy and performing the minimization
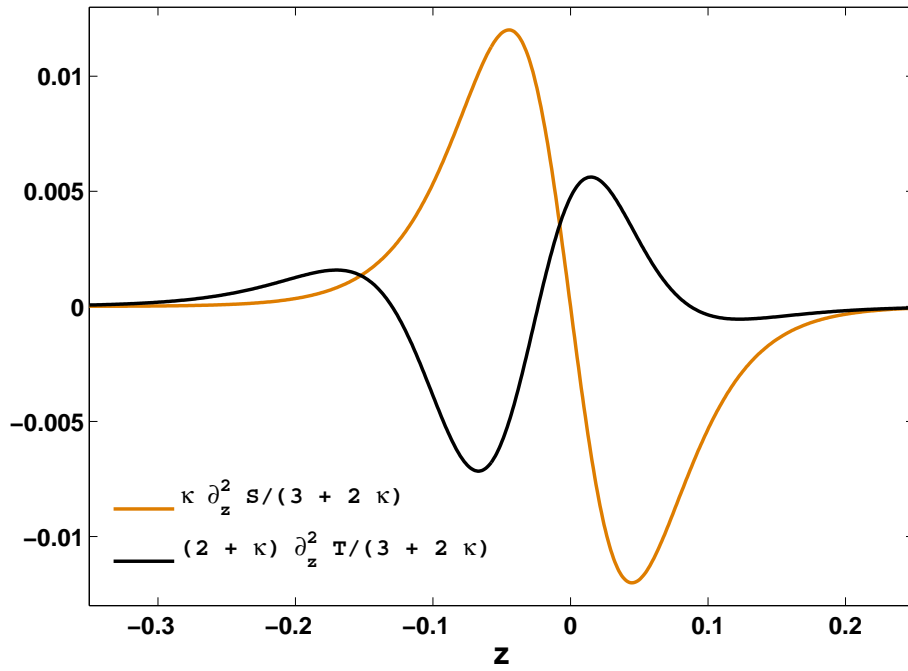
Figure 2.1: A comparison of the terms $\frac{(2+\kappa)}{(3+2\kappa)}\partial_z^2 T$ (dark line) and $\frac{\kappa}{(3+2\kappa)}\partial_z^2 S$ (light line) obtained within the PSW solution to the GLdG equations, for a κ value of 18.0. The PSW approximation consists of ignoring the $\frac{(2+\kappa)}{(3+2\kappa)}\partial_z^2 T$ term in comparison to the $\frac{\kappa}{(3+2\kappa)}\partial_z^2 S$ term. Both terms, however, are of comparable magnitude.

yields [105]

$$\frac{(6+\kappa)}{(3+2\kappa)}\partial_z^2 S + \frac{\kappa}{(3+2\kappa)}\partial_z^2 T \;=\; 4S - 12S^2 + 8S^3 + 4T^2 + \frac{8ST^2}{3}, \quad (2.7)$$

$$\frac{\kappa}{(3+2\kappa)}\partial_z^2 S + \frac{(2+\kappa)}{(3+2\kappa)}\partial_z^2 T \;=\; \frac{4}{3}T + 8ST + \frac{8T^3}{9} + \frac{8S^2T}{3}. \qquad (2.8)$$

Popa-Nita, Sluckin and Wheeler now make several approximations to Eqs. 2.7 and 2.8 to solve them. First, in Eq. 2.7, all terms in T are dropped, since S is typically much larger than T. The resulting equation for S is solved by the tanh function. In Eq. 2.8, PSW drop the $\frac{(2+\kappa)}{(3+2\kappa)}\partial_z^2 T$ term while retaining $\frac{\kappa}{(3+2\kappa)}\partial_z^2 S$. A test of self-consistency of this approximation is the comparison of the magnitude of these terms within the theory. Fig. 2.1 shows the terms $\frac{(2+\kappa)}{(3+2\kappa)}\partial_z^2 T$ (dark line) and $\frac{\kappa}{(3+2\kappa)}\partial_z^2 S$ (light line) computed through the PSW solution. As can be seen from the figure these terms only differ by a factor of order unity. Deep into the isotropic side, the term ignored by PSW exceeds the value of the term retained. Thus, while the PSW approach leads to a straightforward algebraic relation between T and S, a more accurate method would be to retain the partial derivative term as well, requiring that we solve a partial differential equation as opposed to an algebraic one.

Our approach to this problem uses the same approximations as PSW for Eq. 2.7. We thus take

$$S = \frac{S_c}{2}\left[1 + \tanh(\frac{z}{\sqrt{2}\xi})\right], \qquad (2.9)$$

where $\xi = \sqrt{\frac{1+\kappa/6}{1+2\kappa/3}}$. Inserting this in equation (2.8), scaling z by $\sqrt{2}\xi$, redefining the resulting quantity as z again, and dropping the nonlinear term, we obtain,

$$\partial_z^2 T = 2\beta[\tanh^2(z) + 8\tanh(z) + 9]T + \frac{\kappa}{2+\kappa}\tanh(z)[1 + \tanh(z)][1 - \tanh(z)].$$
$$(2.10)$$

with $\beta = \frac{6+\kappa}{3(2+\kappa)}$.

The solution of the equation consists of a homogeneous part T_h and a particular
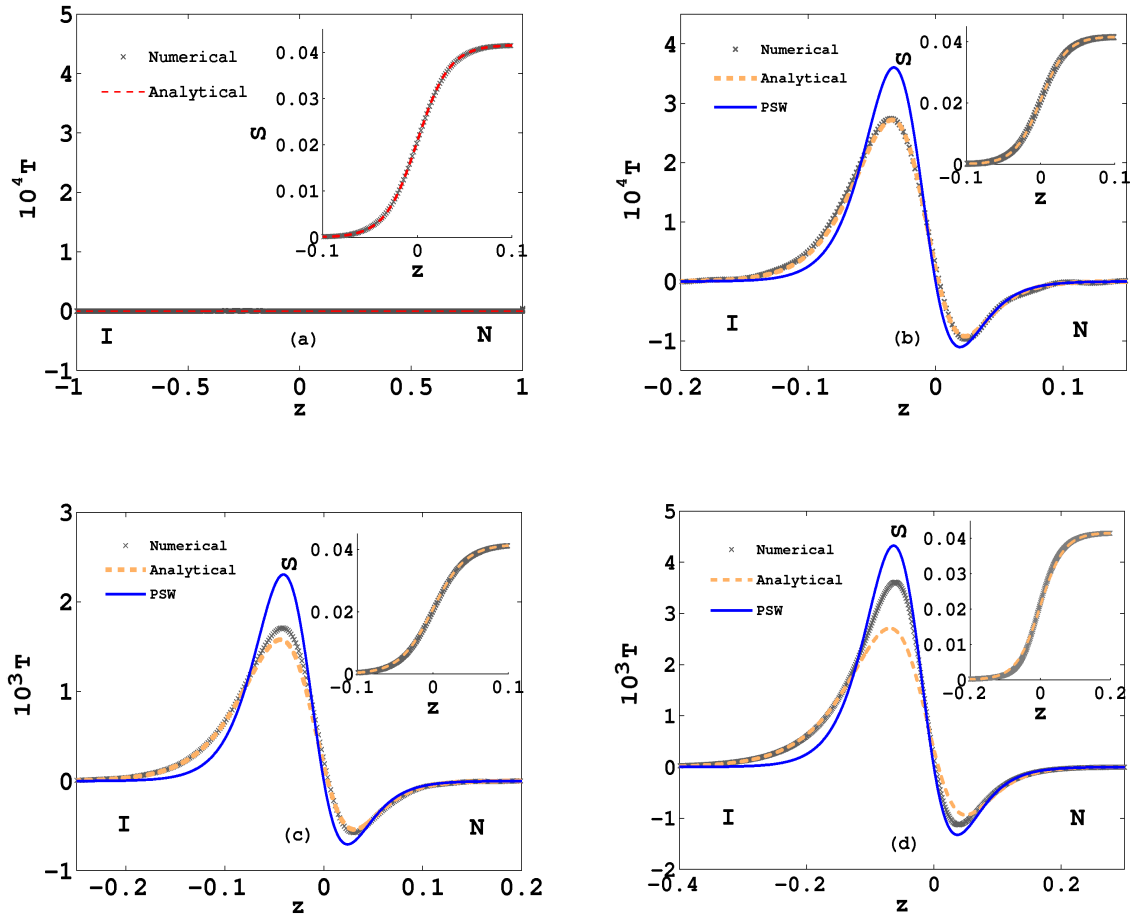
Figure 2.2: Biaxial and uniaxial profiles for $\kappa = 0(a), 0.4(b), 4(c)$ and $18.0(d)$, comparing results from our numerical computations ($\times$), with our analytic formula (dashed line) and the formula of PSW (solid line). The main figure shows the biaxial profile whereas the inset shows the uniaxial profile. In (a), for $\kappa = 0$, the solution has $T = 0$, with the S profile exactly given by the tanh form. In (b), for $\kappa = 0.4$, the computed biaxial profile (T) (main panel) is fit remarkably well by our analytic form, whereas the PSW approximation tends to overestimate the peak value. The uniaxial (S) profile is shown in the inset of (a); here the results obtained by us and by PSW are identical and the fit to a tanh profile is accurate over the entire region. In (c) (main panel), for $\kappa = 4.0$, the numerical data are fit well by the analytic forms, particularly away from the main peak, yielding essentially exact agreement deep into the isotropic and nematic sides. The PSW approximation is still an overestimate to the peak value, and also differs sharply in relation to the numerical data deep into the isotropic side. The inset shows the uniaxial (S) profile for this case. In (d) (main panel), for $\kappa = 18.0$, the PSW form appears to fit the peak better for larger κ, but again fails to capture the decay towards the isotropic side.
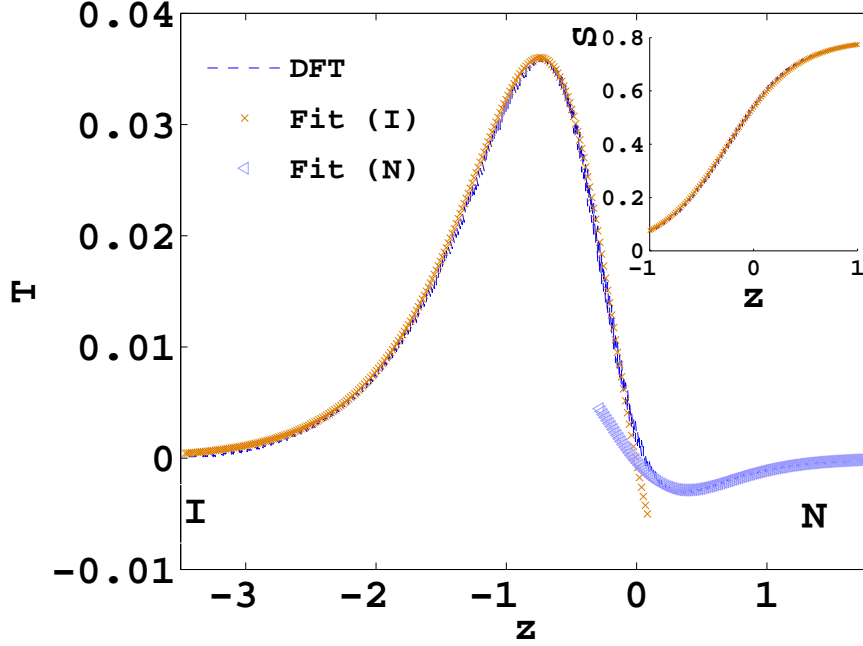
Figure 2.3: A comparison of the results of our analytic calculation to profiles of T obtained from a density functional calculation for the isotropic-nematic interface. Profiles obtained for two values of κ, $\kappa = 5.8$ (for $z < 0$) and $\kappa = 0.69$ (for $z > 0$) are shown. The larger κ value essentially fits the T profile exactly on the isotropic side, whereas the smaller κ value provides an accurate fit on the nematic side. The inset shows the S profile obtained from the density functional calculation, together with an optimum fit varying the value of l_c

part T_p where $T_h = C_1 y_1(z) + C_2 y_2(z)$ and

$$
\begin{aligned}
y_1(z) &= \left(\frac{1 - \tanh(z)}{2}\right)^{3\sqrt{\beta}} \left(\frac{1 + \tanh(z)}{2}\right)^{-\sqrt{\beta}} {}_2F_1[a_1, b_1, c_1, \frac{1 - \tanh(z)}{2}] \\
y_2(z) &= \left(\frac{1 - \tanh(z)}{2}\right)^{-3\sqrt{\beta}} \left(\frac{1 + \tanh(z)}{2}\right)^{\sqrt{\beta}} {}_2F_1[a_2, b_2, c_2, \frac{1 + \tanh(z)}{2}]
\end{aligned}
\tag{2.11}
$$

Here $a_1 = \frac{1}{2} + 2\sqrt{\beta} + \frac{\sqrt{1+8\beta}}{2}$; $\quad b_1 = \frac{1}{2} + 2\sqrt{\beta} - \frac{\sqrt{1+8\beta}}{2}$; $\quad c_1 = 1 + 6\sqrt{\beta}; a_2 = \frac{1}{2} - 2\sqrt{\beta} - \frac{\sqrt{1+8\beta}}{2}$; $\quad b_2 = \frac{1}{2} - 2\sqrt{\beta} + \frac{\sqrt{1+8\beta}}{2}$ and $c_2 = 1 + 2\sqrt{\beta}$. The function ${}_2F_1$ is a hypergeometric function and C_1 and C_2 are fixed by boundary conditions.

The particular solution takes the form

$$
T_p(z) = \left[-y_1(z)I_2(z) + y_2(z)I_1(z)\right]/W(z), \tag{2.12}
$$

22

where the Wronskian $W(z) = W = y_1(dy_2/dz) - y_2(dy_1/dz)$, where

$$
\begin{aligned}
I_1(z) = & \frac{2\kappa}{2+\kappa} \sum_{m=0}^{\infty} \frac{(a_1)_m(b_1)_m}{(c_1)_m m!} t^{1+m+3\sqrt{\beta}}(1-t)^{1-\sqrt{\beta}}\Big(- \frac{2}{2+m+2\sqrt{\beta}} \\
& + \frac{m+4\sqrt{\beta}}{(2+m+2\sqrt{\beta})(1+m+3\sqrt{\beta})} {}_2F_1[1, 2+m+2\sqrt{\beta}, 2+m+3\sqrt{\beta}, t]\Big)
\end{aligned}
$$
(2.13)

$$
\begin{aligned}
I_2(z) = & \frac{2\kappa}{2+\kappa} \sum_{n=0}^{\infty} \frac{(a_2)_n(b_2)_n}{(c_2)_n n!} t_1^{1+n+\sqrt{\beta}}(1-t_1)^{1-3\sqrt{\beta}}\Big(- \frac{2}{2+n-2\sqrt{\beta}} \\
& + \frac{n+4\sqrt{\beta}}{(2+n-2\sqrt{\beta})(1+n+\sqrt{\beta})} {}_2F_1[1, 2+n-2\sqrt{\beta}, 2+n+\sqrt{\beta}, t_1]\Big).
\end{aligned}
$$
(2.14)

The Pochhammer symbol $(a)_n$ which enters above is defined via $(a)_n = a(a + 1)(a+2)\ldots(a+n-1)$. Here $t = [1-\tanh(z)]/2$ and $t_1 = [1+\tanh(z)]/2$ and the result for $I_1(z)$ and $I_2(z)$ is obtained by expanding the hypergeometric functions in Eqns. 2.11 in a power series and integrating term-by-term[3]. Note that the solutions of the homogeneous part diverge asymptotically. Thus, for the boundary condition $T = 0$ at $z = \pm\infty$ the only physical solution is the particular one. Eq. 2.12 is thus the key analytical result of this chapter, describing the variation of biaxiality across the interface. In our numerical evaluations, we sum the series for $I_1(z)$ and $I_2(z)$, retaining as many terms as are required to ensure convergence. The series in I_2 converges very fast (only 3 terms need be retained for good results) whereas the series in I_1 converges more slowly and around 9 terms must be retained for convergence. To convert these into physical units, we must undo the sequence of length transformations, replacing $z \rightarrow z/(\sqrt{2}\xi l_c)$.

An asymptotic analysis of these equations is possible: for $z \rightarrow -\infty$, S and T are small. The tanh profile for S can be approximated as $\frac{1}{2}(1+\tanh(\frac{z}{\sqrt{2}\xi})) \rightarrow e^{\frac{2z}{\sqrt{2}\xi}}$ while Eq. (2.8) takes the form $2\xi^2\partial_z^2 T = 4\beta T - (\frac{2\kappa}{2+\kappa})e^{2\frac{z}{\sqrt{2}\xi}}$ with $\beta = \frac{6+\kappa}{3(2+\kappa)}$. Thus $\partial_z^2 T = \frac{4}{3}\frac{(3+2\kappa)}{(2+\kappa)}T - \frac{2\kappa(3+2\kappa)}{(2+\kappa)(6+\kappa)}e^{2\frac{z}{\sqrt{2}\xi}}$ with asymptotic solution

$$
T \sim e^{\sqrt{\frac{4(3+2\kappa)}{3(2+\kappa)}}z}, z \rightarrow -\infty,
$$
(2.15)

a result in perfect accord with the computed forms of T deep into the isotropic phase. Note that $T > S$ and $(S+T)/2 > S$ as one moves deeper into the isotropic side. This implies that the principal order parameter is negative as pointed out in Ref. [105], where this result was obtained numerically.

As $z \to \infty$, an alternative asymptotic expansion can be derived by taking $S = 1 - \frac{1}{2}e^{-bz}$ with $b = 2\sqrt{\frac{3+2\kappa}{6+\kappa}}$. We then obtain

$$T \sim e^{-2\sqrt{\frac{3+2\kappa}{6+\kappa}}z}, z \to \infty, \tag{2.16}$$

in agreement with our numerical results. Popa-Nita, Sluckin and Wheeler provide an analysis of the asymptotics in the specific limit that $\kappa \to \infty$. However, our results cannot be directly translated to this limit, since we assume a tanh profile of S; this approximation becomes increasingly inaccurate for larger κ (see below).

Our numerical results are obtained using a spectral collocation method [128], applied to our knowledge for the first time to the GLdG equations. In the spectral collocation, the solution is expanded in an orthogonal basis of Chebyshev polynomials in a bounded interval. Differentiation operators constructed from this Chebyshev interpolant are spectrally accurate, in the sense that the error vanishes exponentially in the number of retained polynomials. The interpolant is constructed so as to satisfy Dirichlet boundary conditions. Though the physical problem is for an unbounded interval, our numerical approximation of a bounded interval gives excellent results since all variation in the order parameters is restricted to the region proximate to the interface.

Specifically, we solve the equations of equilibrium

$$(A + CTrQ^2)Q_{\alpha\beta}(\mathbf{x}, t) + B\overline{Q_{\alpha\beta}^2(\mathbf{x}, t)} = L_1\nabla^2 Q_{\alpha\beta}(\mathbf{x}, t) + L_2\overline{\nabla_\alpha(\nabla_\gamma Q_{\beta\gamma}(\mathbf{x}, t))} \tag{2.17}$$

by transforming to a basis $\{a_i\}$ which enforces symmetry and tracelessness, as $Q_{\alpha\beta} = \sum_{i=1}^{5} a_i T_{\alpha\beta}^i$, where, $\mathbf{T}^1 = \sqrt{\frac{3}{2}}\,\overline{\hat{\mathbf{z}}\hat{\mathbf{z}}}$, $\mathbf{T}^2 = \sqrt{\frac{1}{2}}(\hat{\mathbf{x}}\,\hat{\mathbf{x}} - \hat{\mathbf{y}}\,\hat{\mathbf{y}})$, $\mathbf{T}^3 = \sqrt{2}\,\overline{\hat{\mathbf{x}}\,\hat{\mathbf{y}}}$, $\mathbf{T}^4 = \sqrt{2}\,\overline{\hat{\mathbf{x}}\,\hat{\mathbf{z}}}$, $\mathbf{T}^5 = \sqrt{2}\,\overline{\hat{\mathbf{y}}\,\hat{\mathbf{z}}}$. Overbars indicate traceless symmetric parts. We thus obtain five simultaneous partial differential equations for the a_i, which are steady-states of the time-dependent equations we have obtained earlier [17]. Note specifically that we make no symmetry-based ansatz for the components of $Q_{\alpha\beta}$. The

ambiguity of the sign of T in the uniaxial phase, or whenever the ordering of the sub-leading eigenvalues changes, is resolved by requiring solutions to be smooth over the computational domain.

The spectral collocation reduces these differential equations to non-linear algebraic equations. We solve them using a relaxation method from a well-chosen initial condition, relaxing till the differential change in successive iterations is less than 10^{-5}. Spectral convergence to machine accuracy is obtained by retaining 128 Chebyshev modes, as we have checked by an explicit calculation. To compare with analytical and density functional results, the solution at the Chebyshev nodes is interpolated using barycentric interpolation without compromising spectral accuracy. The DMSUITE library is used for the numerical implementation [132].

Our results are summarized in Fig. 2.2 and Fig. 2.3. The main panel of Fig. 2.2 (a), obtained by solving Eq. 2.7 and 2.8 for a value of $\kappa = 0.0$, shows the biaxiality profile obtained using our numerical spectral scheme (crosses), as compared to the analytic result of $T = 0$. The uniaxiality profile shown in the inset is exactly the tanh profile obtained by de Gennes. This limit provides a simple test of our numerical methods, since the solution to Eqs. 2.7 and 2.8 in this limit is exact. Fig. 2.2 (b) shows the biaxiality profile obtained using our spectral scheme (crosses), as compared to the analytic results derived here (dashed line) and results obtained by PSW (solid line) for a value of $\kappa = 0.4$. As can be seen, the numerical data are fit remarkably well by the analytic forms, whereas the PSW approximation tends to overestimate the peak value. The inset to Fig. 2.2 (b) shows the uniaxial (S) profile, obtained numerically as well as in our analytic calculation; here the results obtained by us and by PSW are identical. The fit to a tanh profile is accurate over the entire region.

The main panel of Fig. 2.2 (c) shows the biaxiality profile obtained using our spectral scheme (crosses), as compared to the analytic results derived here (dashed line) and results obtained by PSW (solid line) for a value of $\kappa = 4$. Again the numerical data are fit well by the analytic forms, particularly away from the main peak, yielding essentially exact agreement deep into the isotropic and nematic sides. The PSW approximation is still an overestimate to the peak value, and also differs sharply in relation to the numerical data deep into the isotropic side. The inset to Fig. 2.2 (c) shows the uniaxial (S) profile for this case. Fig. 2.2 (d) shows the biaxiality profile obtained using our spectral scheme (crosses), as compared to

the analytic results derived here (dashed line) and results obtained by PSW (solid line) for a value of $\kappa = 18$. For these - and larger - values of κ, our analytic fits differ noticeably from the numerical data. The PSW form appears to fit better for larger κ, although we believe that this is fortuitous. It appears that the principal error arises from our approximation of the S profile as a tanh form. For large κ, this approximation is less accurate.

Fig. 2.3 compares the results of our analytic calculation to profiles of T obtained from a density functional calculation for the isotropic-nematic interface [31] a method which provides an alternative, more molecular approach to this problem[134]. We have taken numerical data for uniaxial and biaxial profiles obtained in Ref. [31], varying the free parameters S_c, l_c and κ in our solutions till an optimal fit is obtained. The values of S_c and l_c can be obtained from fits to S; thus only κ need be varied to represent the T profile. Fig. 2.3 shows profiles obtained for two values of κ: $\kappa = 5.8$ (for $z < 0$) and $\kappa = 0.69$ (for $z > 0$). The larger κ value fits the profile very closely on the isotropic side, whereas the smaller κ value provides an accurate fit on the nematic side. An alternative density functional approach (Ref. [122]) yield profiles which can also be fit very well on the nematic side by our methods, although the fit towards the isotropic side is of reduced quality. It does not seem possible to fit the complete profile using a single value of κ. This could have been anticipated on physical grounds since the density functional theory yields a density difference between coexisting isotropic and nematic phases. The elastic coefficients L_1 and L_2 which enter our calculation do in principle contain a density dependence which we ignore here.

2.3   Conclusion and Results

In conclusion, we have presented results for the uniaxial and biaxial profiles, in the case of planar anchoring, for the classic problem of the structure of the isotropic-nematic interface within Ginzburg-Landau-de Gennes theory. Our work refines previous analytic treatments of biaxiality at the interface. We have implemented a highly accurate spectral collocation scheme for the solution of the Landau-Ginzburg-de Gennes equations and used this numerical scheme in our tests of the analytic results.

In comparison to earlier work, we obtain improved agreement with numerics for both the uniaxial and biaxial profiles, with our results being increasingly accurate as the anisotropy is reduced. We also provide accurate asymptotic results for the decay of the S and T order parameters deep into the nematic and isotropic phases. Our calculated profiles show a pleasing consistency with profiles obtained from density functional approaches. Further extensions of these numerical and analytic methods to the case of an intermediate anchoring condition far from the interface are currently under way.

3

The Isotropic-Nematic Interface with an Oblique Anchoring Condition

3.1 Introduction

In this chapter we study the isotropic-nematic interface within GLdG theory in the case where an oblique anchoring condition is imposed on the nematic state far from the location of the interface. For a flat interface, the components of $\mathbf{Q}$ can depend only on the coordinate perpendicular to the interface. We assume that this coordinate is aligned along the z axis, as shown in Fig. 3.1, which defines the geometry we work with in this chapter. We work at phase coexistence, imposing boundary conditions fixing the isotropic phase at $z = -\infty$ and the nematic phase at $z = \infty$. The components of $\mathbf{Q}$ as $z \to \infty$ are chosen so that S is fixed to its value at coexistence S_c, while the axis of the nematic is aligned along a specified (oblique) direction. The coexisting states must be separated by an interface in which order parameters rise from zero on the isotropic side of the interface to saturated, non-zero values on the nematic side. Since the two free energy minimum states are degenerate in the bulk, the position of the interface is arbitrary and can be fixed, for concreteness, at $z = 0$ in the infinite system. However, there are subtleties. Provided all components of $\mathbf{Q}$ vary substantially only in the neighbourhood of the interface, the interface can be located through several, largely equivalent criteria. However, if variations of $\mathbf{Q}$ are not confined to a region proximate to the interface but depend on the system size L irrespective of how large L is, the very isolation of an interface from the bulk is ill-defined. As indicated earlier, it is this situation
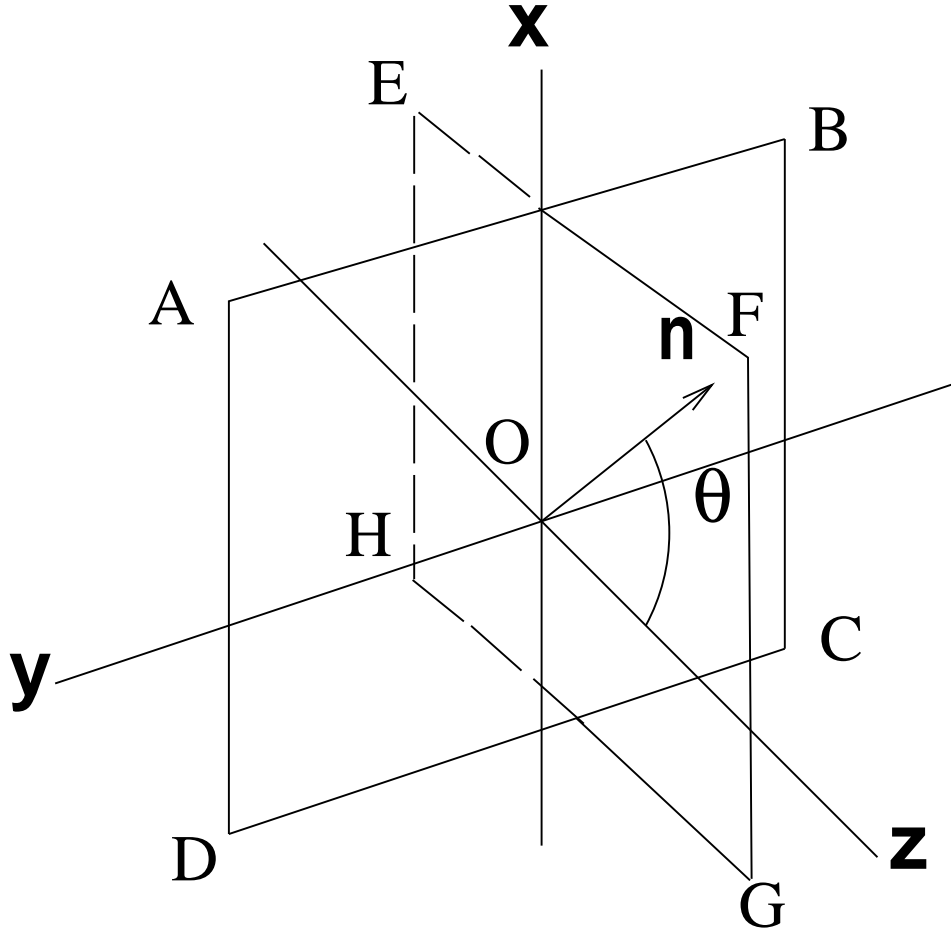
Figure 3.1: The interface geometry and the coordinate system used in this chapter. Note that the nematic director makes an angle θ with respect to the $z-$ axis direction. This angle is fixed at infinity to $\theta = \theta_e$. It can be chosen to vary between $\theta_e = 0$ (homoeotropic anchoring at infinity) and $\theta_e = 90°$ (planar anchoring at infinity). The isotropic phase is favoured, through boundary conditions, as $z \to -\infty$, whereas the nematic phase is favoured for $z \to \infty$. The plane of the interface is the $x - y$ plane, shown by ABCD in the figure, whereas the director is confined to the EFGH plane as shown. The origin is denoted by O.

which obtains in the case of oblique anchoring and the $L \to \infty$ limit must be taken with care.

The central results of this chapter are the following: A numerical minimization of the GLdG free energy which imposes a specific oblique anchoring condition on the system deep into the nematic while fixing the interface location at the origin shows that the elements of $\mathbf{Q}$ vary with space even far away from the interface, albeit slowly. Only in the limit of homoeotropic or planar anchoring is the variation of $\mathbf{Q}$ confined to a finite region. This variation in the case of oblique anchoring can, however, be split into hydrodynamic and non-hydrodynamic components. Generically, the variation of the non-hydrodynamic components, such as the magnitudes of S and T, are confined to a finite region, independent of the system size L, if L is large enough. However, the orientation of the nematic director varies in space: if the asymptotic value of the nematic order parameter at L represents uniaxial ordering along an oblique axis, the director orientation interpolates linearly between either a 90° value preferred at the location of the interface (planar anchoring) or a 0° value (homoeotropic anchoring), and the value imposed by the boundary condition at L. Whether planar or a homoeetropic anchoring is preferred at the interface depends on the sign of the second of the elastic coefficients in the GLdG expansion, the L_2 term, as initially shown by de Gennes[38].

Our results are consistent with the qualitative observations of PSW, but provide a detailed quantitative analysis in the case of oblique anchoring. We scale angle profiles computed for different values of the system size L onto a universal curve, indicating a linear profile. In the limit that $L \to \infty$, the slope with which the phase varies vanishes as $1/L$, so that the total energy cost for elastic distortions of the nematic field $\sim \int (\nabla \theta)^2 dz \sim L(\Delta \theta)^2/L^2 \sim 1/L$, thus vanishing in the thermodynamic limit. Thus, the isotropic-nematic interface with an oblique anchoring constraint imposed on the nematic side can be regarded as being marginally stable, as opposed to unstable, provided the thermodynamic limit is taken with care. We demonstrate that suitably chosen, flexible variational choices for the uniaxial and biaxial profiles can capture the variation of components of the $\mathbf{Q}$ tensor as a function of space. These variational profiles are obtained by generalizing results from a calculation of biaxial and uniaxial order parameter profiles in the planar case. These profiles are benchmarked against numerical calculations.

The outline of the chater is the following. In Section 1.4, we briefly reviewed

aspects of the Landau-Ginzburg-de Gennes transition which will be required in
our analysis. In Section 3.2 we obtain the equations representing the variational
minimum of the GLdG free energy, in a basis adapted to the symmetry of the
problem. Section 3.3 describes solutions to these equations, as appropriate to the
cases of planar and homoeotropic anchoring. The classic tanh profile obtained by
de Gennes is an exact representation of the interface in the limit of homoeotropic
anchoring as well as when the L_2 elastic constant vanishes, in which case the
interface is stable for any anchoring condition. In Section 3.4 we present our
numerical approach to the problem of interface structure, showing how numerically
exact profiles for the variation of S, T and θ can be obtained within the framework
of a minimization of the full GLdG free energy, subject only to the condition that
an interface is forced into the system.

In Section 3.5, we describe our variational approach to this problem, motivating
the choice of a three-parameter variational ansatz inspired by the approximate
solution due to Popa-Nita, Sluckin and Wheeler. We show that this variational
ansatz captures the features of the solution in both the extreme cases of planar
and homoeotropic anchoring, and is flexible enough to describe the intermediate
regime as well. In Section 3.6, we describe our methods of minimization for the
variational problem and our results for $L_2 > 0$ and $L_2 < 0$. We describe how our
numerical and variational calculations can be used to provide an accurate picture
of the interface with an oblique anchoring condition In Section 3.7 we present
asymptotic results for the variation of S, T and θ close to the bulk nematic state.
Section 3.8 contains our conclusions.

3.2   The Ginzburg-Landau-de Gennes Equations

The director $\mathbf{n}$, sub-director $\mathbf{l}$ and their joint normal $\mathbf{m}$ together define a frame.
We define z as the direction perpendicular to the interface. The fixed orientation
of the nematic axis at $z \to \infty$ can be used to define a plane, the xz plane. From
symmetry, and following the arguments of Sen and Sullivan, the nematic director
must always remain in this plane[119]. Thus, the spatial dependence of the frame
orientation can only come from the variation of a single tilt angle θ, which is
measured between the z axis and $\mathbf{n}$, as shown in Fig. 3.1.

Since we assume a flat interface, the components of $\mathbf{Q}$ are functions only of z. The tensor $\mathbf{Q}$ n the local frame defined by the principal axes, is diagonal and given by

$$\mathbf{Q} = \begin{pmatrix} -(S+T)/2 & 0 & 0 \\ 0 & -(S-T)/2 & 0 \\ 0 & 0 & S \end{pmatrix} \tag{3.1}$$

Transforming to the space-fixed frame (the laboratory frame), by rotation through the appropriate angle θ yields

$$\mathbf{Q}_\theta = \begin{pmatrix} -\frac{1}{2}(S+T)\cos^2\theta + S\sin^2\theta & 0 & -\frac{1}{4}(3S+T)\sin 2\theta \\ 0 & -(S-T)/2 & 0 \\ -\frac{1}{4}(3S+T)\sin 2\theta & 0 & -\frac{1}{2}(S+T)\sin^2\theta + S\cos^2\theta \end{pmatrix}. \tag{3.2}$$

Inserting this tensor form into the elastic free energy $\mathcal{F}_{el}[\mathbf{Q}]$ yields the elastic contribution to the free energy

$$
\begin{aligned}
F_{g\theta} &= \frac{(12 + 5\kappa + 3\kappa\cos(2\theta))(\partial_z S)^2 + 4\kappa\sin^2(\theta)\partial_z S \partial_z T + 2\left(2 + \kappa\sin^2(\theta)\right)(\partial_z T)^2}{8(3+2\kappa)} \\
&\quad - \frac{2\kappa\sin(2\theta)(3S+T)\left(\partial_z S - \partial_z T\right)\partial_z\theta}{8(3+2\kappa)} + \frac{(2+\kappa)(3S+T)^2(\partial_z\theta)^2}{4(3+2\kappa)}, \tag{3.3}
\end{aligned}
$$

Note that this contribution must vanish if S, T and θ are uniform.

The bulk free energy contribution $\mathcal{F}_h[\mathbf{Q}]$ is unchanged, as a consequence of the fact that the Landau term is constructed from rotationally invariant terms in the order parameter. It then takes the form

$$\mathcal{F}_h[\mathbf{Q}] = \frac{1}{3}(3S^2 + T^2) - 2(S^3 - ST^2) + \frac{1}{9}(9S^4 + 6S^2T^2 + T^4). \tag{3.4}$$

The Euler-Lagrange equation for the angle field, with $\theta' = d\theta/dz$, is

$$-\kappa\sin(2\theta)(3S+T)(S'' - T'') + (2(2+\kappa)(3S+T)^2\theta')' = 0, \tag{3.5}$$

where the primes indicate derivatives with respect to z.

First, note that for $\kappa = 0$ (*i.e.* no elastic anisotropy) the above equation has only the solution $\theta' = 0$, implying that θ is constant. A similar situation holds for the special θ values $\theta = 0, 90°$, for which again the only solution has $\theta' = 0$.

Thus, in these special limits, the angle θ remains fixed throughout the system. These results are, of course, consistent with the result that planar ($\theta = 90°$) and homoeotropic ($\theta = 0$) anchoring conditions yield a well-defined interface. Also, provided elastic anisotropy is absent, one can continue to define a stable interface for an arbitrary θ, since θ sticks to its asymptotic value throughout.

Finally, we note that once S and T are saturated, $S' = T' = S'' = T'' = 0$, and thus $\theta' = $ constant, yielding a linear variation of θ with z.

For completeness, the full set of Euler-Lagrange equations representing the minimization of the GLdG equations are, in addition to the θ equation above

$$
-\left(\frac{(\kappa\cos(2\theta) + 6 + 3\kappa)\,(3S + T)}{6 + 4\kappa}\right)\theta'^2 + \left(\frac{\kappa(4 + 3\kappa + \kappa\cos(2\theta))\sin(\theta)^2}{4\,(6 + 7\kappa + 2\kappa^2)}\right)T''
$$
$$
+\left(\frac{96 + 88\kappa + 19\kappa^2 + 12\kappa(2 + \kappa)\cos(2\theta) + \kappa^2\cos(4\theta)}{16\,(6 + 7\kappa + 2\kappa^2)}\right)S'' = 2S - 6S^2 + 4S^3 + 2T^2 + 4S\frac{T^2}{3}
$$

$$(3.6)$$

$$
\left(\frac{32 + 24\kappa + 3\kappa^2 - 4\kappa(2 + \kappa)\cos(2\theta) + \kappa^2\cos(4\theta)}{16\,(6 + 7\kappa + 2\kappa^2)}\right)T'' + \frac{\kappa(4 + 3\kappa + \kappa\cos(2\theta))\sin(\theta)^2 S''}{4\,(6 + 7\kappa + 2\kappa^2)}
$$
$$
+\frac{(\kappa\cos(2\theta) - 2 - \kappa)(3S + T)\theta'^2}{6 + 4\kappa} = \frac{2}{3}T + 4ST + \frac{4}{9}T^3 + \frac{4}{3}S^2T
$$

$$(3.7)$$

3.3 Interface structure for Planar and Homoeotropic Anchoring

This section briefly reviews the methodology for the solution of interfacial structure in the cases of homoeotropic and planar alignment[38]. While the exact solution in the case of homoetropic alignment, as originally proposed by de Gennes, motivates the canonical tanh form for the uniaxial order parameter, the more complex situation of planar anchoring requires the simultaneous solution of equations of motion for both S and T, in addition to the equation for θ[105]. We discuss how the Popa-Nita, Sluckin and Wheeler solution[105] of the planar case can be generalized, in a variational sense, to the more general problem of an oblique anchoring

condition.

3.3.1 Homeotropic Alignment

The equation of motion for homoeotropic boundary conditions is easily obtained
by setting $\theta = 0$, in the defining equations above. This immediately yields,

$$\frac{1}{2}\partial_z^2 S \;=\; S - 3S^2 + 2S^3 + T^2 + \frac{2ST^2}{3}, \tag{3.8}$$

$$\frac{1}{2(3+2\kappa)}\partial_z^2 T \;=\; \frac{1}{3}T + 2ST + \frac{2T^3}{9} + \frac{2S^2T}{3}. \tag{3.9}$$

It is easy to see that these equations have the solutions

$$S = \frac{1}{2}\left(1 + \tanh\left(\frac{z}{\sqrt{2}}\right)\right), \quad T = 0; \tag{3.10}$$

Here the treatment of de Gennes is exact.

3.3.2 Planar Alignment

The case of planar alignment follows from setting $\theta = 90°$ in the Euler-Lagrange
equations. This then yields the following set of coupled partial differential equa-
tions for the S and T order parameters,

$$\frac{(6+\kappa)}{(3+2\kappa)}\partial_z^2 S + \frac{\kappa}{(3+2\kappa)}\partial_z^2 T \;=\; 4S - 12S^2 + 8S^3 + 4T^2 + \frac{8ST^2}{3}, \tag{3.11}$$

$$\frac{\kappa}{(3+2\kappa)}\partial_z^2 S + \frac{(2+\kappa)}{(3+2\kappa)}\partial_z^2 T \;=\; \frac{4}{3}T + 8ST + \frac{8T^3}{9} + \frac{8S^2T}{3}. \tag{3.12}$$

In the zeroth order aproximation we drop terms in T as in the solution of the
first equation. This then yields $S = \frac{S_c}{2}(1+\tanh(\frac{z}{\sqrt{2}\xi}))$ where $\xi = \sqrt{\frac{1+k/6}{1+2k/3}}$. Putting
this in equation (3.12), scaling z again with $\sqrt{2}\xi$ and neglecting the nonlinear term,

we get the following equation.

$$
\begin{aligned}
\partial_z^2 T &= 2\beta(\tanh^2(z) + 8\tanh(z) + 9)T \\
&\quad + \frac{\kappa}{2 + \kappa}\tanh(z)(1 + \tanh(z))(1 - \tanh(z)),
\end{aligned}
\tag{3.13}
$$

with $\beta = \frac{6+\kappa}{3(2+\kappa)}$.

The PSW approximation now consists of dropping the $\partial_z^2 T$ term, yielding the algebraic equation

$$
2\beta(\tanh^2(z) + 8\tanh(z) + 9)T = -\frac{\kappa}{2+\kappa}\tanh(z)(1+\tanh(z))(1-\tanh(z)), \tag{3.14}
$$

which then immediately yields

$$
T = -\frac{\kappa}{2\beta(2+\kappa)}\frac{\tanh(z)(1 + \tanh(z))(1 - \tanh(z))}{(\tanh^2(z) + 8\tanh(z) + 9)}. \tag{3.15}
$$

We have recently suggested an improvement to these results, motivated by our tests of the self-consistency of the PSW approximations[66]. These tests indicate that the $\partial_z^2 T$ term dropped by PWS should be retained for a more accurate description of the interface. Our analytic results for this case, expressed as a sum over hypergeometric functions, agree well with numerical solutions of the GLdG equations and represent a significant improvement over the PSW solution, particularly in the case of small κ.

3.4 Numerical Minimization of the Ginzburg-Landau-de Gennes Free Energy for the Interface Problem

Our numerical results for the isotropic-nematic interface with an oblique anchoring condition are obtained from a direct minimization of the Ginzburg-Landau-de Gennes functional, with boundary conditions which ensure the presence of the interface as well as impose the required anchoring condition on the θ field. Our numerical methodology is the following: Defining a system size L, we discretize the one-dimensional (z) coordinate into N points, defining $\delta = L/N$. We use,
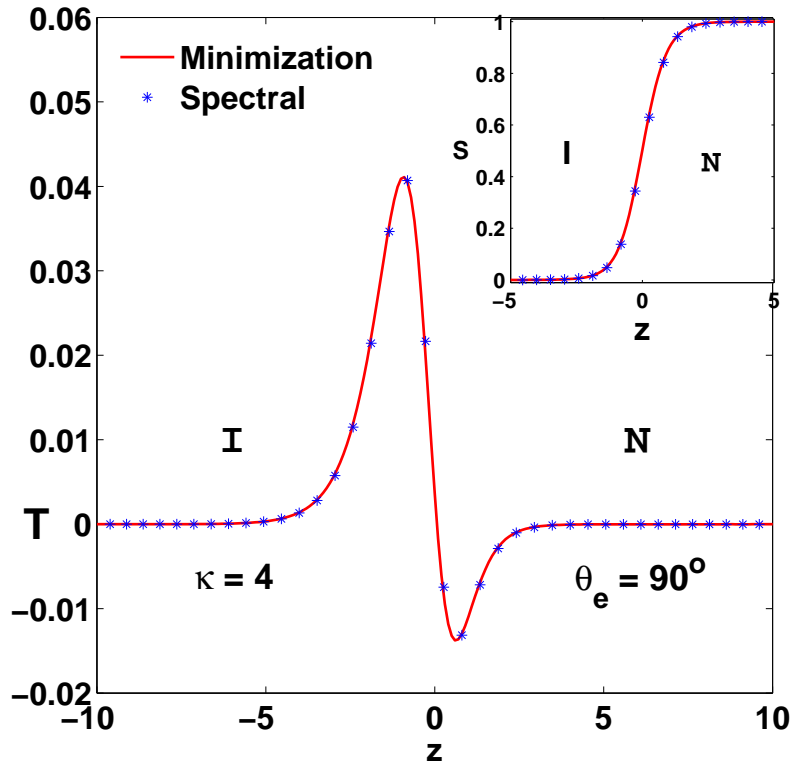
Figure 3.2: Profiles of the biaxial (T) (main figure) and uniaxial (S) order (inset) parameter as a function of the coordinate z across the interface, for planar anchoring and $\kappa = 4$ as obtained from a direct numerical minimization of the LGdG functional (solid line). The results obtained from an spectral collocation method are shown as points.

typically, $N = 1001$. The values of the fields S, T and θ at each of these points is varied so as to minimize the combined integrals of Eq. 3.3 and Eq. 3.4.

To do this, we perform a straightforward evaluation of the integral using the trapezoidal rule, replacing derivative terms in the integrand by the finite difference approximants. Thus, the gradient term $dS/dz \simeq [S(i+1) - S(i)]/\delta$. We have also used a variable discretization in some of our calculations, to assess the accuracy of our results, sampling with closely spaced points in the vicinity of the interface where the variation of S and T is largest. We impose boundary conditions on S, T and θ, by fixing the values at the two extreme boundaries to their values in the isotropic ($S = 0, T = 0$) limit, with θ arbitrary, and in the nematic limit

$(S = 1, T = 0, \theta = \theta_e)$.

The location of the interface is fixed at the centre, by imposing $S = 1/2$ at the central site. In principle, in a system of finite size L, our methods yield a constrained minimum for the following reason: The elastic energy on the nematic side is minimized by allowing the nematic region to expand as far as possible, effectively forcing the interface to invade the isotropic side. However, as discussed above, in the thermodynamic limit $L \to \infty$, this elastic energy cost reduces as $1/L$, vanishing in the thermodynamic limit where a stable interface is obtained. Alternatively, one can think of this in terms of adding a localized pinning potential with strength vanishing as $L \to \infty$, which serves only to stabilize the location of the interface.

This relatively simple approach yields results of very high quality, as we have checked by a direct comparison to exact results for the planar anchoring case as well as to numerical calculations using spectral methods in the case of planar anchoring. We have used the minimization routines (NMinimize) in Mathematica to find the stationary values of S,T and θ which minimize the free energy subject to the applied boundary conditions. This routine selects the most appropriate methodology from a variety of minimization techniques available, iterating till an accuracy between successive iterations of 1 part in 10^8 is obtained.

As a test of the quality of the minimization methodology which will be used in this chapter, we show in Fig. 3.2, profiles of the biaxial (T) (main figure) and uniaxial (S) order (inset) parameter as a function of the coordinate z across the interface, as computed by the numerical spectral methodology of Ref. [66] and the minimization technique described above, for the case of planar anchoring *i.e.* $\theta_e = 90°$, with $\kappa = 4$. Results obtained from the numerical minimization of the LGdG functional are shown as the solid line whereas results from the spectral collocation scheme of Ref. [66] are shown as points. These coincide to high accuracy.

3.5 Variational Method

Clearly, the solution of the full set of equations for S, T and θ given above is a formidable problem. Our approach to this problem therefore proceeds through the construction of simple, physically motivated variational choices for $\theta(z)$, $S(z)$

and $T(z)$. This choice is made keeping in mind that requirement that the results
should be consistent with computations in the simpler $\theta = 0, 90°$ limits, where the
angular variation is absent and the de Gennes solution and the PSW solution are
obtained, respectively.

Our approach begins by assuming a profile of the form

$$S = \frac{1}{2}(1 + \tanh(az)) \quad \text{and} \quad T = -b\tanh(cz)\frac{(1+\tanh(cz))(1-\tanh(cz))}{\tanh^2(cz) + 8\tanh(cz) + 9}.$$
(3.16)

together with the assumption that the theta variation can be fitted to a simply
parametrizable function. We have examined a variety of such functions for the
case of planar anchoring, including (a) $\theta = 90° - 2\frac{\psi}{L}z$ for $z > 0, 90°$ for $z < 0$,
(b) $\theta = 90° - \frac{\psi}{2}(1 + \tanh(a_1 z))$ which implies that at $z = \infty$, $\theta = 90° - \psi$ and at
$z = -\infty$, $\theta = 90°$, (c) $\theta = 90° - \frac{\psi}{2}(1 + \tanh(a_1 z))$ which implies that at $z = \infty$,
$\theta = 90° - \psi$ and at $z = -\infty$, $\theta = 90°$, (d) $\theta = \frac{\psi}{2}(1 + \tanh(a_1 z))$ (e) $\theta = \frac{\psi}{2L}z + \psi/2$
and (f) $\theta = p + \frac{\psi}{2}(1 + \tanh(a_1 z))$.

Our best results are obtained with the variational form

$$\theta = p + \psi\frac{z}{L}$$
(3.17)

subject to a constraint $p + \psi = \theta_L$ where θ_L is the value of angle at L, the system
size. It will be our intention to take the $L \to \infty$ limit later.

Note that the choice $p = 90°, \psi = 0, a = 1, b = \frac{\kappa}{2\beta(2+\kappa)}$ recovers the profile
of PSW for the planar case. The parameter values $\psi = 0, b = 0$ generate the de
Gennes solution. Thus, the two extreme limits of the variation of the anchoring
angle can be obtained with the appropriate choice of parameter values in the
variational form chosen above. These can be simply generalized to the case of
homoeotropic anchoring.

3.6   Numerical Methodology for the Variational Solution

These variational *ansätze* for S and T are inserted into the form for the free energy,
which is then minimized with respect to the parameters a, b, c, and p. This min-

imization is carried out using Mathematica. We use the "Nelder-Mead" method
for the minimization of a function of n variables. This is a direct search method
which uses an initial choice of $n + 1$ vectors which form the vertices of a polytope
in $n-$dimensions and a methodology for changing the vertices of this polytope
iteratively. The process is assumed to have converged if the difference between the
best function values in the new and old polytope, as well as the distance between
the new best point and the old best point, are less than preset values, typically of
the order of 10^{-10}.

To eliminate problems arising from an incorrect choice of initial values, we
have computed the minima for about 100 separate initial conditions and chosen the
parameter values corresponding to the least value of the free energy from these. Our
results for the minimization have been crosschecked using the differential evolution
method, a simple stochastic function minimizer.

3.6.1 Results from the Numerical and Variational Minimization: $\kappa > 0$

In Fig. 3.3, the main panel and inset of (a) and (b) shows profiles of the biaxial
(T) and uniaxial (S) order parameter as a function of the coordinate z across the
interface. We show the T profile in the main panel for systems of size $L = 50, 1290$
and parameter values (a) $\kappa = 8, \theta_e = 30$, and (b) $\kappa = 8, \theta_e = 60$. N and I in the
figure refer to nematic and isotropic respectively. The insets to (a) and (b) show
the corresponding profiles for S. We note that for larger anchoring angles, the T
profile converges faster as a function of system size than for smaller angles; contrast
the behavior for $\theta_e = 30^o$ and $\theta_e = 60^o$ in the figure. The profiles are qualitatively
similar to profiles obtained for the $\theta_e = 90^o$ degree, and asymptotically match
this profile as $L \to \infty$. These are computed by direct numerical minimization of
the LGdG functional, *via* the methodology described in the previous section. We
allowed θ on the isotropic side to vary, finding that the free energy minimum was
obtained when θ was stuck to the value it attained at the location of the interface.
This value is somewhat smaller than 90° for small system sizes but asymptotes to
this value as L goes to infinity.

In Fig. 3.3, in the insets to (c) and (d), we show the unscaled profile of
θ, the angle describing the orientation of the local director field as a function of
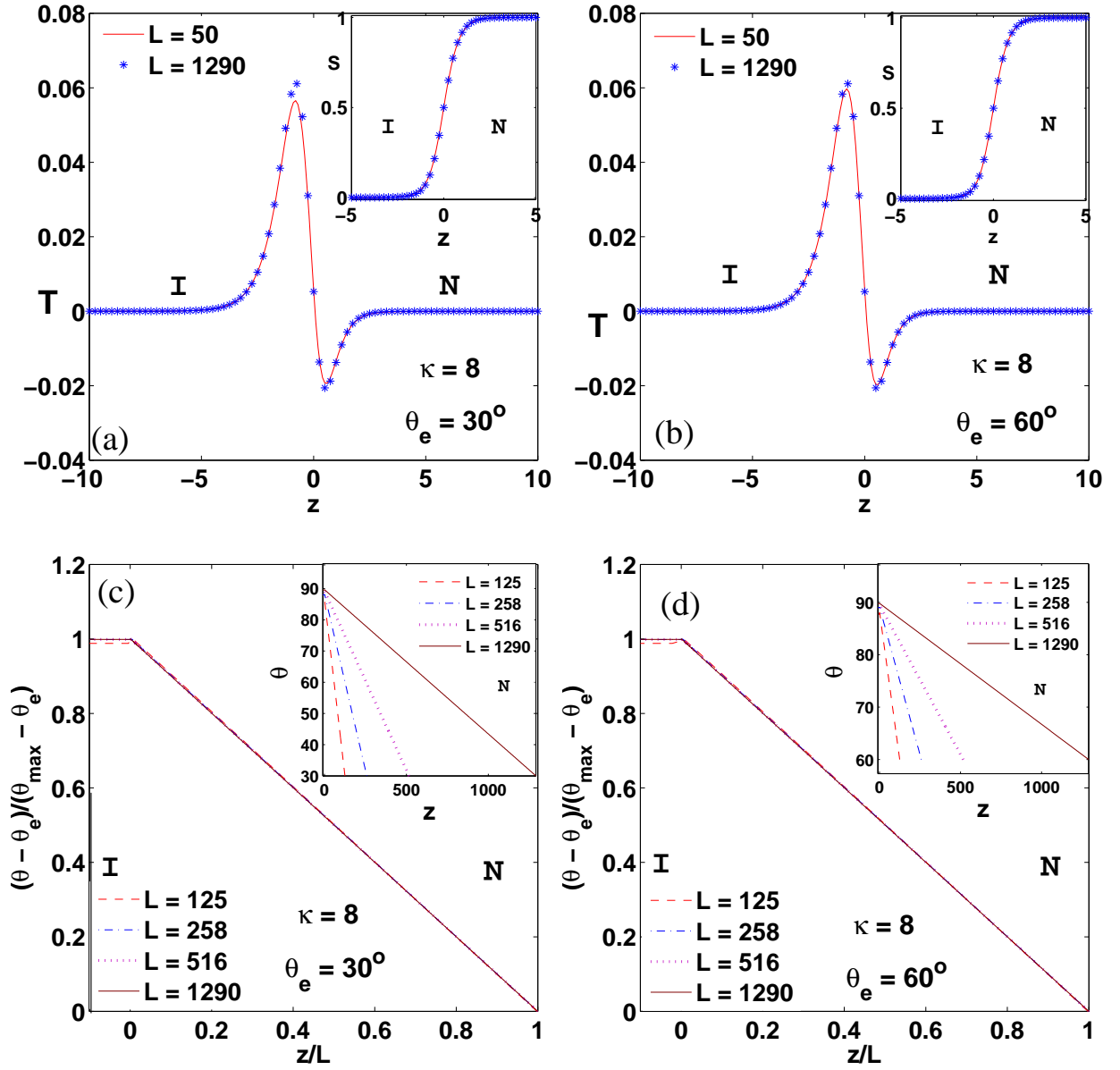
Figure 3.3: The main panel in (a) and (b) illustrates the profiles of the biaxial (T) order parameter as a function of the coordinate z across the interface, computed by direct numerical minimization of the LGdG functional for systems of size $L = 50$ and 1290, for the parameter values (a) $\kappa = 8, \theta_e = 30$, (b) $\kappa = 8, \theta_e = 60$. The insets to (a), (b) show the corresponding profiles for S. The main panel in (c) and (d) shows the scaled profiles for θ for the same parameter values as in (a) and (b). The insets to (c) and (d) show the corresponding unscaled profiles for θ. N and I refer to nematic and isotropic respectively.
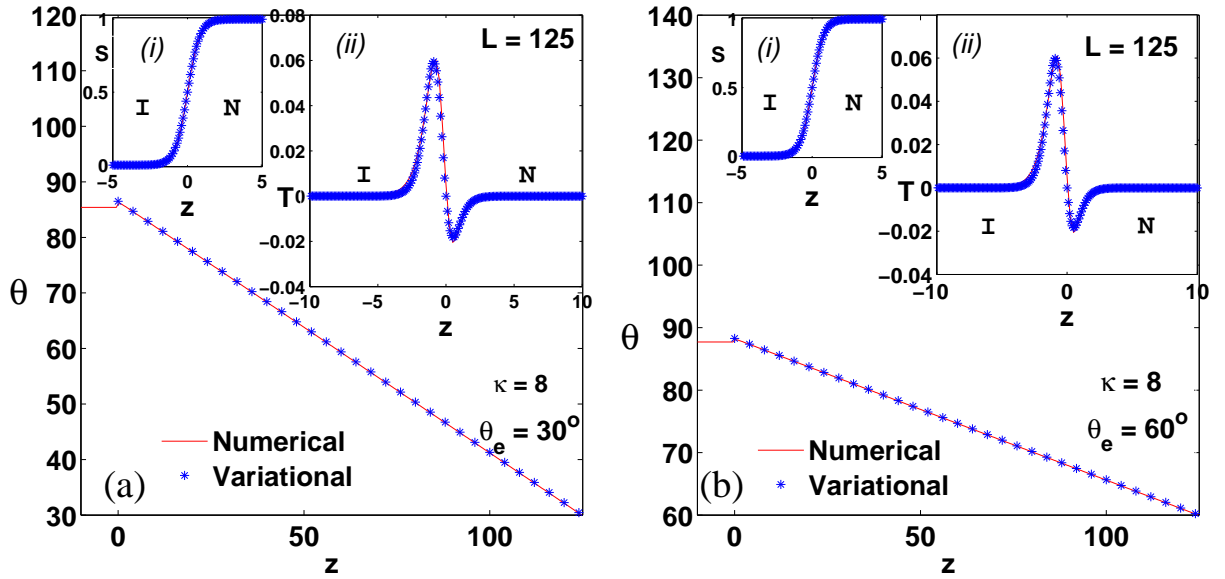
Figure 3.4: Main figure: Profiles of the angle θ describing the orientation of the local director field as a function of the coordinate z across the interface for a system of size $L = 125$, as obtained from a direct numerical minimization of the LGdG functional (solid line) and from the variational calculation described in the text (point). These are shown for parameter values (a) $\kappa = 8, \theta_e = 30$, and (b) $\kappa = 8, \theta_e = 60$. The inset labeled (i) in each sub-figure shows the corresponding profile of S, whereas the inset labeled (ii) shows the profile of T. N and I refer to nematic and isotropic, respectively.

z across the interface, as obtained from our numerical minimization. We show data for systems of size $L = 125, 258, 516$ and 1290, and for parameter values (a) $\kappa = 8, \theta_e = 30$, and (b) $\kappa = 8, \theta_e = 60$. The main panel, in both cases, plots the same data as a function of the scaled coordinate z/L on the $x-$axis and the quantity $(\theta - \theta_e)/(\theta_{max} - \theta_e)$ on the $y-$axis , thus normalizing the value to its maximum. This produces high quality collapse of the data, indicating that the angle profile is linear on the nematic side, interpolating linearly between its value at the interface to the anchored value of θ_e at $z = L$. Also, as the system size is increased, the value at the interface ($z = 0$), approaches 90°, indicating that anchoring at the interface is always planar in the asymptotic limit.

In Fig. 3.4 we show the comparison between the computed 3-parameter variational profile for the angle θ as a function of the coordinate z across the interface, for a system of size $L = 125$, as obtained from a direct numerical minimization of the LGdG functional (solid line) and the variational calculation described in the text (point). These are shown for parameter values (a) $\kappa = 8, \theta_e = 30$ and (b) $\kappa = 8, \theta_e = 60$. The inset labeled (i) in each sub-figure shows the corresponding profile of S, whereas the inset labeled (ii) shows the profile of T. Note that the variational result coincides with the result obtained from a direct numerical minimization to high accuracy. As the system size is increased, the value of θ at the interface approaches 90° within both the variational and the direct numerical minimization approaches, as indicated in Fig. 3.5.

Fig. 3.6 shows the variational parameters a (a), b (b) and c (c) as a function of system size L, together with the variation of the variational angle p (d), plotted for $\kappa = 1$. These parameters converge to their $L \to \infty$ values corresponding to the case of planar anchoring. In all cases the parameter p converges to the asymptotic value of 90° as the system size is increased, consistent with planar anchoring.

3.6.2 Results from the Numerical and Variational Minimization: $\kappa < 0$

Stability imposes the requirement that $3 + 2\kappa > 0$, but does not constrain the *sign* of κ (or, equivalently L_2), apart from this requirement. In this section we explore the consequences of a negative value for L_2.

We find that, consistent with de Gennes' prediction, a negative L_2 (or κ) con-
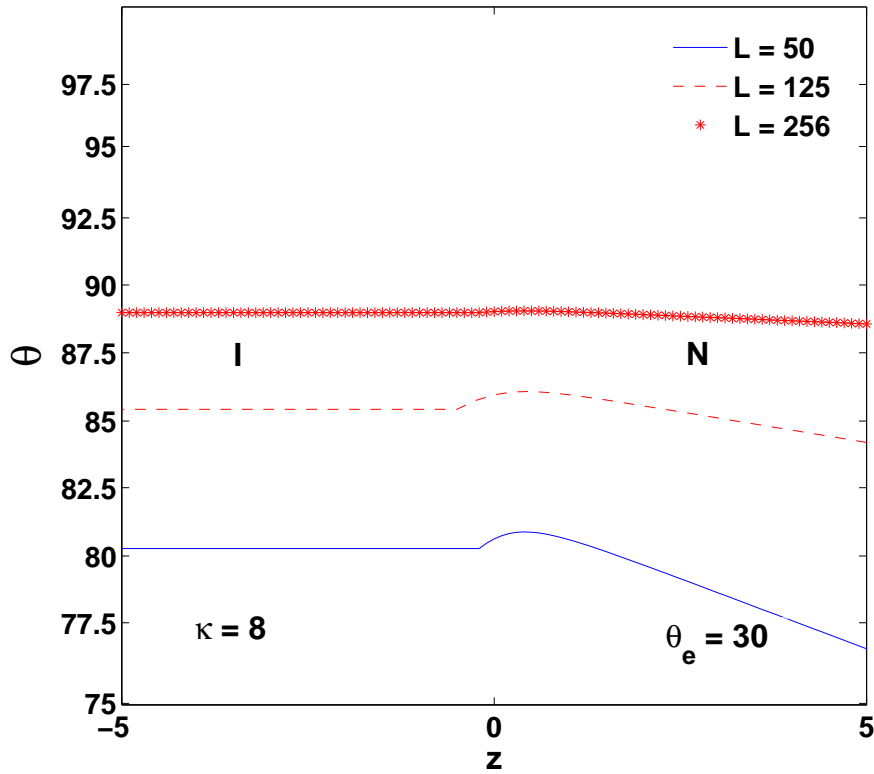
Figure 3.5: The angle profile $\theta(z)$, for different systems sizes $L = 50, 125$ and 256, illustrating the convergence to the value of $90°$ at the interface. The parameters are $\kappa = 8$ and the asymptotic anchoring angle is $\theta_e = 30°$. As the system size increases, note that the variation at the interface becomes smoother. The value of the anchoring angle at the interface is somewhat smaller than $90°$ for small system sizes but asymptotes to this value as L goes to infinity.
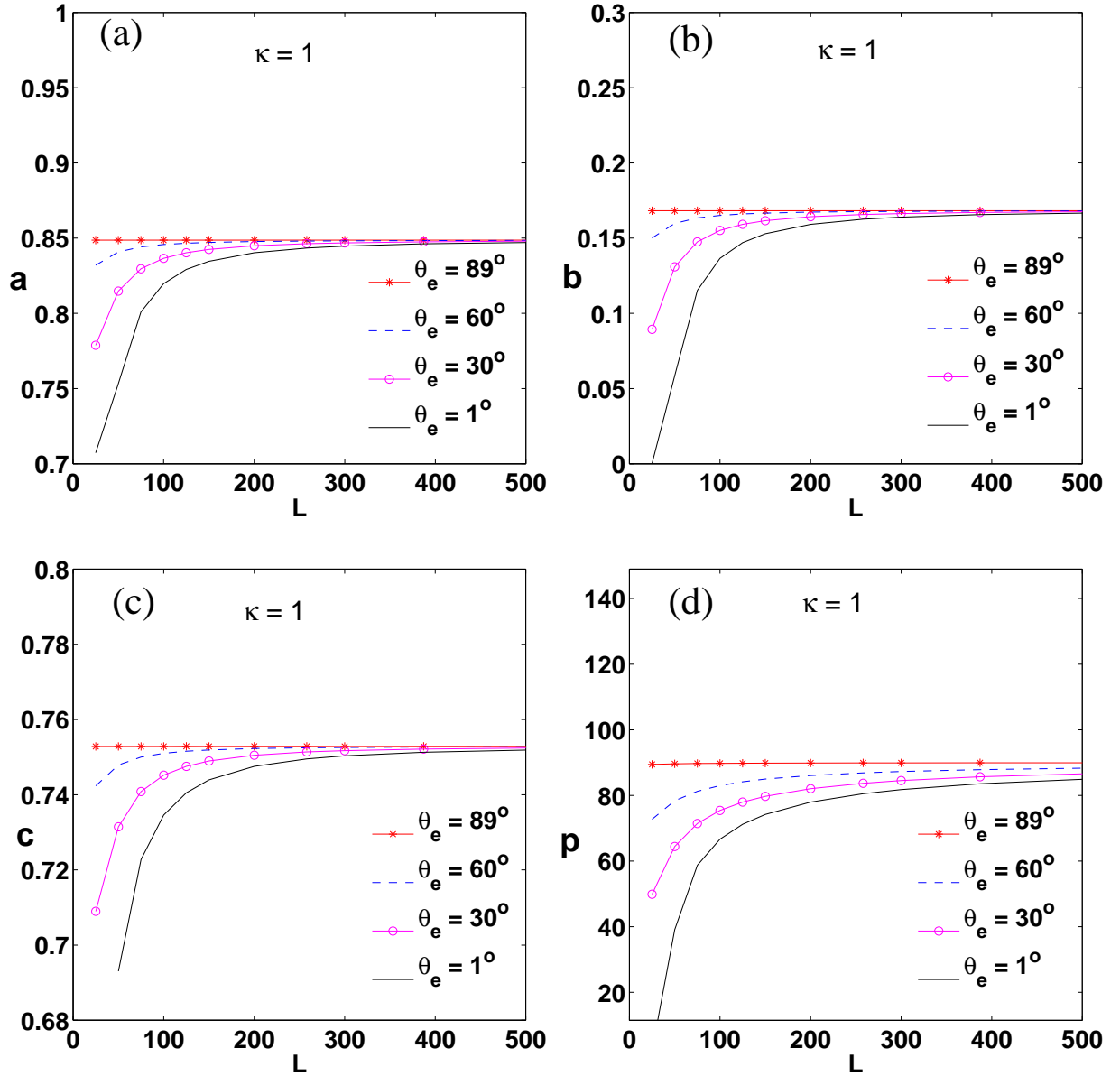
Figure 3.6: The variation of the variational parameters a (a), b (b) and c (c) with system size L, together with the variation of the variational angle p (d), plotted for $\kappa = 1$. Note that these parameters quickly converge to their $L \to \infty$ values corresponding to the case of planar anchoring. In all cases the parameter p appears to converge to the asymptotic value of $90°$ as the system size is increased.
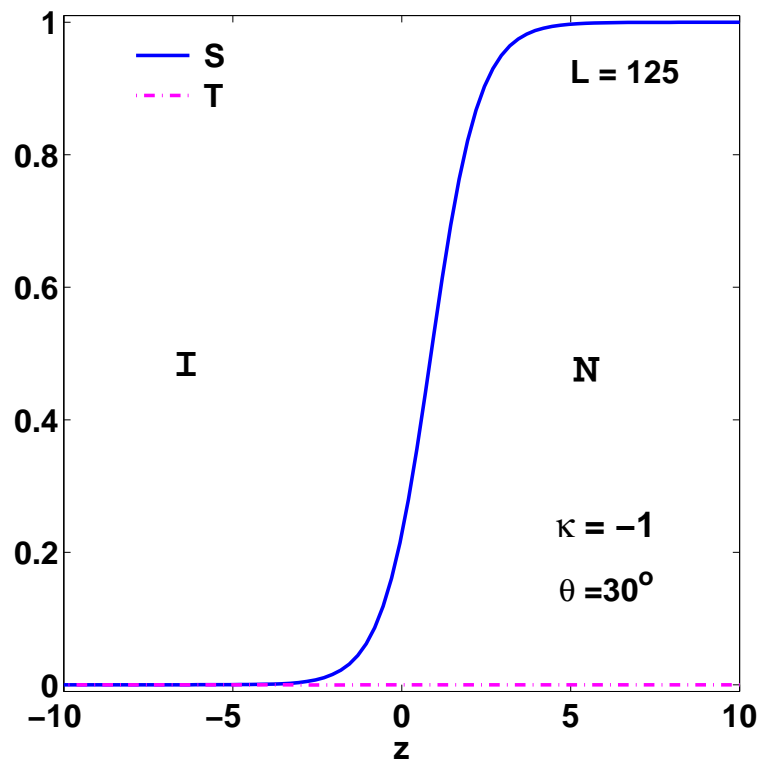
Figure 3.7: The variation of the S and T, for system size $L = 125$, plotted for $\kappa = -1$, with an oblique anchoring angle of 30°. Our results are consistent with $T = 0$ for homoeotropic anchoring.
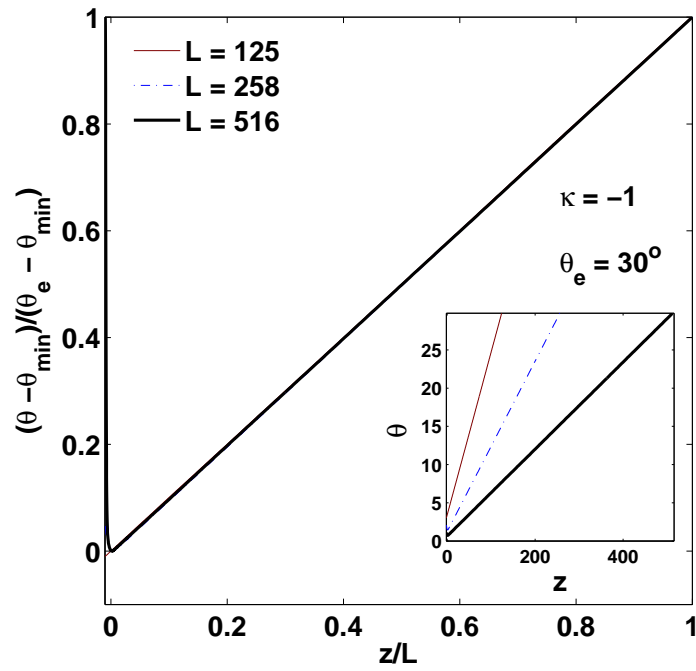
Figure 3.8: Plot of the angle scaled to its minimum value for each system size ($L = 125, 258$ and 516, against z/L for $\kappa = -1$ and an asymptotic, oblique anchoring angle of 30°. The inset shows the bare angles as a function of z for these different system sizes. Note that the excellent data collapse indicates that angle profiles in the case of $L_2 < 0$ scale in the same way as the $L_2 > 0$ case, with a homoeotropic anchoring being favoured at the interface.
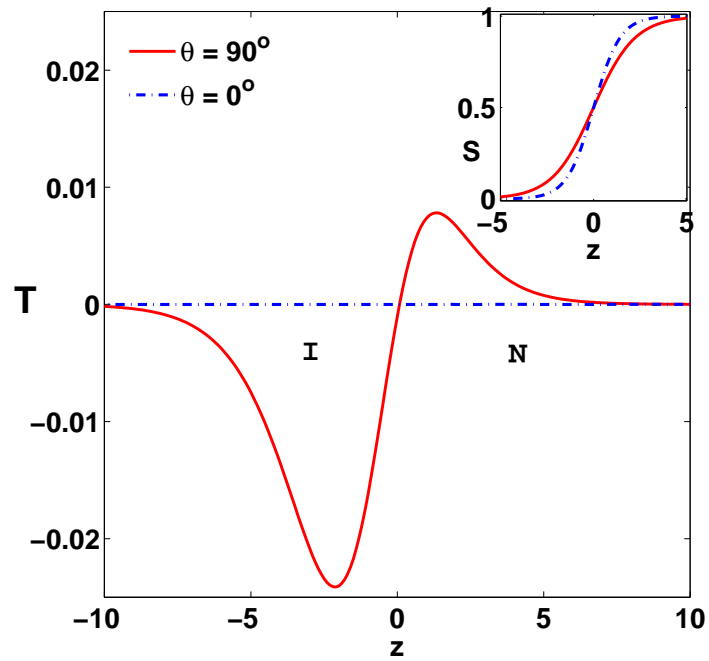
Figure 3.9: Main Panel: Profile of T, the biaxial order parameter, for $\kappa = -1$, in the two extreme cases of planar ($0°$) and homoeotropic ($90°$) anchoring. Note that the profile of T is *inverted* with respect to profiles obtained for $\kappa > 0$, with the minimum appearing on the isotropic side of the interface. Inset: The profile of S, consistent with a tanh form. Data are computed for $L = 50$. While the profile of T is non-zero for planar anchoring, biaxiality vanishes for the homoeotropic anchoring case.

sistent with stability favours *homoeotropic* anchoring at the interface, in contrast
to the case of positive L_2. Thus, the biaxiality T generically vanishes as $L \to \infty$,
whereas S assumes the canonical tanh form obtained by de Gennes. This can be
seen from Fig. 3.7 which shows the variation of S and T, for $L = 125$, plotted for
$\kappa = -1$. The anchoring at L is set to an oblique angle of 30°. The S and T profiles
are consistent with $T = 0$ for homoeotropic anchoring.

The preference for homoeotropic anchoring can be seen from Fig. 3.8 which
shows the director tilt angle scaled to its minimum value for each system size
($L = 125, 258$ and 516, against z/L for $\kappa = -1$, where an asymptotic, oblique
anchoring angle of 30° is imposed on the system at L. The inset shows the bare
angles as a function of z for these different system sizes. The excellent data collapse
indicates that angle profiles in the case of $L_2 < 0$ scale in the same way as the
$L_2 > 0$ case, except that homoeotropic anchoring is favoured in this case.

Finally, in Fig. 3.9, we show, in the main figure, the profile of T, the biaxial
order parameter, for $\kappa = -1$, in the two extreme cases of planar (0°) and ho-
moeotropic (90°) anchoring, with $L = 50$. Importantly, the profile of T is *inverted*
with respect to profiles obtained for $\kappa > 0$, with the minimum appearing on the
isotropic side of the interface rather than the nematic side, as earlier. The profile
of S is consistent with a tanh form. While the profile of T is non-zero for planar
anchoring, biaxiality vanishes for the homoeotropic anchoring case.

These results are consistent with the general trends observed in the case of
$\kappa > 0$, with the difference that homoeotropic, rather than planar, anchoring is
preferred once κ turns negative.

3.7   Asymptotic Solution

We can use our ansatz for S and T to check the self-consistency of our conjectured
behaviour for θ. Our chosen forms imply $S = 1 - e^{-2az}$ and $T = -be^{-2az}$ deep
into the nematic phase, as $z \to \infty$. Then $S' = 2ae^{-2az}$, $T' = 2abe^{-2az}$ and
$S'' = -4a^2 e^{-2az}$, $T'' = -4a^2 b e^{-2az}$. Inserting these into the equation for θ as
below,

$$4(2 + \kappa)\left(3S' + T'\right)\theta' - \kappa \sin(2\theta)(S'' - T''), +2(2 + \kappa)(3S + T)\theta'' = 0, \quad (3.18)$$

we get

$$8(2 + \kappa)\,(3 + b)\,a e^{-2az}\theta' + \kappa \sin(2\theta)(1 - b)a^2 e^{-2az} + 6(2 + \kappa)\theta'' = 0. \quad (3.19)$$

As $z \to \infty$, this equation reduces to $\theta'' = 0$. Thus, θ should have a linear profile in this asymptotic limit, taking the form

$$\theta = p + \psi\frac{z}{L}. \quad (3.20)$$

We can also compute corrections to this profile for $z \to \infty^-$. Let us now expand about the $z = \infty$ limit, in which case $\theta'' = 0$. Thus,

$$\frac{\theta'}{\sin(2\theta)} = \frac{-\kappa a(1 - b)}{2(2 + \kappa)(3 + b)}. \quad (3.21)$$

Integrating the left-hand side of this equation, we obtain

$$\frac{1}{2}\ln\tan(\theta) - \ln C = \frac{-\kappa a(1 - b)z}{2(2 + \kappa)(3 + b)}, \quad (3.22)$$

which has a solution $\theta = \tan^{-1}[Ce^{\frac{-\kappa a(1-b)z}{(2+\kappa)(3+b)}}]$. It can be seen that this will vanish as z goes to ∞ and is, in effect, negligible apart from a region close to the interface, at $z = 0$.

3.8   Summary and Conclusions

In this chapter, we have presented our results for the problem of the isotropic-nematic interface within Ginzburg-Landau-de Gennes theory, for the case in which an oblique anchoring condition is imposed on the system asymptotically on the nematic side, keeping the interface pinned at the origin. In this case, we find that nematic elasticity dictates that the nematic orientation interpolates smoothly between a value of 90° at the interface (planar anchoring) to the anchored value at the boundary on the nematic side when $\kappa > 0$. Thus, the preferred value of the anchoring angle at the interface is 90° in this case. The case $\kappa < 0$ with κ satisfying the stability requirement $\kappa > -1.5$ leads to stable homoeotropic anchoring at the interface, as predicted by de Gennes.

We have used simple variationally based descriptions of the structure of the interface, with our methods capturing essential features of interface structure, both qualitatively and quantitatively, for the case of oblique anchoring. Our methods access the non-trivial structure of biaxiality at the interface, including the large tail towards the isotropic side and the change in the sign of the biaxial order parameter across the interface. Our approach also captures the inversion of the profile of biaxiality as κ crosses zero.

The results presented here are broadly consistent with results from density functional approaches, molecular simulations and approaches based on the Onsager functional, but necessitate fewer approximations, truncations or assumptions about specific model systems. Thus, coarse-grained approaches based on the Ginzburg-Landau-de Gennes functional provide a powerful methodology for understanding generic features of the isotropic-nematic interface.

Part II

Lattice Models For Rheological Chaos in Sheared Nematics

4

Introduction to Rheology of Nematics

4.1 Introduction

Complex fluids are internally structured, possesing a macromolecular architecture which leads to a coupling between such structure and an imposed flow. The rheological properties of complex fluids have been studied extensively for this reason[60, 35, 106]. The goal of theoretical rheology is to relate deformation history to macroscopic properties of the material by developing constitutive equations that relate stress within the material to its deformation history. Constitutive equations together with mass and momentum conservation can be used to predict the flow of the material.

4.1.1 Stress

A central role in the study of rheology is played by a tensor field σ_{ij}, defined at all points within the medium and called the stress. The stress σ_{ij} (Fig. 4.1) is defined in terms of the component in the j-th direction of the force per unit area exerted on an infinitesimal surface element with normal in the i-th direction. Thus, the force per unit area in the j-th direction is given by

$$F_i = \sigma_{ij} n_j \tag{4.1}$$

where n_j is a unit vector normal to the surface Such forces cause deformations in elastic media and flow in fluid media.
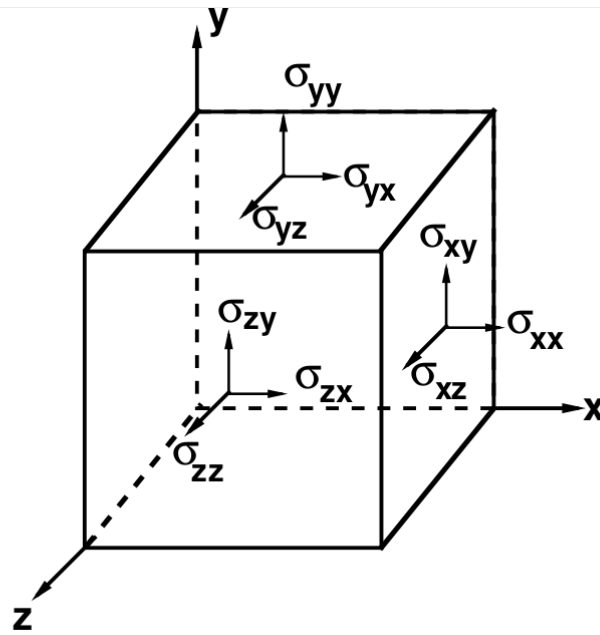
Figure 4.1: Components of the stress tensor, acting on a small cube of material

4.1.2 Strain

The deformation induced by $\boldsymbol{\sigma}$ is manifest in a strain (or strain history) of the medium. For an elastic medium, assuming a fixed reference state, the deviations from that state are parametrized in terms of a displacement vector at every point in space. Since a uniform translation of the material costs no energy, the only energy cost must be associated with a gradient in the deformation field. This deformation defines a tensor field, called the strain tensor. For solid media, the stress tensor is assumed to be a function of the deformation gradient tensor or strain tensor with (within linear elasticity), a fourth order tensor connecting stress and strain. This is just the continuum version of Hooke's law. For fluid media, no single reference state exists and fluid stresses arise from the relative motion of adjacent parts of the fluid.

Deformation gradient tensor

Consider a material in which a vector $\mathbf{r}'$ connects two points in the medium at time t'. This displacement vector is changed to $\mathbf{r}$ in the time interval between t' and a later time t, as shown in Fig. 4.2. This leads to stresses in the medium.

The vector $\mathbf{r}'$ is rotated and stretched as a result of the deformation. The inverse of the deformation tensor F, $i.e.$ F^{-1}, is defined through
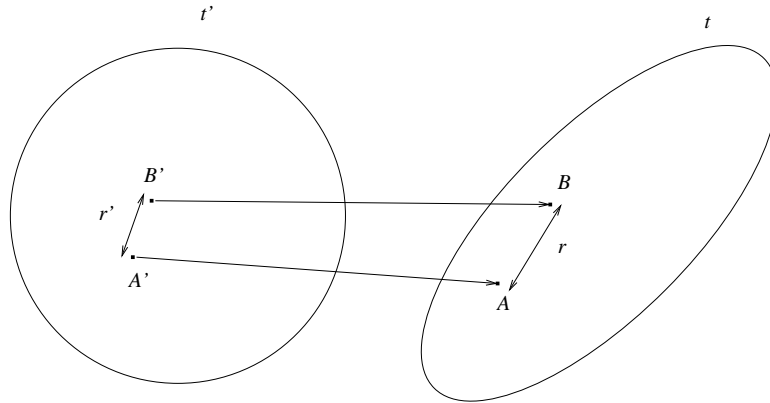
Figure 4.2: Transformation of the displacement vector upon a deformation

$$F_{ij}^{-1} = \frac{\partial r_j}{\partial r_i'} \tag{4.2}$$

which illustrates how components of the displacement tensor vary with the deformation. Fig. 4.3 shows how the components of $\mathbf{F}^{-1}$ are constructed for simple
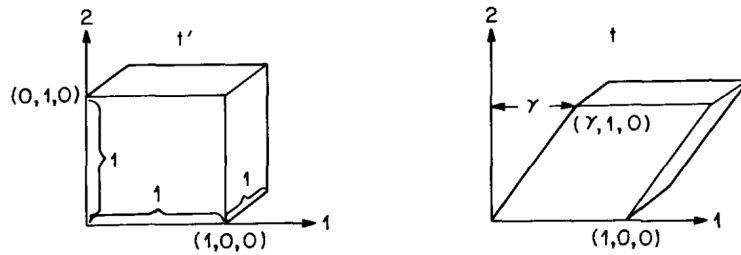
Figure 4.3: Shear deformations of a block of material

shear, in which elements retain their volume but change in shape. This is given by

the tensor components in matrix form,

$$\mathbf{F}^{-1} = \begin{bmatrix} 1 & 0 & 0 \\ \gamma & 1 & 0 \\ 0 & 0 & 1 \end{bmatrix} \qquad (4.3)$$

Fig. 4.4 shows the case of extensional deformation, for which the inverse of deformation tensor is given by

$$\mathbf{F}^{-1} = \begin{bmatrix} \lambda_1 & 0 & 0 \\ 0 & \lambda_2 & 0 \\ 0 & 0 & \lambda_3 \end{bmatrix} \qquad (4.4)$$

If the material is incompressible, so that the volume is unchanged by deformation, then $\lambda_1\lambda_2\lambda_3 = 1$. More generally, for any volume preserving deformation,

$$det \ \mathbf{F}^{-1} = 1 \qquad (4.5)$$
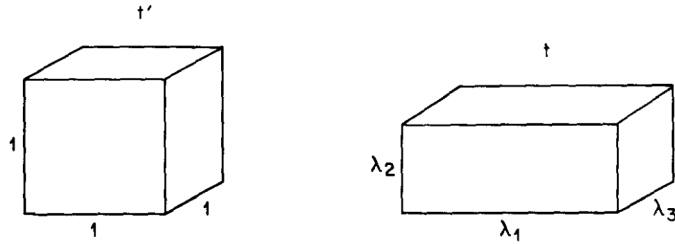
Figure 4.4: Extensional deformations, illustrating the definitions of λ_1, λ_2 and λ_3

In general, the tensor $\mathbf{F}^{-1}(t, t')$ carries the time indices t and t', since it describes the deformation that a material particle undergoes between the past time t', and the present time t. $\mathbf{F}^{-1}(t, t')$ is thus the cumulative deformation that occurs between time t' and t.

Velocity gradient tensor

If we take the time derivative of $\mathbf{F}^{-1}$, from Eq. 4.2

$$\frac{\partial}{\partial t}\mathbf{F}^{-1} = \frac{\partial \dot{\mathbf{r}}}{\partial \mathbf{r}'} = \frac{\partial \mathbf{r}}{\partial \mathbf{r}'} \cdot \frac{\partial \dot{\mathbf{r}}}{\partial \mathbf{r}} = \mathbf{F}^{-1} \cdot \nabla \mathbf{v}. \tag{4.6}$$

where $\nabla \mathbf{v}$ is the velocity gradient tensor. For simple shear as shown in Fig. 4.3 it is given by

$$\nabla \mathbf{v} = \begin{bmatrix} 0 & 0 & 0 \\ \dot{\gamma} & 0 & 0 \\ 0 & 0 & 0 \end{bmatrix} \tag{4.7}$$

and for extensional flow , as shown in Fig. 4.4 is given by

$$\nabla \mathbf{v} = \begin{bmatrix} \dot{\lambda}_1 & 0 & 0 \\ 0 & \dot{\lambda}_2 & 0 \\ 0 & 0 & \dot{\lambda}_3 \end{bmatrix} \tag{4.8}$$

For incompressible flow $\nabla \cdot \mathbf{v} = \mathbf{0}$.

Finger Tensor

It might have been thought that $\sigma_{ij} = \sigma_{ij}(\mathbf{F}^{-1})$ would uniquely specify the stress for deformed elastic media. However, constraints such as frame invariance indicate that the stress in elastic media must depend on the following combination, called the Finger tensor,

$$\mathbf{C}^{-1} \equiv \left(\mathbf{F}^{-1}\right)^T \cdot \mathbf{F}^{-1} \tag{4.9}$$

or its time derivative, in the case of fluid media. For viscoelastic media, which behave like elastic solids at short times and like fluids at long times, the stress must be a function of both the finger tensor and its time derivative, in such as way as to yield the right behavior in these two extreme limits.

For the case of simple shear $\mathbf{C}$ is given by

$$\mathbf{C}^{-1} = \begin{bmatrix} 1+\gamma^2 & \gamma & 0 \\ \gamma & 1 & 0 \\ 0 & 0 & 1 \end{bmatrix} \tag{4.10}$$

The rate of change of the Finger tensor is related to velocity gradient as follows

$$\dot{\mathbf{C}}^{-1} = (\nabla \mathbf{v})^T \cdot \mathbf{C}^{-1} + \mathbf{C}^{-1} \cdot \nabla \mathbf{v} \qquad (4.11)$$
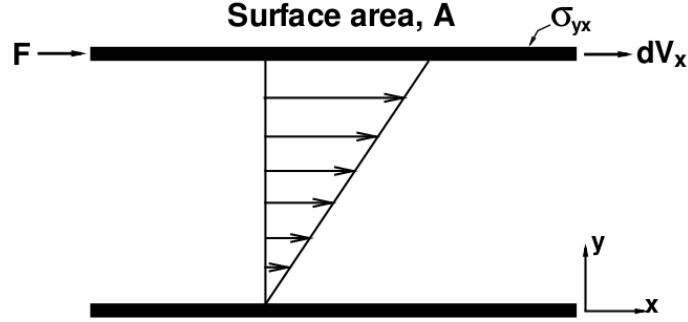
Figure 4.5: Depiction of flow and shear stresses in the Couette geometry, when a fluid is placed between two plates, with the upper plate being moves at a constant velocity

4.1.3   The Stress-Strain-rate relation and Viscosity

The relation between such velocity gradients and the internal stress tensor is fundamental to the theory of fluid mechanics and takes the form

$$\sigma_{ij} = f(\nabla_k v_l) \qquad (4.12)$$

In general the stress tensor and the velocity gradients are connected through a fourth order tensor *i.e.* $\sigma_{ij} = \lambda_{ijkl} \nabla_k v_l$. However, symmetries and physical arguments can be used to greatly reduce the number of independent components of λ_{ijkl}. For an incompressible fluid system, only one such component survives. It is called the shear viscosity.

A Newtonian liquid satisfies the constitutive equation

$$\sigma_{ij} = 2\eta \Gamma_{ij}, \qquad (4.13)$$

where Γ_{ij} is the symmetric part of the velocity gradient tensor

$$\Gamma_{ij} = (\partial_i v_j + \partial_j v_i)/2. \tag{4.14}$$

and η is the shear viscosity. The antisymmetric part of the velocity gradient tensor is called the vorticity. The vorticity is related to the angular velocity of the fluid.

The state-of-stress, or total stress, τ is the stress tensor plus a pressure contribution:

$$\tau_{ij} = \sigma_{ij} - p\delta_{ij} \tag{4.15}$$

Tensors that are proportional to $\boldsymbol{\delta}$ are called *isotropic*. For an incompressible material, only gradients of p affect fluid motion. Thus a constant isotropic tensor of arbitrary magnitude can be added to τ without affecting the physics. Thus, σ_{ij} is determined only up to an additive isotropic term. Hence the stress free state is equivalent to the state of isptropic stress. This is why only the stress difference, $\sigma_{11} - \sigma_{22}$, and not σ_{11} and σ_{22} separately, can be measured in simple shear.

The constitutive relation in a fluid connects stress and strain rate. In general such a relationship involves memory terms *i.e* the instantaneous stress is determined by the time history of the strain rate. For a Newtonian fluid, it is assumed that such a history dependence is absent. Thus, in general, while

$$\sigma_{ij}(t) = \int_{-\infty}^{t} dt' G(t-t')\dot{\gamma}(t') \tag{4.16}$$

for a Newtonian fluid, the kernel $G(t-t') = \eta\delta(t-t')$. In addition, for a Newtonian fluid, it is also required that the two normal stress differences $N_1 = \sigma_{xx} - \sigma_{yy}$ and $N_2 = \sigma_{yy} - \sigma_{zz}$ vanish for pure shear flow.

The physical picture for the shear viscosity η, is the following. Consider two plates separated by a distance d when placed parallel to each other (Couette geometry), and containing a fluid (Fig. 4.5). The upper plate is moved at a constant velocity, inducing a constant veocity gradient between the top plate and the bottom plate, if the velocity gradient is not large enough to significantly perturb the fluid. Then, there is a force per unit area on the upper plate acting to retard its motion. The shear viscosity defines the proportionality of this stress to the velocity gradient.
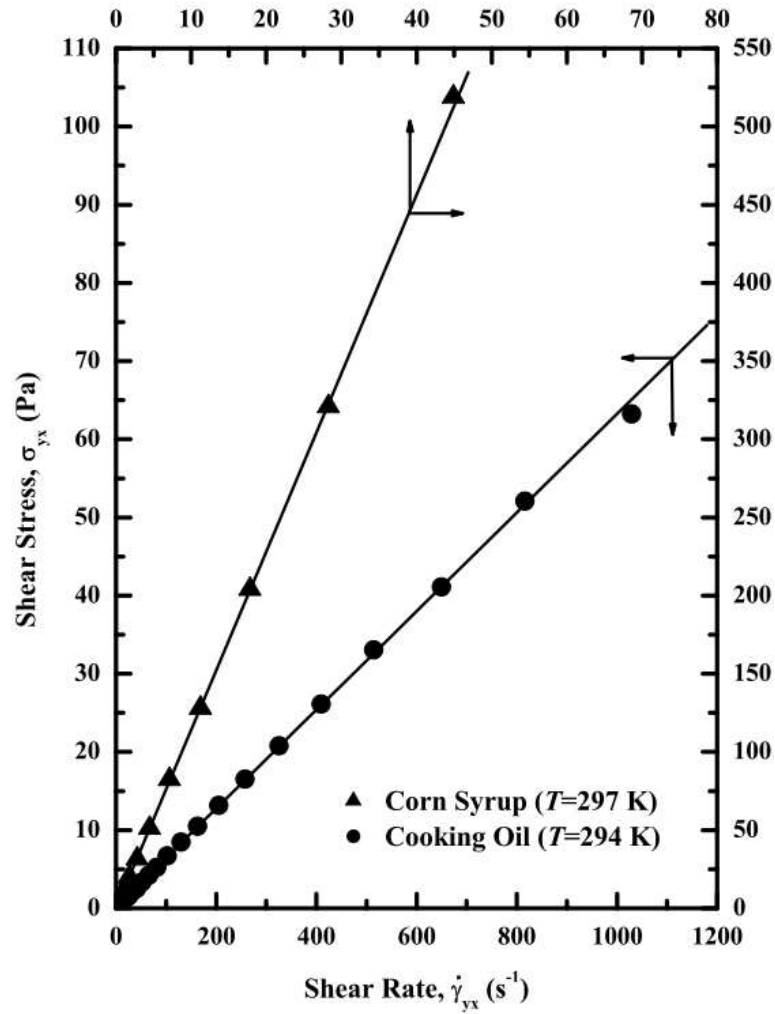
Figure 4.6: Shear stress *vs* Shear Rate for two fluids, with the linearity indicating regimes of constant viscocity. Figure from *Rheology of Complex Fluids* ,Abhijit P.; Krishnan, J. Murali; Kumar, P. B. Sunil (Eds.) Springer (2010).

4.2 Non-Newtonian Fluids

For a Newtonian fluid, the shear viscosity is a constant independent of the velocity gradient, equivalently the shear rate. Thus a plot of shear stress *vs.* shear rate yields a straight line, whose slope is the shear viscosity. The role of the bulk viscosity μ is usually ignored, since the approximation of an incompressible fluid is valid in most cases of interest to the soft matter physicist.

A non-Newtonian fluid exhibits a deviation from this linear relationship between stress and strain, with the viscosity decreasing at large shear rates (shear thinning) or increasing at large shear rates (shear thickening). Such non-Newtonian behaviour arises as a consequence of the coupling of internal microstructure to the flow and can be characterized in terms of two dimensionless quantities, the Weissenberg and Deborah numbers.

A rough categorisation of non-Newtonian fluid behaviour for convenience is as follows

1. The stress $\boldsymbol{\sigma}$ at a point only depends on the instantaneous value of the shear rate $\dot{\gamma}$ at that point. One can give various name to these material like purely viscous, inelastic, time-independent or generalized Newtonian fluids(GNF).

2. The Stress $\boldsymbol{\sigma}$ depends on the duration of shearing as well as on the magnitude of $\dot{\gamma}$. Such fluids are known as time-dependent fluids.

3. The stress $\boldsymbol{\sigma}$ shows both viscous and elastic behaviour. For instance, this class of materials shows partial elastic recovery, recoil, creep etc. They are called visco-elastic or elastico-viscous.

The classification scheme is arbitrary and most real materials display a combination of two or even all these different features under appropriate circumstances. Figure 4.7 shows the flow relation for some common non-Newtonian fluids.

For fluids with a characteristic time scale λ, placed in a flow with a characteristic shear rate $\dot{\gamma}$ and a characteristic frequency ω, or characteristic time T, two dimensionless groups can be formed

$$
\begin{aligned}
\text{Deborah number} \quad De &= \lambda\omega \text{ or } \lambda/T, \\
\text{Weissenberg number} \quad Wi &= \lambda\dot{\gamma}
\end{aligned}
\tag{4.17}
$$

The Deborah number, the ratio between the fluid relaxation time and the flow characteristic time, represents the transient nature of the flow relative to the fluid time scale. If the observation time scale is large (small De number), the material responses like a fluid. If it is small (large De number), the response is solid-like. From this point of view, there is no fundamental difference between solids and
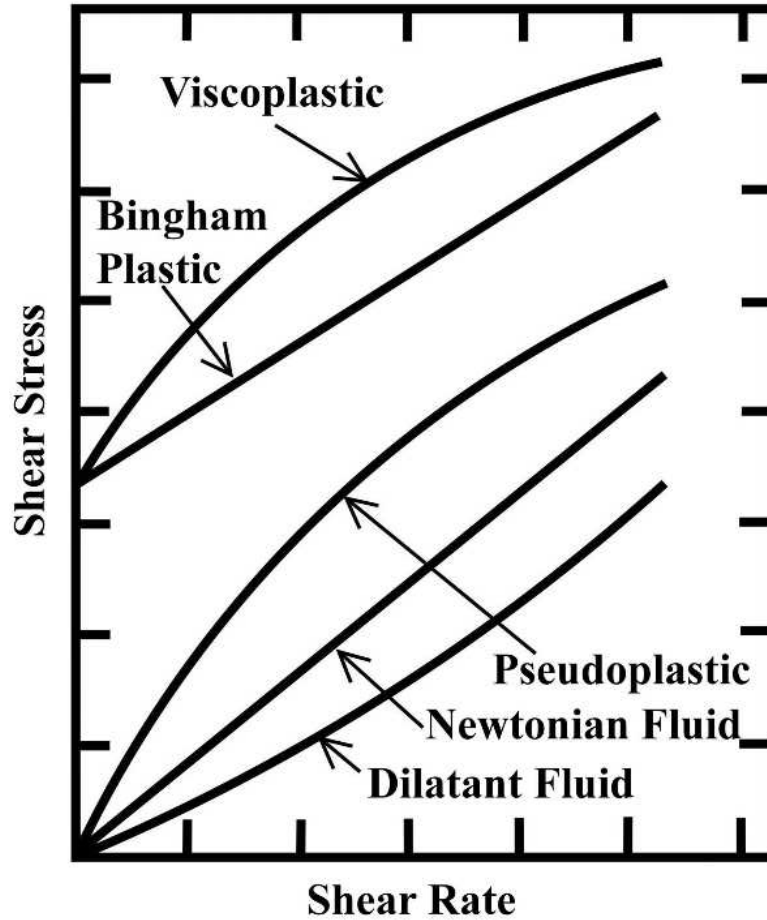
Figure 4.7: Schematic of the flow relation (stress vs shear rate) illustrating non-Newtonian behaviour Figure from *Rheology of Complex Fluids*, J. Murali Krishnan et al.

liquids; it is only a matter of time scale. In the limit, when $De = 0$ one has a Newtonian liquid, and when $De = \infty$, an elastic solid.

The Weissenberg number compares the elastic forces to the viscous effects. One can have a flow with small Wi number and very large De number, and vice versa. One can find significant non-Newtonian behaviour in a large Wi number flow. Therefore, the constitutive equation must contain non-Newtonian physics. A guide for the right choice of constitutive equations can be find with the help of Pipkin's diagram (Pipkin and Tauner [103]).
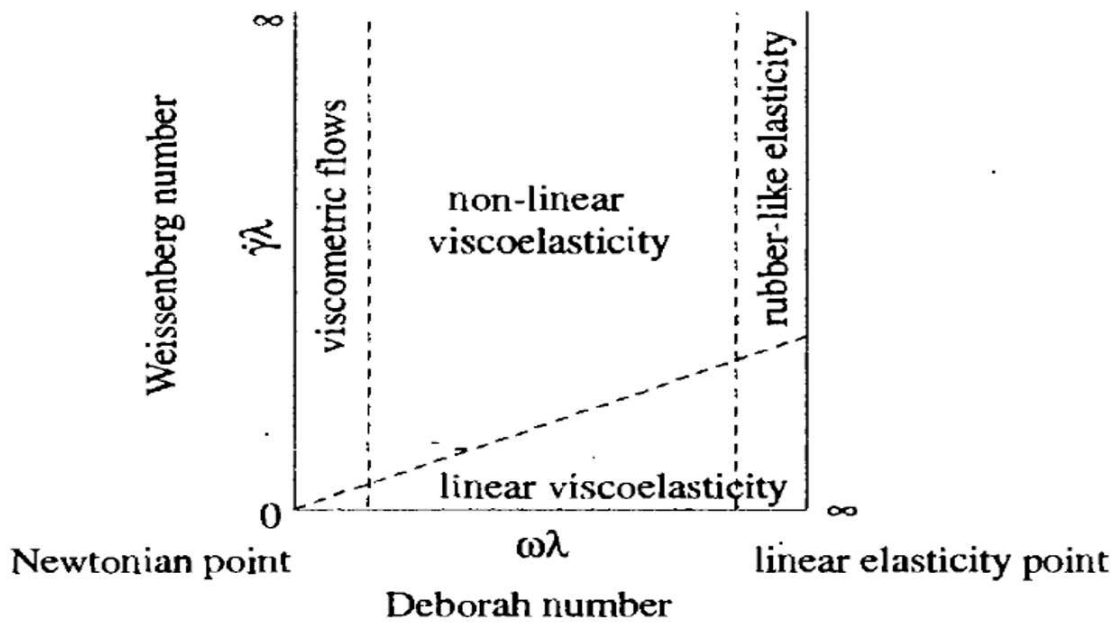
Figure 4.8: Pipkin's diagram, with the y axis showing the Weissenberg number and the x-axis showing the Deborah number. Regimes of non-linear and linear viscoelasticity as well as of regimes of viscometric flow and rubber elasticity are shown. Figure from Phan Thein N *Understanding Viscoelasticity*, Springer (2002)

4.3 Constitutive Modelling

In isothermal flow the conservation of energy is not relevant. Conservation of mass and conservation of momentum form four balance equations. The number of variables in question are ten: three velocity, one pressure and six independent stress components due to conservation of angular momentum. Thus one need six extra equations to form a well posed mathematical problem. A rheological equation of state provides the missing information by connecting the stress and the kinematics.

There are two different approaches for constitutive modelling, the *continuum* approach and the *microscopic* approach. In the continuum approach the relevant variables are identified, and are related in a frame work that ensures invariance under a change of frames. Different restrictions are then imposed to simplify the constitutive equation.

In the microstructure approach, one postulates a physical model of the microstructure representing the material. Solving the deformation at that level using well-tested physical principles (Newton's laws, conservation laws, etc.) allows the average stress and strain to be related, producing a constitutive equation.

In the continuum approach one is usually left with a general constitutive equations, which may have some undetermined functions or functionals. The details of these functions or functionals may be furnished by a relevant experiment. In the microstructure approach, the constitutive equations become more specific and therefore more relevant to the material in the question.

4.3.1 A Simple Equation for a Viscoelastic Material

For elastic materials, the simplest constitutive equation is given by

$$\sigma_{ij} = GC_{ij}^{-1} \tag{4.18}$$

as is easily verified using Eq. 4.10. The above equation can also be a constitutive equation for viscoelastic simple fluids in rapid deformations.

For slow deformations, the contribution to the stress of strain increments occuring in the remote past must be weighted less than than those occuring in the recent past. Fig. 4.9 illustrates the dependence of the cumulative deformation on

time. If one weights each strain increment by $\exp\left((t'-t)/\lambda\right)$, where t is the current time and t' is the past time, and λ the relaxation time, the increment in the stress is given by

$$d\sigma_{12} = Ge^{(t'-t)/\lambda}\dot{\gamma}(t')dt' \tag{4.19}$$

Hence the shear stress is given by integrating the expression

$$\sigma_{12} = G\int_{-\infty}^{t} e^{(t-t')/\lambda}\dot{\gamma}(t')dt' = G\int_{-\infty}^{t} \frac{1}{\lambda}e^{(t-t')/\lambda}\gamma(t',t)dt' \tag{4.20}$$

The last term of the Eq. 4.20 is due to integrating by part and $\gamma(t,t')$ is the shear strain that accumulated between times, t' and t.

$$\gamma(t,t') = \int_{t'}^{t} \dot{\gamma}(t'') \ dt'' \tag{4.21}$$

In tensorial form Eq. 4.20 is given by

$$\boldsymbol{\sigma} = G\int_{-\infty}^{t} \frac{1}{\lambda}e^{(t'-t)/\lambda}\mathbf{C}^{-1}(t,t') \ dt'. \tag{4.22}$$

Equation 4.22 is known as the *Lodge equation*. In a very fast deformation, the strain is imposed just before the present time, t. Then, $\mathbf{C}^{-1}$ is independent of t'. Therefore $\mathbf{C}^{-1}$ is a constant and Eq. 4.22 recovers the elastic limit.

$$\sigma_{ij} = GC_{ij}^{-1} \tag{4.23}$$

On the other hand, if the deformation is very slow then $\mathbf{C}^{-1}$ is a small perturbation from δ_{ij}. From Eq. 4.10, one can write

$$C_{ij}^{-1} = \delta_{ij} + 2(t-t')\Gamma_{ij}. \tag{4.24}$$

Then Eq. 4.22 gives,

$$\sigma_{ij} = G\delta_{ij} + 2G\lambda\Gamma_{ij} \tag{4.25}$$

Thus, apart from an isotropic term, the stress tensor is $2\eta\Gamma_{ij}$, where the viscosity $\eta = G\lambda$. This recovers the Newtonian limit.
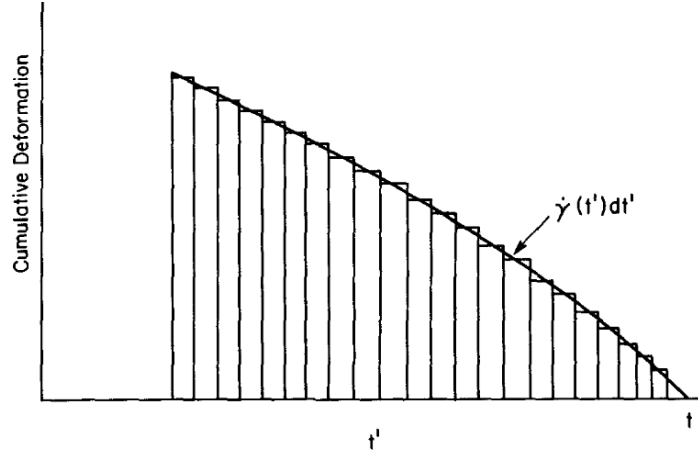
Figure 4.9: Dependence of the cumulative deformation on time

The differential version of the Lodge equation is given by

$$\dot{\boldsymbol{\sigma}} - \nabla \mathbf{v}^T \cdot \boldsymbol{\sigma} - \boldsymbol{\sigma} \cdot \nabla \mathbf{v} + \frac{1}{\lambda} \boldsymbol{\sigma} = \frac{G}{\lambda} \boldsymbol{\delta} \qquad (4.26)$$

which is called the *upper-convected Maxwell equation* (Eq. 4.26) The viscosity in simple shear predicted by the Lodge equation is given by

$$\eta = \frac{\sigma_{12}}{\dot{\gamma}} = \frac{G}{\dot{\gamma}} \int_{-\infty}^{t} \frac{1}{\lambda} e^{(t-t')/\lambda} \, \dot{\gamma}(t - t') \, dt' = G\lambda \qquad (4.27)$$

Thus there is no shear thinning and η is constant.

The first normal stress difference, $N_1 = \sigma_{11} - \sigma_{22}$ can be easily calculated. For simple shear $C_{11}^{-1} - C_{22}^{-1} = \gamma^2 = \dot{\gamma}^2(t - t')^2$. Inserting this in the Lodge equation gives,

$$N_1 = 2G\lambda^2\dot{\gamma}^2 \qquad (4.28)$$

Thus $\Psi_1 = N_1/\dot{\gamma}^2 = 2\eta\lambda$. From this one can calculate the relaxation time. $N_2 = \sigma_{22} - \sigma_{33}$ is zero since $C_{22}^{-1} - C_{33}^{-1} = 0$.

For the Newtonian fluid all normal stress differences are zero. The Lodge equation predicts, qualitatively, the non-Newtonian phenomena of rod-climbing, extrudate swell and the presence of spinning flows such as the tubeless siphon.

The Upper Convected Maxwell (UCM) equation can also be written as follows.

$$\dot{\boldsymbol{\sigma}} - \boldsymbol{\Omega}^T \cdot \boldsymbol{\sigma} - \boldsymbol{\sigma} \cdot \boldsymbol{\Omega} - \boldsymbol{\Gamma}^T \cdot \boldsymbol{\sigma} - \boldsymbol{\sigma} \cdot \boldsymbol{\Gamma} + \frac{1}{\lambda}\boldsymbol{\sigma} = \frac{G}{\lambda}\boldsymbol{\delta} \qquad (4.29)$$

where $\boldsymbol{\Omega}$ and $\boldsymbol{\Gamma}$ are the antisymmetric and symmetric part of $\nabla \mathbf{v}$ the velocity gradient tensor.

A related model equation for nonaffine motion is given by Johnson and Segalman, as is known as the *Johnson-Segalman model equation*. This is

$$\dot{\boldsymbol{\sigma}} - (\boldsymbol{\Omega}^T \cdot \boldsymbol{\sigma} + \boldsymbol{\sigma} \cdot \boldsymbol{\Omega}) - a(\boldsymbol{\Gamma}^T \cdot \boldsymbol{\sigma} + \boldsymbol{\sigma} \cdot \boldsymbol{\Gamma}) + \frac{1}{\lambda}\boldsymbol{\sigma} = \frac{G}{\lambda}\boldsymbol{\delta} \qquad (4.30)$$

where a is called the slippage parameter. This parameter is set to unity in the case of the upper convected Maxwell model.

4.3.2 Linear Rheology

The concept of linear viscoelasticity originated with Maxwell, who proposed

$$\frac{d\sigma}{dt} = G\frac{d\gamma}{dt} - \frac{\sigma}{\lambda}, \qquad (4.31)$$

where σ is the (one-dimensional) stress, γ is the (one-dimensional) strain, G is the modulus of elasticity and λ is a time constant. This is easily obtained from Eq. 4.26. Note that when the relaxation time is zero, keeping $\eta = \lambda G$ constant, the Newtonian model is recovered. When the relaxation time is infinitely large, a further integration yields the Hookean model.

Somer years later, Meyer introduced the equation

$$\sigma = G\gamma + \eta\frac{d\gamma}{dt}, \qquad (4.32)$$

Note that both the Maxwell and Meyer descriptions indicate that the stress depends only on the instantaneous strain rate and its time derivative. Boltzmann criticised the lack of generality in these models, proposing instead that the stress at the current time depends not only on the current strain but on the past strains as well.

It was assumed that a strain at a distant past contributes less to the stress than

a more recent strain. This is the familiar concept of fading memory. Furthermore, linear superposition was assumed. Supposing that strain between times t' and $t' + dt'$, say $d\gamma(t')$, contributes $G(t - t')d\gamma(t')$ to the stress, then the total stress at time t is

$$\sigma(t) = \int_{-\infty}^{t} G(t - t')d\gamma(t') = \int_{\infty}^{t} G(t - t')\dot{\gamma}(t')dt' \qquad (4.33)$$

Here, $G(t)$ is a decreasing function of time, the *relaxation modulus*, and $\dot{\gamma}$ is the shear rate.

The three-dimensional version of this relation is

$$\sigma_{ij}(t) = 2\int_{\infty}^{t} G(t - t')\Gamma_{ij}(t')dt' \qquad (4.34)$$

Linearity, combined with time-translational invariance of material properties, requires that

$$\sigma_{xy} = \sigma_{yx} = G(t - t')\gamma \qquad (4.35)$$

all other deviatoric components of σ_{ij} vanish, at linear order in γ, by symmetry.

Oscillatory flow

The case of an oscillatory flow is often studied. In this case $\gamma(t) = \gamma_0 e^{i\omega t}$ (taking the real part whenever appropriate). Substituting this in the above equation gives after trivial manipulation

$$\sigma_{xy} = \gamma_0 e^{i\omega t} G^*(\omega) \qquad (4.36)$$

where $G^*(\omega) = i\omega \int_0^{\infty} G(t)e^{i\omega t}dt$. The complex modulus $G^*(\omega) = G'(\omega) + iG''(\omega)$, where G' and G'' are the real and imaginary part of $G^*(\omega)$.

The linear Maxwell model.

The simplest imaginable $G(t)$ takes the form, $G(t) = G_0 exp(-t/\tau_M)$. When the complex modulus is written as $G = G' + iG''$ it can be seen that G consists of a component which is in phase with the strain and one which is out of phase. The in phase part, G', is known as the storage or elastic modulus and the out of phase part, G'', is the loss or dissipative modulus.

A perfectly elastic solid of modulus G_0 would have $G' = G_0$ and $G'' = 0$. In the case of a viscous liquid with viscosity η then $G' = 0$ and $G'' = \omega\eta$ since σ_{xy} is in

phase with the shear rate. For a viscoelastic material both G' and G'' are functions of the applied frequency,ω. In general, the loss modulus dominates at low frequencies, while the elastic modulus dominates at high frequencies. The material crosses over from viscous behaviour to elastic behaviour at some intermediate frequency where $G' = G''$.

For the Maxwell model, where $G(t) = G_0 exp(-t/\tau_M)$, characterised by a relaxation time, τ_M, the complex modulus is

$$G'(\omega) = G_0 \frac{\omega^2 \tau_M^2}{1 + \omega^2 \tau_M^2} \quad G''(\omega) = G_0 \frac{\omega \tau_M}{1 + \omega^2 \tau_M^2} \tag{4.37}$$

4.3.3   Nonlinear rheology

Nonlinear rheology addresses the response of a system to finite or large stresses. In this case the superposition principle assumed in linear response, does not hold. The range of independent measurements is thus much wider. Nonlinear versions exist of the step-strain and step-stress response measurements. For oscillatory measurements in which either stress or strain oscillate sinusoidally, the induced strain or stress will have a more complicated waveform in the non-linear regime.

$$\sigma_{xy} = G(t - t'; \gamma)\gamma \tag{4.38}$$

if $G(t - t'; \gamma) = G(t - t')h(\gamma)$, the system is called 'factorable'.

4.4   Wormlike Micelles

Amphiphilic molecules in water have a tendency to self-assemble by aggregating reversibly into larger objects. The simplest of these is a spherical aggregate called a 'micelle'. For geometrical reasons, a spherical micelle is self limiting in size, unless the solution contains oil that can fill any hole in the middle.

At the critical micelle concentration or CMC [64] micelles proliferate abruptly. By adding salt one can change the shape of the micelles. The most stable local packing of amphiphilic molecules leads to an evolution from spherical micelles towards a cylindrical shape; see Fig. 4.10. The transition from spherical to cylindrical shapes begins with micelles elongating into a short cylindrical body with

hemispherical end caps. The body then increases in size and eventually becomes very long.

The resulting giant micelles soon exceed the persistence length, of a few hundred microns, at which thermal motion overcomes local rigidity. Such giant micelles resemble a flexible polymer chain. After crossing the overlap threshold, these chainlike objects entangle but remain in an isotropic phase with no long-range orientational order. Such giant micelles are often referred to as "worm-like micelles" or "living polymers".

At very high concentrations, orientational ordering can arise, as can positional ordering, giving for example a hexagonal array of infinite straight cylinders[23]. A phase diagram is given in Fig. 4.11. A number of recent review articles are available on the rheology of worm like micelles. [8, 137, 44, 23, 136, 115, 89].
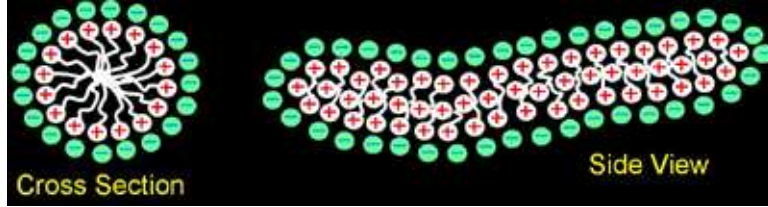
Figure 4.10: Cross-section and side-view of a worm-like micelle. Figure taken from http://ceb.cam.ac.uk

Within a mean field theory [118, 95] the free energy in terms of $c(N)$ the number density of aggregates containing N amphiphiles or monomers is given by

$$\beta F = \sum_N c(N)[\ln c(N) + \beta E] + F_0(\phi) \qquad (4.39)$$

where $\beta = 1/k_B T$; E is the energy of two end caps per chain and $c \ln c$ comes from mixing of micelles of different length. $F_0(\phi)$ contains excluded volume interactions and solvent terms represented via the volume fraction ϕ, with

$$\phi = \nu C = \nu_0 \sum_N N c(N), \qquad (4.40)$$

where ν_0 is the molecular volume of the amphiphiles and C their total concentration.
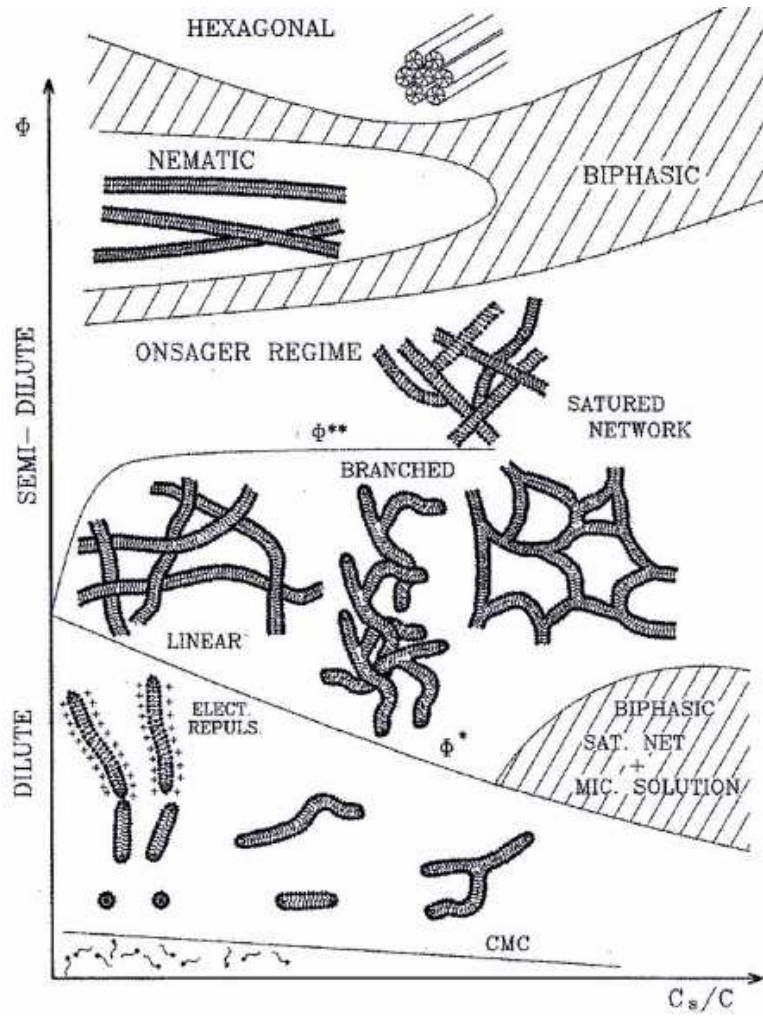
Figure 4.11: Schematic phase diagram for self assembly of ionic amphiphiles into giant micelles and related structures. The vertical axis represents volume fraction Φ of amphiphile; the horizontal is the ratio C_s/C of added salt. Figure taken from Ref. [23].

Minimizing this free energy at fixed ϕ gives the distribution

$$c(N) \propto \exp\left[-\frac{N}{\widehat{N}}\right]; \quad \widehat{N} \simeq \phi^{1/2} \exp\left[\frac{\beta E}{2}\right] \tag{4.41}$$

Experimental estimates of overlap volume fraction indicate that they are in the range of $0.005 - 5\%$ and $E \sim 10 - 20 k_B T$.
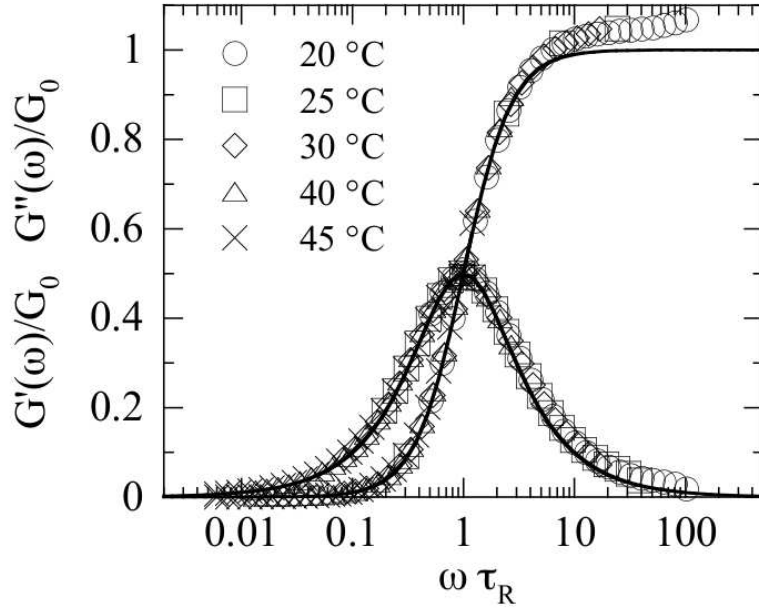
Figure 4.12: Elastic moduli G'/G_0 and $G"/G_0$ as function of the angular frequency for temperatures comprised between 20 and 45 degree Centigrade. G_0 is the elastic modulus and the angular frequency ω is normalized by the relaxation time of the fluid. Data are for the CPCl-NaSal wormlike micelles in water (0.5 M NaCl) at c = 12 wt and are reproduced from Ref. [15]. The solid lines correspond to Maxwellian viscoelastic behavior.

The observation which attracted rheological interest in wormlike micelle solutions was that their linear viscoelastic response can often be quite accurately modeled by a Maxwell model with just one or two relaxation times[16, 111, 110]. Over two decades, Cates and others have developed constitutive models which provide excellent agreement with the measured linear viscoelastic response of wormlike micelles [19, 54, 22].

In the model of Cates, it is assumed that there are two distinct relaxation mechanisms for wormlike micelles. These are: (i) a break up of the wormlike micelle with the chain breaking at any point along the length with equal probability and, (ii) the reptation of the micelle through the confinement tube. These two mechanism have characteristic time scales τ_{br} and τ_{rep} for breaking and reptation. In the fast breaking limit, where the break-up time is much shorter than the reptation time, $i.e.$ $\tau_{br} \ll \tau_{rep}$, the Cates model [125] predicts Maxwellian behaviour of these

worm-like micelles with a Maxwell relaxation time $\tau_m = (\tau_{br}\tau_{rep})^{1/2}$. A comparison of the Maxwell model with experiment is given in the figure (4.12).

The Maxwell model fit is best for wormlike micelles in concentrated solution. For low concentration before overlapping regime, wormlike micelles show shear thickening behaviour and a Maxwell fit is poor, as indicated in reference [108].

Cates and Candau [22] developed a scaling for the relaxation time, elastic modulus(G_0) and zero shear rate viscosity (η_0) with volume fraction ϕ of surfactant. These predict

$$\tau_m = (\tau_{br}\tau_{rep})^{1/2} \sim \phi^{1.5}, \tag{4.42}$$

as well as

$$G_0 \sim \phi^2, \tag{4.43}$$

and

$$\eta_0 = G_0\tau_m \sim \phi^{3.5}, \tag{4.44}$$

The predicted scaling behaviour is in very good agreement with experimental results [13]. In wormlike micelles which exhibit some degree of branching or in the presence of strongly binding counterions, the scaling of viscosity and relaxation time break down but the modulus continues to follow the quadratic scaling with volume fraction [120, 121, 109, 114]

The effect of salt concentration on the rheology of wormlike micelles solutions can be quite complex. The viscosity and relaxation time are often non-monotonic functions of salt concentration [111, 120, 121, 34]. Granek and Cates [54] showed that the high frequency deviations can be explained by Rouse-like relaxation modes and primitive path fluctuations along the micelle chain.

The linear behaviour agrees well with the Maxwell model at higher concentrations of surfactant. The break up time τ_{br} roughly corresponds to the angular frequency at which the data deviates from the prediction of the single mode Maxwell model[77] and has been found to lie between several tens of milliseconds to several hundred milliseconds [76]. Kern *et al.* [77] show that the number of entanglements per wormlike micelle can be approximated by the inverse of the high frequency minimum in the normalised storage modulus.

4.4.1 A Constitutive equation for giant micelles

Cates has developed a constitutive equation for giant micelles in reference [20], which we reproduce here for completeness. This model is the extension of the reptation model of Doi and Edwards for polymers, with the dynamics of breaking and fusion of giant micelles incorporated and is called a reptation-reaction model.

The constitutive equation for this model is the following

$$
\begin{aligned}
\sigma_{ij} &= \frac{15}{4} G_0 \left[W_{ij} - \frac{\delta_{ij}}{3} \right] \\
W_{ij} &= \int_{-\infty}^{t} \mathcal{B}(\nu(t')) \exp\left[-\int_{t'}^{t} \mathcal{D}(\nu(t''))dt'' \right] \widetilde{\mathcal{S}}(F_{mn}^{tt'}) \, dt' \\
\nu(t) &= W_{ij}\Gamma_{ij} \\
\widetilde{\mathcal{S}} &= \left\langle \frac{F_{ik}u_k F_{jl}u_l}{|F_{im}u_m|} \right\rangle_0
\end{aligned}
\tag{4.45}
$$

where $W_{ij} = \langle u_i u_j \rangle$ is the second moment of the distribution at time t of the unit orientation vector u_i for tube segments. This is the same as in the case of polymers. The new features of Eq. 4.45 are $\mathcal{B}$ and $\mathcal{D}$, which are the birth rate and death rates for tube segment due to the reaction model. They can be well approximated for $\nu > 0$ by $\mathcal{D} = 1/\tau + \nu$, $\mathcal{B} = 1/\tau$ and for $\nu < 0$, $\mathcal{D} = 1/\tau$, $\mathcal{B} = 1/\tau - \nu$. F_{ij} is the deformation. In the linear viscoelastic limit Eq. 4.45 reduces to the Maxwell model. The solution of Eq. 4.45 in terms of the predicted flow curves is given in Fig. 4.13, taken from reference [23].

In the nonlinear rheology of worm like micelles, one interesting phenomenon is that of shear banding, reviewed in the following references: Refs. [47, 40, 96, 73].

4.5 Shear banding

In worm like micelles above a certain strain rate $\dot{\gamma}_p$, the shear stress σ attains a plateau value $\sigma = \sigma_p$. This plateau value is maintained at this level for at least two decades in $\dot{\gamma} \geq \dot{\gamma}_p$. The normal stress difference N_1 however, continues to increase. This represents shear thinning of a quite drastic kind.

For a shear thinning system such as this, it is now understood that the system forms shear bands. These bands comprise layers of fluid with unequal strain rates
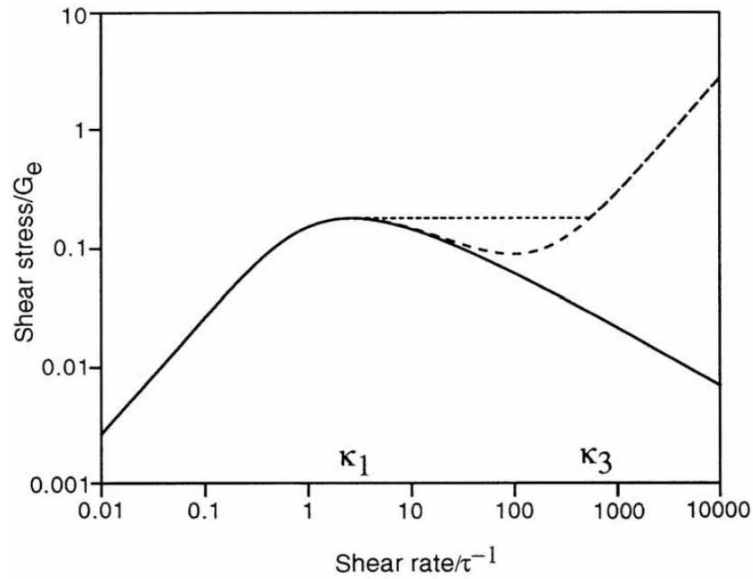
Figure 4.13: Flow curves for reptation-reaction model:solid line, by solution of Eq.4.45. dashed line, with additional quasi-newtonian stress calculated,dotted-line, top-jumping shear-banded solution. Figure from M. E. Cates and S. Fielding, Advances in Physics 55, 799-879 (2006)

but equal stress. The bands can form in the vorticity direction (vorticity banding) or in the gradient direction (gradient banding), in which the normals to the bands are along the velocity gradient direction. (Banding in the velocity direction is also a possibility.)

This is an instability with the following origin: the flow curve $\sigma(\dot{\gamma})$ is a non monotonic curve with increasing and decreasing branches. After attaining a maximum stress σ_p in homogeneous flow, the stress decreases, attaining a minima and then starts to increase linearly again. Flow is unstable on the decreasing branch and thus becomes inhomogeneous, separating into a high shear rate and a low shear rate branch. This hydrodynamical instability can be avoided if we take a gap in the Couette geometry which is smaller than minimum wave length of the fluctuations. It is then possible to trace the full non-monotonic curve.

4.6 Rheological Chaos

New experiments with enhanced spatial and temporal resolution increasingly show that shear banded systems can exhibit complex dynamics. Unusual dynamical steady states are generically obtained in the non-linear flow behaviour of complex fluids driven out of equilibrium[87, 21, 116, 41, 59, 92]. When such fluids are sheared uniformly, the shear stress σ is typically regular at very small shear rates $\dot{\gamma}$. However, at larger shear rates the response is often unsteady, exhibiting oscillations in space and time as a prelude to intermittency and chaos [11, 108, 10, 52, 33]. In this non-linear regime, complex fluids under shear exhibit a variety of instabilities, including instabilities to "shear banded" states[124, 90, 125, 98, 96, 47]. Such banded states arise from an underlying multi-valued constitutive relation connecting the stress and the shear rate, and are often obtained as a precursor to spatio-temporal intermittency and chaotic behaviour in flow response[13, 83, 14, 18, 133, 57, 45, 84, 117].

Such rheological chaos must be a consequence of *constitutive non-linearities*, since Reynolds numbers associated with the flow are too small for convective non-linearities to be important[96, 47]. Such constitutive non-linearities originate in the non-trivial internal structure of the fluid and its coupling to the flow. Recent rheological studies of living polymers obtain an oscillatory stress response to steady shear at shear rates above a threshold value[11, 108, 10, 52]. Such an oscillatory response turns chaotic at still larger shear rates[11, 108, 10, 52].

Although a very large number of experiments on instabilities and "rheological chaos" exist, we will concentrate on describing the work of Sood and collaborators at the Indian Institute of Science, Bangalore over the past decade. Sood and collaborators have pioneered studies of the rheological behaviour in the worm-like micellar system formed by the surfactant CTAT at low concentrations. In Fig. 4.14 the graph between shear stress σ_{xy} and $\dot{\gamma}$, the flow relation, is shown (cf. Ref. [108]). The behaviour in the plateau region exhibits remarkable properties. On applying a shear rate chosen in the plateau region of the flow curve, the stress instead of decaying to a steady state, oscillates in time, as shown in Fig. 4.15, with both a regular and irregular component. These oscillations are not transient.

Sood and collaborators[11] provide a detailed analysis of the oscillatory signal of stress, finding that the signal shows attributes of low dimensional chaos. To do

this, a number N of m dimensional vectors $\vec{X}_i = (\sigma_i, \sigma_{i+L}, \ldots, \sigma_{i+(m-1)L})$, where L is the delay time, are formed from the time series of the stress signal. A embedding theorem of Takens ensures that the dynamics of the original system is represented by $F : \vec{X}_i \to \vec{X}_{i+1}$, provided that m, the embedding dimension, is chosen correctly. One calculates the correlation integral $C(R)$, defined in an m-dimensional phase space, as $C(R) = lim_{N\to\infty} \frac{1}{N^2} \sum_{1,j=1}^{N} H(R - |\vec{X}_i - \vec{X}_j|)$, where $H(x)$ is the Heaviside function.

For small R, $C(R)$ is known to scale as $C(R) \sim R^\nu$ where ν, the *corelation dimension*, gives useful information about the local structure of the attractor. The exponent ν is obtained as a function of $\log(R)$ from the plot of $\log[C(R)]$ versus $\log(R)$. A plateau in the plot of ν versus $\log(R)$ gives the correct ν for a chosen dimension m. The minimum value of m for which the ν saturates is the correct value of m to rpresent the system. Furthermore, if $\nu < m$, then the signal is due to deterministic chaos rather than to random noise.

Sood and collaborators found $\nu = 2.8$ and $m = 4$, showing that the signal exhibits low dimensional chaos. Bandyopadhyay and Sood [10] also found that, with increasing shear rate, the correlation dimension ν, the embedding dimension m and the Lyapunov exponent all increase, showing increased complexity in the dynamics. In Ref. [52] the authors found that adding salt to wormlike micelles leads to a coupling of flow and concentration. In this regime they observe that the plateau found in the shear thinning region of the flow curve attains a slope, as predicted by theory [48].

To confirm this, Sood and collaborators have performed small angle light scattering (SALS) measurements on the sample, in parallel with simultaneous stress relaxation measurement. A butterfly pattern in the intensity of the scattered light is found, confirming the presence of concentration-flow coupling. These authors also found that the signal of the stress in the shear thinning region of the flow curve shows Type II intermittency, leading to a chaotic signal on increasing the shear rate further. The SALS also gives a strong indication that the system is at the threshold of nematic ordering. The signal in orientation fluctuations is correlated with the stress relaxation signal, which become chaotic on increasing the shear rate further.

In Ref. [51], the authors perform a "Granger causality test" on the time series of stress and orientation, finding that the orientation fluctuations have a strong

influence on stress fluctuations. It has been argued that a hydrodynamic descrip-
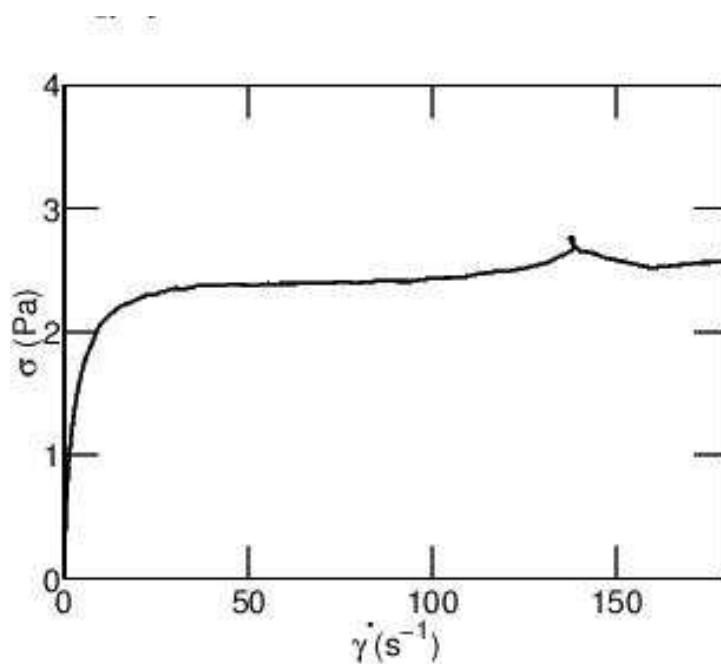
Figure 4.14: The metastable branch of the flow curve of 1.35wt.% CTAT. measured under conditions of controled stress. Figure from R. Bandyopadhyay and A. K. Sood, Europhys Lett 56 447-453 (2001)

tion of this behaviour requires coupling the internal *orientational* state of such a polymeric fluid to the flow. This motivates the study of the problem addressed in the next two chapters. This is the model problem of the spatio-temporal description of an orientable fluid, such as a nematic liquid crystal, placed in a simple steady shear flow[61, 42, 43].

4.6.1 Models for Rheological chaos

There is a substantial body of previous work on the dynamical states of complex fluids under shear. A model due to Fielding and Olmsted expresses the stress as a function of a microstructural parameter chosen, for illustrative purposes, to be the micellar length, which itself evolves in response to the shear rate. The microstructural parameter yields a viscoelastic contribution to the stress, over and above the regular fluid contribution[49]. Fielding and Olmsted show that their
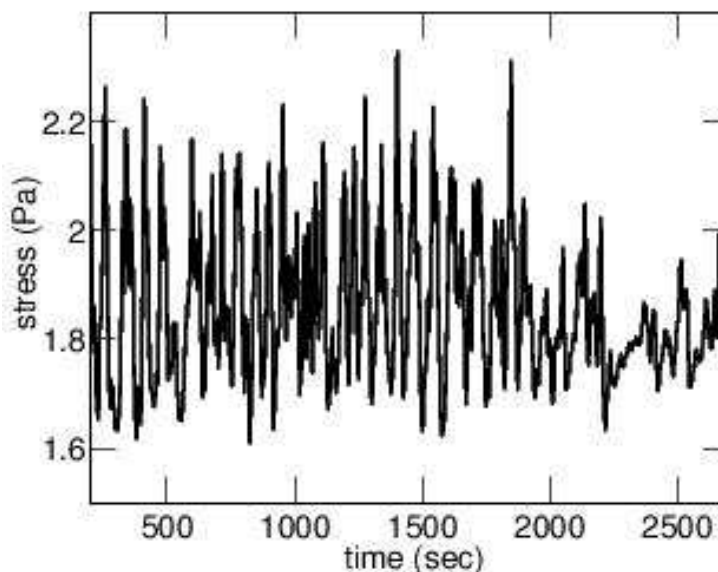
Figure 4.15: The time-dependent relaxation of stress in 1.35wt.% CTAT, on subjecting the sample to a constant step-strain rate of $100s^{-1}$ Figure from R. Bandyopadhyay and A. K. Sood, Europhys Lett 56 447-453 (2001)

model exhibits spatio-temporal rheochaos. Aradian and Cates have proposed a one-dimensional model for the instabilities of a shear-banding fluid system, writing down an equation for the time-variation of the shear stress which depends both on the instantaneous value of the strain rate as well as on the previous history of the stress[9]. This single non-local equation can be cast as two coupled local equations, one for the stress as well as another for a "memory" term, arising out of the single equation for the stress evolution. This simple model yields regimes of periodic as well as chaotic behaviour[9].

Both these models assume simplified scalar descriptions of the internal microstructure. A recent, comprehensive study of a shear-banding interface by Fielding and Olmsted, based on the diffusive Johnson-Segalman (DJS) model, shows that the interaction of multiple shear bands can yield a time-dependent stress response possessing attributes of low-dimensional chaos[50]. However, such approaches do not examine how such a stress response might arise from an underlying microscopic equation of motion. Recent work by Chakraborty, Dasgupta

and Sood on a one-dimensional model for nematic rheochaos extends the model of Refs. [26, 37] by incorporating hydrodynamics, finding stable shear banding as well as the coexistence of banded and spatio-temporally chaotic states[27]. Further, the DJS model is derivable as a specific limit of their model, in which the equation for the order-parameter part of the stress is linearised about the isotropic limit.

4.7 Hydrodynamics of Nematic Fluids

There are several methods to derive the hydrodynamics of nematics. These theories in general follow from the general frame work of classical linear irreversible thermodynamics as discussed, for example, by de Groot and Mazur[55].

In general, the entropy production in the system is calculated from the local conservation laws and the assumption of local thermodynamic equilibrium, in terms of the relevant coarse-grained hydrodynamic variables, including the orientation tensor $q_{\alpha\beta}$. in this derivation it is assumed that we can define thermodynamics quantities as an average over a length scale large with respect to microscopic lengths and small with respect to the length scales of typical gradients characteristic of the non-equilibrium processes[99, 100, 79].

These quantities are then assumed to obey standard thermodynamic relations. One identifies the relevant thermodynamic forces and fluxes in the system from the conjugate pairs that appear in the entropy production relation. Different choices of fluxes and forces may be convenient for different applications [39]. The system is assumed very close to equilibrium so that we may expand the fluxes linearly in the forces. Finally, from the resulting force-flux relation, one uses conservation laws to obtain the equations of motion for $Q_{\alpha\beta}(\mathbf{r}, t)$ and $\mathbf{v}(\mathbf{r},\text{t})$.

The equations for a nematic liquid crystal in terms of the order parameter $\mathbf{Q}$ have been derived by Olmsted in his thesis. To zeroth order the equations are as follows. We define the free energy from

$$\mathcal{F} = \int (F_b + F_g) \, \mathbf{dr}. \tag{4.46}$$

and the molecular field

$$\Phi_{\alpha\beta} = -\frac{\delta\mathcal{F}}{\delta Q_{\alpha\beta}} \tag{4.47}$$

With these,

$$(\partial_t + \mathbf{v} \cdot \nabla)Q_{\alpha\beta} = \underline{(\nabla\mathbf{v})}_{\alpha\gamma}Q_{\gamma\beta} - Q_{\alpha\gamma}\underline{(\nabla\mathbf{v})}_{\gamma\beta} + \beta_1\widehat{(\nabla\mathbf{v})}_{\alpha\beta} + \frac{1}{\beta_2}\widehat{\Phi}_{\alpha\beta} \qquad (4.48)$$

$$(\partial_t + \mathbf{v} \cdot \nabla)v_\alpha = \partial_\gamma\sigma_{\alpha\gamma} \,, \qquad (4.49)$$

where

$$\sigma_{\alpha\beta} = \widehat{\sigma}_{\alpha\beta} + \underline{\sigma}_{\alpha\beta} + \sigma^d_{\alpha\beta} - p\delta_{\alpha\beta} \qquad (4.50)$$

$$\widehat{\sigma}_{\alpha\beta} = \beta_3\widehat{(\nabla\mathbf{v})}_{\alpha\beta} - \beta_1\widehat{\Phi}_{\alpha\beta} \qquad (4.51)$$

$$\underline{\sigma}_{\alpha\beta} = \widehat{\Phi}_{\alpha\gamma}Q_{\gamma\beta} - Q_{\alpha\gamma}\widehat{\Phi}_{\gamma\beta} \qquad (4.52)$$

$$\sigma^d_{\alpha\beta} \equiv \pi^\alpha_{\rho\mu}\partial_\beta Q_{\rho\mu}, \quad \pi^\gamma_{\alpha\beta} \equiv -\frac{\delta\mathcal{F}}{\delta\partial_\gamma Q_{\alpha\beta}} \qquad (4.53)$$

The underline implies the antisymmetric part of the tensor and the $\widehat{}$ symbol requires that we consider the symmetric trace less part of the tensor.

There are other approaches to the same problem, including the Poisson bracket method and molecular model approaches such as the one of Doi and Edwards. A molecular model, due to Hess and co-workers obtains the related equation of motion

$$\frac{d\mathbf{Q}}{dt} - 2\widehat{\mathbf{\Omega} \cdot \mathbf{Q}} - 2\sigma'\widehat{\mathbf{\Gamma} \cdot \mathbf{Q}} + \tau_Q^{-1}\mathbf{\Phi} = -\sqrt{2}\frac{\tau_{ap}}{\tau_a}\mathbf{\Gamma}. \qquad (4.54)$$

This equation is derived for particles of spheroidal shape. These reduce to rods of negligible diameter at $\sigma' = 0$; we will use $\sigma' = 0$ in all our numerical calculation. This choice ensures that the two equations of motion above for the order parameter coincide.

If the non linear part of the $\mathbf{\Phi}$ is dropped, then $\widehat{\sigma}_{\alpha\beta}$ can be replaced in place of $\mathbf{Q}$ in the equation 4.48. This recovers the Johnson-Segalman model.

4.8 Coupled Map Lattices

Coupled map lattices (CML) are basic models for the time evolution of nonlinear systems which are extended in space or involve many individual units. A CML is a discrete time dynamical system generated by a mapping acting on real (vector) sequences. The characteristic features of coupled map lattices are

- They obey discrete time dynamics

- They possess a discrete nature of the underlying space (lattice or network)

- The local variables consist of real numbers or real vectors

The typical and most studied example is the model introduced by Kaneko in 1983. It is given by the following iterations

$$u_s^{t+1} = (1 - \epsilon)f(u_s^t) + \frac{\epsilon}{2}\{f(u_{s-1}^t) + f(u_{s+1}^t)\} \quad t \in \mathbb{N}, \ \epsilon \in [0, 1] \tag{4.55}$$

where $u_s^t \in \mathbb{R}$ and f is a real map.

The configurations $\{u_s^t\}$ may represent the spatial profile of a chemical concentration, of a population density, of a velocity field etc. In these cases, the configurations are bounded sequences, sometimes finite or periodic. Some systems may require unbounded configurations, for example the Frenkel-Kontorova model [30]. CMLs were independently introduced by K. Kaneko, R Kapral and S. Kuzentsov in 1983-84 [68, 69, 131, 75, 80, 81]. A comprehensive set of results for CML's can be found in Refs. [36, 1, 2, 29].

The dynamics of a CML is governed by two competing terms. One is an individual nonlinear reaction represented by f, while the second is a spatial interaction (coupling) with variable intensity ϵ. In the basic model, the interaction is a convolution operator which represents a diffusive coupling. This simple formulation makes the coupled map latticd a paradigm of nonlinear spatially extended dynamical systems. In particular, CMLs are specially designed to facilitate computer simulations over large space-time domains. The simulations exhibit a extraordinary variety of behaviours upon changes in the local map and in the interaction. This diverse phenomenology motivates the application of CML to the simulation of real systems. (For instance, a recent spectacular application can be found in cloud simulations by CML's in Ref. [93]).

The dynamics of spatially extended systems is traditionally described by partial differential equations (PDEs). CMLs provide simpler models where one can usually safely assume that dynamics of local components of the field (local dynamics systems or local maps) is well known, enabling the isolation of the effects of spatial interactions. CMLs are, in a sense, ideal models for computer simulations since they are discrete in space. Therefore, they allow a direct numerical simulation

without the requirement for the complex discretization schemes required for the solution of PDEs. This crucial feature of CML was used extensively by Kaneko, who produced a large variety of numerical studies of CML, providing visualizations of a large number of spatio-temporal patterns exhibiting different regimes of dynamics [69, 72].

4.9 Summary of Work on Rheochaos

In the fifth chapter we propose and study a local map capable of describing the full variety of dynamical states, ranging from regular to chaotic, obtained when a nematic liquid crystal is subjected to a steady shear flow. We have explored many alternative formulation of the map and discussed there problems. In particular we have discuss the map in terms of a quaternion parametrization of rotations of the local frame described by the axes of the nematic director, subdirector, and the joint normal to these, with two additional scalars describing the strength of ordering. Our model yields kayaking, wagging, tumbling, aligned, and coexistence states, accommodated in a phase diagram which closely resembles phase diagrams obtained using representations of the dynamics which are based on ordinary differential equations. We also study the behaviour of the map under periodic perturbations of the shear rate. Such a map can serve as a building block for the construction of lattice models of the complex spatiotemporal states predicted for sheared nematics.

In the sixth chapter, we propose a coupled map lattice (CML) model for such complex spatio-temporal behaviour in a passively sheared nematic liquid crystal, using local maps constructed so as to accurately describe the spatially homogeneous case. Such local maps are coupled diffusively to nearest and next nearest neighbours to mimic the effects of spatial gradients in the underlying equations of motion. We investigate the dynamical steady states obtained as parameters in the map and the strength of the spatial coupling are varied, studying local temporal properties at a single site as well as spatio-temporal features of the extended system. Our methods reproduce the full range of spatio-temporal behaviour seen in earlier one-dimensional studies based on partial differential equations. We report results for both the one and two-dimensional cases, showing that spatial coupling favours uniform or periodically time-varying states, as intuitively expected.

We demonstrate and characterise regimes of spatio-temporal intermittency out of which chaos develops. Our work suggests that such simplified lattice representations of the spatio-temporal dynamics of complex fluids under shear may provide useful insights as well as fast and numerically tractable alternatives to continuum representations.

5

Regular and Chaotic States in a Local Map Description of Sheared Nematic Liquid Crystals

5.1 Introduction

Recent rheological studies of "living polymers", solutions of worm-like micelles in which the energies for scission and recombination are thermally accessible, obtain an oscillatory response to steady shear at low shear rates which turns chaotic at larger shear rates[11, 52]. It has been argued that a hydrodynamic description of this behaviour requires a field describing the local orientation of the polymer, motivating a treatment of the problem of an orientable fluid, such as a nematic, in a uniform shear flow[61, 42, 43].

Nonlinear relaxation equations for the symmetric, traceless second rank tensor $\mathbf{Q}$ characterising local order in a sheared nematic have been derived [61, 42, 43, 62, 102, 82, 97, 126]. Assuming spatial uniformity, a system of 5 coupled ordinary differential equations (ODEs) for the 5 independent components of $\mathbf{Q}$ in a suitable tensor basis is obtained. Solving this system of equations yields a complex phase diagram admitting many states – aligned, tumbling, wagging, kayak-wagging, kayak-tumbling and chaotic – as functions of the shear rate $\dot{\gamma}$ and a phenomenological relaxation time which is a parameter in the equations of motion[112, 113, 56]. Recent work adds spatial variations: numerical studies of the partial differential equations thus obtained yield a phase diagram containing

spatio-temporally regular, intermittent and chaotic states[26, 37].

The degrees of freedom which enter a coarse-grained description of an orientable fluid are mesoscopic. Spatio-temporal structure arises from the coupling of locally ordered regions, through processes such as molecular diffusion, flow-induced dissipation and advection. A powerful approach to understanding complex spatio-temporal dynamics is based on the study of coupled map lattices, a numerical scheme in which maps placed on the sites of a lattice evolve both via local dynamics as well as through couplings to neighbouring sites[1]. However, the utility of this methodology in a specific context is often severely limited by the availability of local maps able to describe the spatially uniform case. This chapter addresses this requirement in the context of a model for rheochaos, proposing the first local map description of the regular and chaotic states obtained in sheared nematics.

5.2   Equation of Motion for Nematics

The hydrodynamic equation of motion for nematics has been presented in the previous chapter, in the form of Eqns. 4.48. Since our results will be compared with the work of Hess and collaborators in Ref. [113], we will use their notation.

The equation of motion used by Hess and co-workers (Eq. 5.1) is closely related to the equation of motion of Eq. 4.48. The difference is that Eqn. 5.1 is derived for particles of spheroidal shape. This shape reduces to the shape of a rod with negligible diameter at $\sigma' = 0$. We will use $\sigma' = 0$ in all our numerical calculations.

We will also neglect spatial variation since our interest is in the construction of a *local* map for nematodynamics. Extensions to models with spatial coupling will be discussed in the following chapter.

Defining $\widehat{\mathbf{b}} := \frac{1}{2}(\mathbf{b} + \mathbf{b}^T) - \frac{1}{3}(tr\mathbf{b})\delta$ to be the symmetric-traceless part of the second-rank tensor $\mathbf{b}$, the equation of motion for $\mathbf{Q}$ in a passive velocity field is, in the notations of Refs. [61, 113]:

$$\frac{d\mathbf{Q}}{dt} - 2\widehat{\boldsymbol{\Omega} \cdot \mathbf{Q}} - 2\sigma'\widehat{\boldsymbol{\Gamma} \cdot \mathbf{Q}} + \tau_Q^{-1}\boldsymbol{\Phi} = -\sqrt{2}\frac{\tau_{ap}}{\tau_a}\boldsymbol{\Gamma} \qquad (5.1)$$

where the tensor $\boldsymbol{\Omega} = \frac{1}{2}((\nabla\mathbf{v})^T - \nabla\mathbf{v})$, $\boldsymbol{\Gamma} = \frac{1}{2}((\nabla\mathbf{v})^T + \nabla\mathbf{v})$ and $\nabla\mathbf{v}$ is the velocity gradient tensor, with $\mathbf{v} = \dot{\gamma}y\mathbf{e^x}$, where $\mathbf{e^x}$ is a unit vector in the $x-$ direction. The

velocity is along the x direction, the velocity gradient is along the y direction, while z is the vorticity direction. The quantities $\tau_a > 0$ and τ_{ap} are phenomenological quantities related to relaxation times, σ' describes the change of alignment caused by $\mathbf{\Gamma}$ and $\mathbf{\Phi} = \partial\phi/\partial\mathbf{Q}$, with $\phi(\mathbf{Q}) = \frac{1}{2}A\mathbf{Q}:\mathbf{Q} - \frac{1}{3}\sqrt{6}B(\mathbf{Q}\cdot\mathbf{Q}):\mathbf{Q} + \frac{1}{4}C(\mathbf{Q}:\mathbf{Q})^2$. The notation $Q:Q$ represents $Q_{ij}Q_{ji}$, with repeated indices summed over. Here $A = A_0(1 - T^*/T)$, and B and C are constrained by the conditions $A_0 > 0$, $B > 0, C > 0$ and $B^2 > \frac{9}{2}A_0C$.

Scaling $t = t^*\tau_a/A_k$, $\mathbf{v} = \mathbf{v}^*A_k/\tau_a$ and $a = a^*a_k$, Eqn. (6.2) can be written in dimensionless form,

$$\frac{d\mathbf{Q}^*}{dt^*} - 2\widehat{\mathbf{\Omega}^*.\mathbf{Q}^*} - 2\sigma'\widehat{\mathbf{\Gamma}^*.\mathbf{Q}^*} + (\theta\mathbf{Q}^* - 3\sqrt{6}\widehat{\mathbf{Q}^*.\mathbf{Q}^*} + 2(\mathbf{Q}^*:\mathbf{Q}^*)\mathbf{Q}^*) = \sqrt{\frac{3}{2}}\lambda_k\mathbf{\Gamma}^* \quad (5.2)$$

where $A_k = A_0(1 - T^*/T_k) = 2B^2/9C, a_k = a_{eq}(T_k) = 2B/3C$ is the (nonzero) equilibrium value of the scalar order parameter a at the transition temperature T_k, $\lambda_k = -\frac{2}{3}\sqrt{3}\frac{\tau_{ap}}{\tau_a a_k}$ and $\theta = (1 - \frac{T^*}{T})/(1 - \frac{T^*}{T_k})$ is the reduced temperature.

5.3 Nematodynamics and Quaternion Algebras

There is, in general, no systematic procedure for the construction of such maps. However, it is reasonable to require that any such map should accurately reproduce the full variety of states obtained through the study of the corresponding ODEs. It should also enable useful physical insights through a sensible choice of physical variables. One obvious possibility is simply the discretization of the governing ODEs. Such a choice of variables, however, is not particularly illuminating as these equations are formulated in terms of the components of $\mathbf{Q}$ in a specific space-fixed tensor basis, rather than in terms of variables more natural to the problem.

We have thus explored an alternative formulation of this problem, constructing a local map in terms of quaternion variables. These variables encode the dynamics of the orthogonal set of axes associated with the eigenvectors of $\mathbf{Q}$, *i.e.* the director, sub-director and the joint normal to these. Our approach incorporates biaxiality, is formulated in terms of physically accessible variables and is computationally straightforward to implement. Our results, summarized in the phase diagram of Fig. 5.1, are in good agreement with previous work based on ODEs

[113], but provide an efficient alternative to such methods. (As is common in high dimensional complex systems, there is the possibility of coexistence of different dynamical states; our phase diagram shows the dominant attractor of the dynamics.)

5.3.1 Orthogonal Tensor Basis

One way to expand the alignment tensor way is as follows,

$$\mathbf{Q} = \sum_{k=0}^{4} a_k \mathbf{T^k}, \tag{5.3}$$

with

$$\mathbf{T^0} = \sqrt{3/2}\widehat{\mathbf{e}^z\mathbf{e}^z}, \quad \mathbf{T^1} = \sqrt{1/2}(\mathbf{e}^x\mathbf{e}^x - \mathbf{e^y}\mathbf{e^y}),$$

$$\mathbf{T^2} = \sqrt{2}\widehat{\mathbf{e}^x\mathbf{e}^y}, \quad \mathbf{T^3} = \sqrt{2}\widehat{\mathbf{e}^x\mathbf{e}^z}, \quad \mathbf{T^4} = \sqrt{2}\widehat{\mathbf{e}^y\mathbf{e}^z}. \tag{5.4}$$

where $\mathbf{T}^k$'s are the orthogonal basis tensor

$$\Rightarrow \mathbf{T}^i : \mathbf{T}^k = \delta_{ik}. \tag{5.5}$$

The dynamical equation for the alignment tensor in shear flow is given by [113]

$$
\begin{aligned}
\dot{a_0} &= -(\theta - 3a_0 + 2a^2)a_0 - 3(a_1^2 + a_2^2) + \frac{3}{2}(a_3^2 + a_4^2) - \frac{3}{2}\sqrt{3}\sigma'\dot{\gamma}a_2, \\
\dot{a_1} &= -(\theta + 6a_0 + 2a^2)a_1 + \dot{\gamma}a_2 + \frac{3}{2}\sqrt{3}(a_3^2 - a_4^2), \\
\dot{a_2} &= -(\theta + 6a_0 + 2a^2)a_2 - \dot{\gamma}a_1 + 3\sqrt{3}a_3a_4 + \frac{\sqrt{3}}{2}\lambda_k\dot{\gamma} - \frac{1}{3}\sqrt{3}\sigma'\dot{\gamma}a_0, \\
\dot{a_3} &= -(\theta - 3a_0 + 2a^2)a_3 + \frac{1}{2}\dot{\gamma}(\sigma' + 1)a_4 + 3\sqrt{3}(a_1a_3 + a_2a_4), \\
\dot{a_4} &= -(\theta - 3a_0 + 2a^2)a_4 + \frac{1}{2}\dot{\gamma}(\sigma' - 1)a_3 + 3\sqrt{3}(a_2a_3 - a_1a_4), \tag{5.6}
\end{aligned}
$$

where $a^2 = a_0{}^2 + a_1{}^2 + a_2{}^2 + a_3{}^2 + a_4{}^2$, This parameterization suits PDE-based numerical approaches but the physical interpretation of the results directly in these variables is more problematic. We thus address the problem of the dynamics of the orientation tensor by posing the problem in terms of a map involving quaternion variables.

5.3.2 Quaternion

Definition

Quaternions are members of an algebra with parameters $(e_0, e_1, e_2, e_3) \in \mathbf{R}$, represented as

$$\mathbf{q} = \{e_0 + e_1 i + e_2 j + e_3 k\} \tag{5.7}$$

where addition is defined by

$$\{e_0 + e_1 i + e_2 j + e_3 k\} + \{b_0 + b_1 i + b_2 j + b_3 k\} = (e_0 + b_0) + (e_1 + b_1)i + (e_2 + b_2)j + (e_3 + b_3)k, \tag{5.8}$$

and multiplication with $\mathbf{q_1} = b_0 + b_1 i + b_2 j + b_3 k$

$$
\begin{aligned}
\mathbf{q}.\mathbf{q_1} = \ & (e_0.b_0 - e_1.b_1 - e_2.b_2 - e_3.b_3) \\
& + (e_2.b_3 - e_3.b_2 + e_0.b_1 + e_1.b_0)i \\
& + (e_3.b_1 - e_1.b_3 + e_0.b_2 + e_2.b_0)j \\
& + (e_3.b_1 - e_1.b_3 + e_0.b_3 + e_3.b_0)k
\end{aligned} \tag{5.9}
$$

Using the distributive law and then applying the law

$$i^2 = j^2 = k^2 = ijk = -1, . \tag{5.10}$$

and

$$ij = k, \ ji = -k, \ jk = i, \ kj = -i, \ ki = j, \ ik = -j. \tag{5.11}$$

The unit quaternion is defined as $e_0^2 + e_1^2 + e_2^2 + e_3^2 = 1$

5.3.3 Relation to the Rotation

A Rotation matrix represented in terms of quaternion parameters is given by

$$\mathbf{A} = \begin{bmatrix} e_0^2 + e_1^2 - e_2^2 - e_3^2 & 2(e_1 e_2 + e_0 e_3) & 2(e_1 e_3 - e_0 e_2) \\ 2(e_1 e_2 - e_0 e_3) & e_0^2 - e_1^2 + e_2^2 - e_3^2 & 2(e_2 e_3 - e_0 e_1) \\ 2(e_1 e_3 + e_0 e_2) & 2(e_2 e_3 - e_0 e_1) & e_0^2 - e_1^2 - e_2^2 + e_3^2 \end{bmatrix} \tag{5.12}$$

One can transform from space coordinates to body fixed axes by the equation
$x' = \mathbf{A}x$, with the constraint $e_0^2 + e_1^2 + e_2^2 + e_3^2 = 1$

5.3.4   Relation to Euler angle

In the convention we are using, the relation between the quaternion parameter and
Euler angles are given by

$$
\begin{aligned}
e_0 &= \cos\frac{\psi+\phi}{2}\cos\frac{\theta}{2} \\
e_1 &= \cos\frac{\psi-\phi}{2}\sin\frac{\theta}{2} \\
e_2 &= \cos\frac{\psi-\phi}{2}\sin\frac{\theta}{2} \\
e_3 &= \cos\frac{\psi+\phi}{2}\cos\frac{\theta}{2}
\end{aligned}
\tag{5.13}
$$

It is clear from these relations that there is no ambiguity in the value of quaternion
parameter at $\theta = 0, or \pi$. Moreover it is very easy to check numerical errors.

5.3.5   Quaternions and the Alignment Tensor

As discussed above, the $\mathbf{Q}$ tensor admits the following parametrization: $Q_{ij} = \frac{3s_1}{2}\left(n_i n_j - \frac{1}{3}\delta_{ij}\right) + \frac{s_2}{2}\left(m_i m_j - l_i l_j\right)$, where s_1 and s_2 represent the magnitude of
the ordering along $\mathbf{n}$ (the director) and $\mathbf{m}$ (the subdirector), with $\mathbf{n}$ and $\mathbf{m}$ unit
vectors and $\mathbf{l} = \mathbf{n} \times \mathbf{m}$. The dynamics of $\mathbf{Q}$ thus involves both the dynamics of
the frame defined by $\mathbf{n}, \mathbf{m}$ and $\mathbf{l}$ as well as the dynamics of s_1 and s_2.

The frame dynamics can be represented in many equivalent ways, such as
through coordinate matrices, axis-angle or Euler angle representations. However,
the coordinate matrix representation requires a large number of parameters, the
axis-angle representation suffers from redundancy and the use of the Euler-angle
representation is marred by the "gimbal-lock" problem[6]. Our parametrization of
the frame dynamics uses quaternion variables, providing an elegant, compact and
numerically stable alternative to these representations.

Equations for $\dot{\mathbf{n}}$, $\dot{\mathbf{m}}$ and $\dot{\mathbf{l}}$ as well as for the order parameter amplitudes $\dot{s_1}$
and $\dot{s_2}$ can be derived by considering a reference frame in which the director and
subdirector are stationary (body frame). In the body frame, denoted by primed

vectors, the director can be chosen to be $\mathbf{n}' = (1,0,0)$, the subdirector to be $\mathbf{m}' = (0,1,0)$, with $\mathbf{l}' = (0,0,1)$. The transformation matrix $\mathbf{A}$ which maps vectors from the lab frame to the body frame, can be defined in terms of quaternion parameters $(e_0, \ldots, e_3)$ constrained by $e_0^2 + e_1^2 + e_2^2 + e_3^2 = 1$. This transformation matrix has the form

$$
\mathbf{A} = \begin{pmatrix} n_x & n_y & n_z \\ m_x & m_y & m_z \\ l_x & l_y & l_z \end{pmatrix} = \begin{bmatrix} e_0^2 + e_1^2 - e_2^2 - e_3^2 & 2(e_1 e_2 + e_0 e_3) & 2(e_1 e_3 - e_0 e_2) \\ 2(e_1 e_2 - e_0 e_3) & e_0^2 - e_1^2 + e_2^2 - e_3^2 & 2(e_2 e_3 - e_0 e_1) \\ 2(e_1 e_3 + e_0 e_2) & 2(e_2 e_3 - e_0 e_1) & e_0^2 - e_1^2 - e_2^2 + e_3^2 \end{bmatrix}
$$

5.3.6 Dynamical Equation for the Alignment Tensor

We now discuss the equation for the alignment tensor in terms of quaternions. Putting $\sigma' = 0$ in the above equations we get,

$$
\dot{s_1} = \frac{1}{6} \left(9 \sqrt{6}\, s_1^2 - 18\, s_1^3 - 3 \sqrt{6}\, s_2^2 + 2\, s_1 \left(-3\, s_2^2 - 3\, \theta \right) + 3 \sqrt{6}\, n_x\, n_y\, \dot{\gamma}\, \lambda_k \right)
$$

$$
\dot{s_2} = -3 \sqrt{6}\, s_1\, s_2 - 3\, s_1^2\, s_2 - s_2 \left(s_2^2 + \theta \right) - \sqrt{\frac{3}{2}} \left(l_x\, l_y - m_x\, m_y \right) \dot{\gamma}\, \lambda_k
$$

$$
\dot{e_0} = \frac{1}{4} \dot{\gamma}\, e_3 + \frac{1}{4} \sqrt{\frac{3}{2}}\, \dot{\gamma} \left(-\frac{(l_y\, m_x + l_x\, m_y)\, e_1}{s_2} + \frac{2\, (l_y\, n_x + l_x\, n_y)\; e_2}{3\, s_1 + s_2} + \frac{2\, (m_y\, n_x + m_x\, n_y)\, e_3}{-3\, s_1 + \; s_2} \right) \lambda_k
$$

$$
\dot{e_1} = \frac{1}{4} \dot{\gamma}\, e_2 + \frac{1}{4} \sqrt{\frac{3}{2}}\, \dot{\gamma} \left(\frac{(l_y\, m_x + l_x\, m_y)\, e_0}{s_2} - \frac{2\; (m_y\, n_x + m_x\, n_y)\, e_2}{-3\, s_1 + s_2} + \frac{2\, (l_y\, n_x + l_x\, n_y)\; e_3}{3\, s_1 + s_2} \right) \lambda_k
$$

$$
\dot{e_2} = -\frac{1}{4} \dot{\gamma}\, e_1 + \frac{1}{4} \sqrt{\frac{3}{2}}\, \dot{\gamma} \left(-\frac{2\, (l_y\, n_x + l_x\, n_y)\, e_0}{3\, s_1 + s_2} + \frac{2\, (m_y\, n_x + m_x\, n_y)\, e_1}{-3\, s_1 \; + s_2} + \frac{(l_y\, m_x + l_x\, m_y)\, e_3}{s_2} \right) \lambda_k
$$

$$\dot{e}_3 = -\frac{1}{4}\,\dot{\gamma}\,e_0 + \frac{1}{4}\sqrt{\frac{3}{2}}\,\dot{\gamma}\,(-\frac{2\,(m_y\,n_x + m_x\,n_y)\,e_0}{-3\,s_1 + s_2} - \frac{2\,(l_y\,n_x + l_x\,n_y)\,e_1}{3\,s_1 + s_2} - \frac{(l_y\,m_x + l_x\,m_y)\,e_2}{s_2})\,\lambda_k$$
$$(5.14)$$

where n_x , m_y , m_x , m_y , l_x and l_y are components of the director and subdirector
and $\mathbf{l} = \mathbf{n} \times \mathbf{m}$. These are given in terms of quaternion parameters as follows

$$n_x = e_0^2 + e_1^2 - e_2^2 - e_3^2, \quad n_y = 2(e_1 e_2 + e_0 e_3), \quad m_x = 2(e_1 e_2 - e_0 e_3),$$

$$m_y = e_0^2 - e_1^2 + e_2^2 - e_3^2, \quad \text{and } l_x = 2(e_1 e_3 + e_0 e_2), \quad l_y = 2(e_2 e_3 - e_0 e_1)$$

For illustration, a rigid body rotated with constant angular velocity is represented
by the equations

$$\dot{e}_0 = \frac{1}{4}\dot{\gamma}e_3, \quad \dot{e}_1 = \frac{1}{4}\dot{\gamma}e_2, \quad \dot{e}_2 = -\frac{1}{4}\dot{\gamma}e_1, \quad \dot{e}_3 = -\frac{1}{4}\dot{\gamma}e_0. \qquad (5.15)$$

5.4   Local Map in terms of Quaternions

The quantities $\mathbf{n} = (n_x, n_y, n_z), \mathbf{m} = (m_x, m_y, m_z)$ and $\mathbf{l} = (l_x, l_y, l_z)$ are easily
obtained using this mapping, yielding ODE's for the parameters $s_1, s_2, e_0, e_1, e_2, e_3$.
These are converted into a map using a first-order Euler scheme. After each discrete
time step, we renormalise the quaternion variable. Choosing σ' and θ equal to zero
for all the results reported here in common with earlier work, our map is then

defined through

$$s_1^{t+1} = s_1^t + \Delta \left(\frac{1}{6} \{ 9\sqrt{6}\, s_1^2 - 18\, s_1^3 - 3\sqrt{6}\, s_2^2 - 6\, s_1\, s_2^2 + 3\sqrt{6}\, n_x\, n_y\, \dot{\gamma}\, \lambda_k \} \right)^t$$

$$s_2^{t+1} = s_2^t + \Delta \left(-3\sqrt{6}\, s_1\, s_2 - 3\, s_1^2\, s_2 - s_2^3 - \sqrt{\frac{3}{2}}\, (l_x\, l_y - m_x\, m_y)\, \dot{\gamma}\, \lambda_k \right)^t$$

$$e_0^{t+1} = e_0^t + \Delta \left(\frac{1}{4}\dot{\gamma}\, e_3 + \frac{1}{4}\sqrt{\frac{3}{2}}\, \dot{\gamma}\, \{ -\frac{(l_y\, m_x + l_x\, m_y)\, e_1}{s_2} + \frac{2\,(l_y\, n_x + l_x\, n_y)\, e_2}{3\, s_1 + s_2} \right.$$

$$\left. + \frac{2\,(m_y\, n_x + m_x\, n_y)\, e_3}{-3\, s_1 + s_2} \} \, \lambda_k \right)^t$$

$$e_1^{t+1} = e_1^t + \Delta \left(\frac{1}{4}\dot{\gamma}\, e_2 + \frac{1}{4}\sqrt{\frac{3}{2}}\, \dot{\gamma}\, (\frac{(l_y\, m_x + l_x\, m_y)\, e_0}{s_2} - \frac{2\,(m_y\, n_x + m_x\, n_y)\, e_2}{-3\, s_1 + s_2} \right.$$

$$\left. + \frac{2\,(l_y\, n_x + l_x\, n_y)\; e_3}{3\, s_1 + s_2})\, \lambda_k \right)^t$$

$$e_2^{t+1} = e_2^t + \Delta \left(-\frac{1}{4}\dot{\gamma}\, e_1 + \frac{1}{4}\sqrt{\frac{3}{2}}\, \dot{\gamma}\, (-\frac{2\,(l_y\, n_x + l_x\, n_y)\, e_0}{3\, s_1 + s_2} + \frac{2\,(m_y\, n_x + m_x\, n_y)\, e_1}{-3\, s_1 + s_2} \right.$$

$$\left. + \frac{(l_y\, m_x + l_x\, m_y)\, e_3}{s_2})\, \lambda_k \right)^t$$

$$e_3^{t+1} = e_3^t + \Delta \left(-\frac{1}{4}\dot{\gamma}\, e_0 + \frac{1}{4}\sqrt{\frac{3}{2}}\, \dot{\gamma}\, (-\frac{2\,(m_y\, n_x + m_x\, n_y)\, e_0}{-3\, s_1 + s_2} - \frac{2\,(l_y\, n_x + l_x\, n_y)\, e_1}{3\, s_1 + s_2} \right.$$

$$\left. - \frac{(l_y\, m_x + l_x\, m_y)\, e_2}{s_2})\, \lambda_k \right)^t \tag{5.16}$$

5.5   Numerical Procedures and Results

5.5.1   Numerical Methods

We choose $\Delta = 0.01$ for all our calculations. (The phase boundaries shown in Fig. 5.1 exhibit a weak dependence on Δt. However, provided Δt is chosen small enough, this dependence may be neglected.) The superscript 't' indicates that the

values of the variables are taken at the t'th discrete time step These equations are apparently singular in the three limits $s_2 \rightarrow 0, 3s_1 + s_2 \rightarrow 0$ and $3s_1 - s_2 \rightarrow 0$, when denominators containing these quantities approach zero. This happens at isolated points in the dynamical evolution of the map, when the system is rendered effectively uniaxial, as a consequence of eigenvalues along two orthogonal axes becoming degenerate. We deal with this in two ways. First, we can set these terms the denominator to a small constant whenever they reach a preset value close to zero, so that these terms never actually cross zero. Alternatively, we may use the freedom to choose the degenerate eigenvectors in such a way as to cancel the term which vanishes in the denominator. In practice, both schemes give equivalent results. We also note that the systems is always effectively biaxial due to the shear.

The control parameters are the dimensionless shear rate $\dot{\gamma}$ and λ_k. In place of the 5 coupled ODE's used in the conventional parametrization of the dynamics of $\mathbf{Q}$, we have 6 equations constrained by the normalization requirement, thereby conserving the number of degrees of freedom.

In our numerical analysis of the map, we start typically from random initial conditions, omitting sufficient transients ($\sim 10^5$ time steps) to ensure that the asymptotic attractor of the dynamics is reached. Our analysis includes inspection of the (i) power spectrum, (ii) phase portraits, (iii) bifurcation diagrams and (iv) time series of the different relevant variables.

5.5.2   Results

Figs. 5.2 and 5.3 show the variety of states obtained in our numerical calculations. Each sub-figure, labelled as Figs. 5.2 (a) - (c) and Figs. 5.3 (a)-(c), has the following structure: The first inset, labelled (i) for all figures, describes the time dependence of n_z, the z-component of the director, and the angle ϕ made by the projection of the director on the $x - y$ plane with the $x-$ axis. The second inset, labelled (ii) for all figures, plots the quantities measuring the amount of ordering along director and sub-director against each other, providing the attractor of the system in the $s_1 - s_2$ plane for a generic initial condition. The main panel in each of the sub-figures shows the power spectrum of s_1, $\ln(|A(f)|^2)$ against frequency f on a semi-log plot.

The following states are easily identified: (I) An **Aligned** state denoted as 'A'
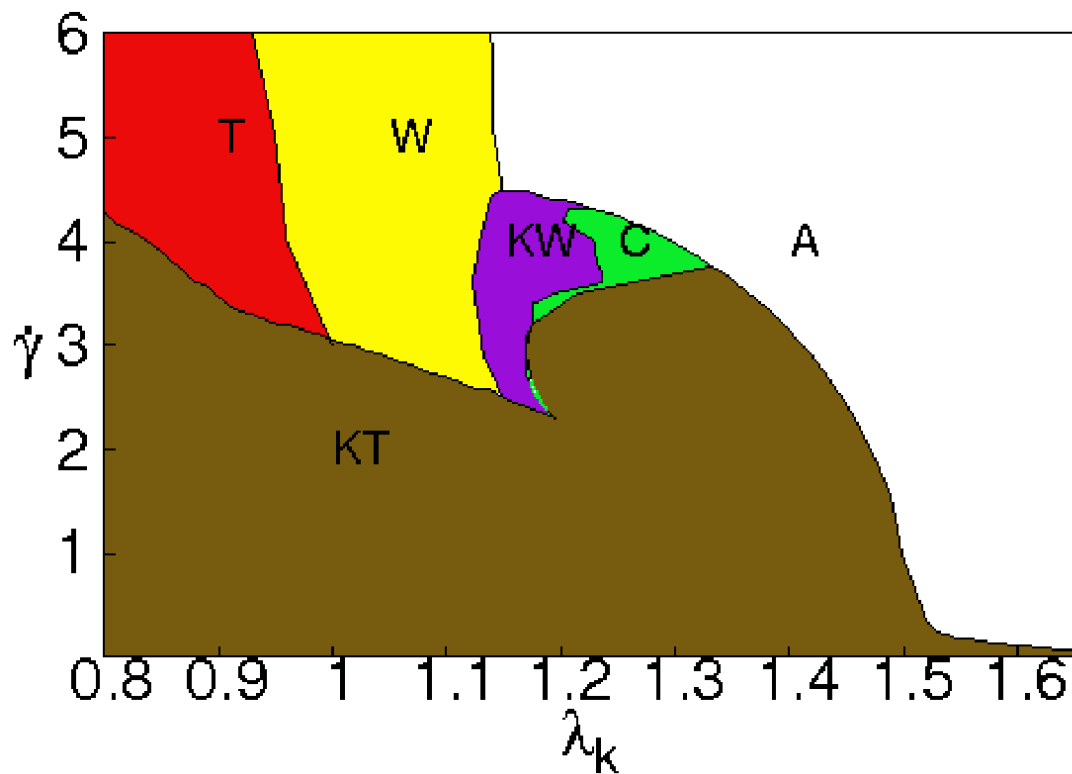
Figure 5.1: The phase diagram of steady states in our model, illustrating regimes
in which the following steady states are obtained for a generic initial condition:
an aligned state denoted as 'A', a tumbling state labelled as 'T', a wagging state
'W', a kayak-tumbling state 'KT', a kayak-wagging state denoted by 'KW' and a
complex state denoted as 'C'. This phase diagram closely resembles phase diagrams
plotted in Refs. [113].
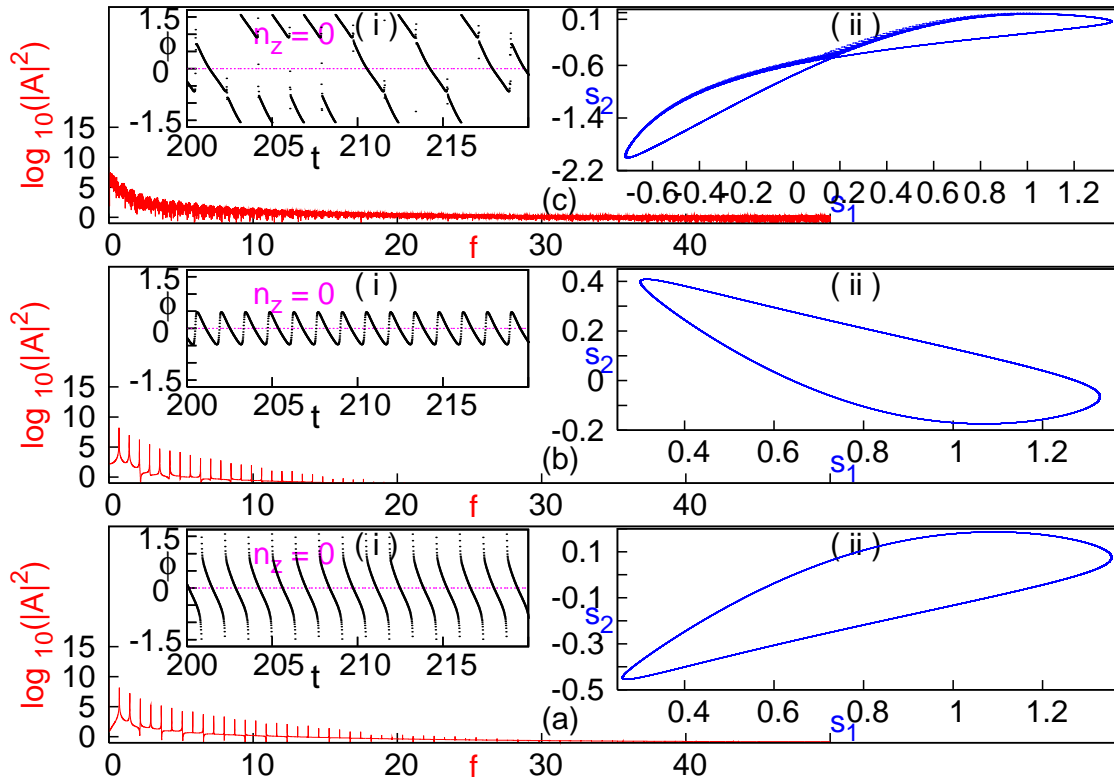
Figure 5.2: The sequence of three main panels shows the power spectrum associated with states in the regimes labelled (a) T and (b) W in the phase diagram of Fig. 5.1. The topmost panel (c) shows a mixed state (M) (not shown separately in Fig. 5.1), associated with the boundary between W and T The inset labelled (i) in all these panels shows typical plots of the time-dependence of the z-component of the director n_z and the angle ϕ made by the projection of the director on the $x - y$ plane with the $x-$ axis. The insets labelled (ii) in all these panels show the trajectory in the $s_1 - s_2$ plane.

Figure 5.3: The sequence of three main panels shows the power spectrum associated
with states in the regimes labelled (a) KT (kayak-tumbling), (b) KW (kayak-
wagging) and (c) C (complex or chaotic) in the phase diagram of Fig. 5.1. The
inset labelled (i) in all these panels shows typical plots of the time-dependence of
the z-component of the director n_z and the angle ϕ made by the projection of the
director on the $x - y$ plane with the $x-$ axis. The insets labelled (ii) in all these
panels show the trajectory in the $s_1 - s_2$ plane.

in the phase-diagram of Fig. 5.1, but omitted, for brevity, from the states shown
in Fig. 5.2 and Fig. 5.3. In the aligned state, neither the frame orientation, nor s_1
and s_2, vary in time. The director is aligned with the flow at a fixed angle; (II)
A **Tumbling** state, in which the director lies in the shear plane (the xy plane)
and rotates about the vorticity direction (the z axis). Fig. 5.2(a)(i) indicates that
this state is a stable in-plane state, since the z-component of the director is zero.
Also, the angle made by the projection of the director on the x-y plane varies
smoothly between $\pi/2$ and $-\pi/2$. Fig. 5.2(a)(ii) shows the periodic character of
this state. This state is labelled as 'T' in the phase-diagram of Fig.5.1; (III) A
Wagging state, in which the director lies in the shear plane, but oscillates between
two values. Note that Fig. 5.2 (b)(i) indicates that this state is a stable in-plane
state. Also, the director oscillates back and forth in-plane as indicated in Fig. 5.2
(b)(ii). Fig. 5.2 (b) shows that this state is a periodic state with sharp delta-
function peaks in the power spectrum. These states are denoted as 'W' in the
phase-diagram in Fig.5.1.

In addition to the states described above, we obtain (IV) A **Kayak-Tumbling**
state, equivalent to the tumbling state, but in which the director is out of the
shear plane. Thus, as shown in Fig. 5.3(a) $n_z \neq 0$ and the projection of the
director on the xy plane rotates through a full cycle. Such states are temporally
periodic, as shown in Fig. 5.3(a); the regular cycles evident in the map of s_1 vs.
s_2 (Fig. 5.3(a)(ii)) is a further indication of periodic behaviour. These states are
noted as 'KT' in the phase-diagram of Fig. 5.1; (V) A **Kayak-Wagging** state
where, as in KT, the director is out of plane, but the projection of the director on
the shear plane oscillates between two values. The properties of such states are
illustrated in Fig. 5.3(b). Such states are again temporally periodic. The cyclic
trajectory of the system in the $s_1 - s_2$ plane (Fig. 5.3(b)(ii)) further confirms such
periodic behaviour. These states are denoted by 'KW' in the phase-diagram of
Fig. 5.1; (VI) A **Mixed** state, typically found close to the boundaries between
wagging and tumbling states, whose properties are illustrated in Fig. 5.2(c). In
such states, the director exhibits both oscillation and complete rotations. Power
spectra obtained at the boundaries of this phase, for example near $\lambda_k = 0.99$ and
$\dot{\gamma} = 4.0$, have a broad range of frequencies, and, (VII) A **Complex** state, in which
the director lies out of the shear plane but both oscillates and rotates. The complex
phase exhibits chaotic behaviour, as can be seen in Fig. 5.3(c). Note that the delta
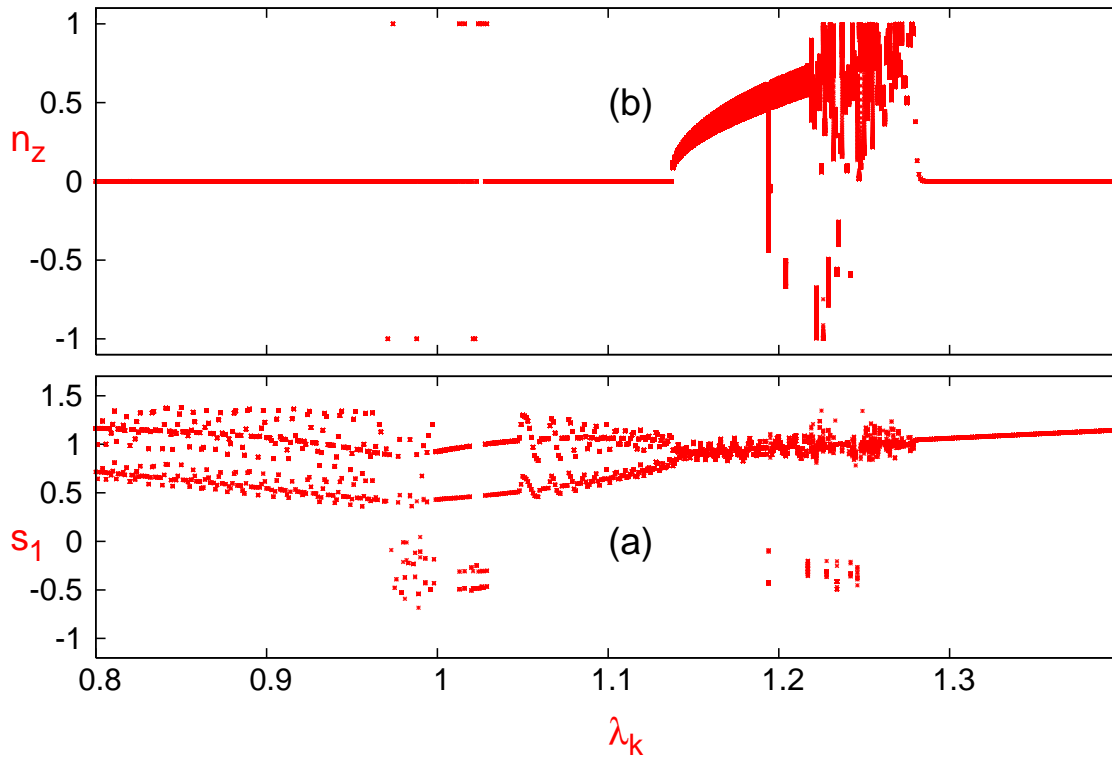
Figure 5.4: Bifurcation diagram obtained for a generic initial condition by varying λ_k at fixed $\dot{\gamma} = 4.0$, showing (a) n_z and (b) a Poincare section of s_1 (with s_2 fixed at the midpoint of the s_2 range) at each point in the bifurcation diagram.

function peaks in the power spectrum exhibited by the periodic states discussed earlier have broadened into a continuum of frequencies. The plot of s_1 vs. s_2 displays no regular structure. These state are noted as 'C' in the phase-diagram in Fig.5.1. In addition to these states, we also obtain a log rolling state in which the director is perpendicular to the shear plane (not shown).

The range of dynamical states manifest in this problem is clearly evident in the bifurcation diagram of Fig. 5.4 which shows a cut in the phase diagram at fixed $\dot{\gamma} = 4.0$, varying λ_k. Such a cut intersects KT, T, W, KW, C and A states in the phase diagram. For specificity we show the quantities n_z and the Poincare section of s_1. It is clearly evident from Fig. 5.4 that $n_z = 0$ for the T, W and A states, while the KT, KW and C states are out-of-plane states with $n_z \neq 0$. Further, the s_1 section, shows a fixed point for the aligned state, regular cycles for the KT, T

98

W and KW states and irregular (chaotic) behavior for the C state.

Finally, we investigate the behaviour of this dynamical system to a class of periodic perturbations constructed by taking $\dot{\gamma} = \dot{\gamma}_0 + \dot{\gamma}_1 \sin{(\omega_a t)}$, with t taken in discrete time and ω_a representing the angular frequency of the applied forcing. This corresponds to the experimental situation in which the steady shear is modulated by a small ($\dot{\gamma}_1 \ll 1$) amplitude periodic perturbation. If $\dot{\gamma}_0$ were strictly zero, this would be the case of purely oscillatory shear. We choose ω_a to be small, so that steady state is easily achieved. We have also investigated the effects of periodic variation of λ_k, finding behaviour similar to that described below.

Our results are summarized in Fig. 5.5 which show the power spectrum of $s_1, \ln(|A(f)|^2)$ against frequency f on a semi-log plot. Data for the states labelled (a) T and (b) C in the phase diagram of Fig. 5.1 are shown. For comparison, we show the unperturbed power spectrum in the lower panel of each figure. Note that the introduction of the time modulation adds an additional periodic component to the signal in the case of the periodic states, such as the T state. The power spectrum shows several harmonics of the intrinsic and driving frequencies as well as linear combinations of these frequencies, consistent with the inherent non-linearity of this system. The peaks in the power spectrum are indexed as shown in the figure. For the state labelled (C) (complex or chaotic), the power spectrum shows broad-band structure as before, indicating that the periodic driving does not serve to stabilize order. These statements remain roughly independent of the amplitude of the periodic perturbation, provided it is not large enough that nearby states in the phase diagram are accessed. The generic features described above continues to hold in the other regions of the phase diagram.

5.6   Discussion and Conclusion

Aradian and Cates have recently studied a minimal model for rheochaos in shear-thickening fluids, using equations which describe a shear-banding system coupled to a retarded stress response[9]. These authors connect their model system to a modified Fitzhugh-Nagumo model, a dynamical system with a variety of interesting and complex phases. Fielding and Olmsted study instabilities in shear-thinning fluids, where the instability originates in the multi-branched character of the con-
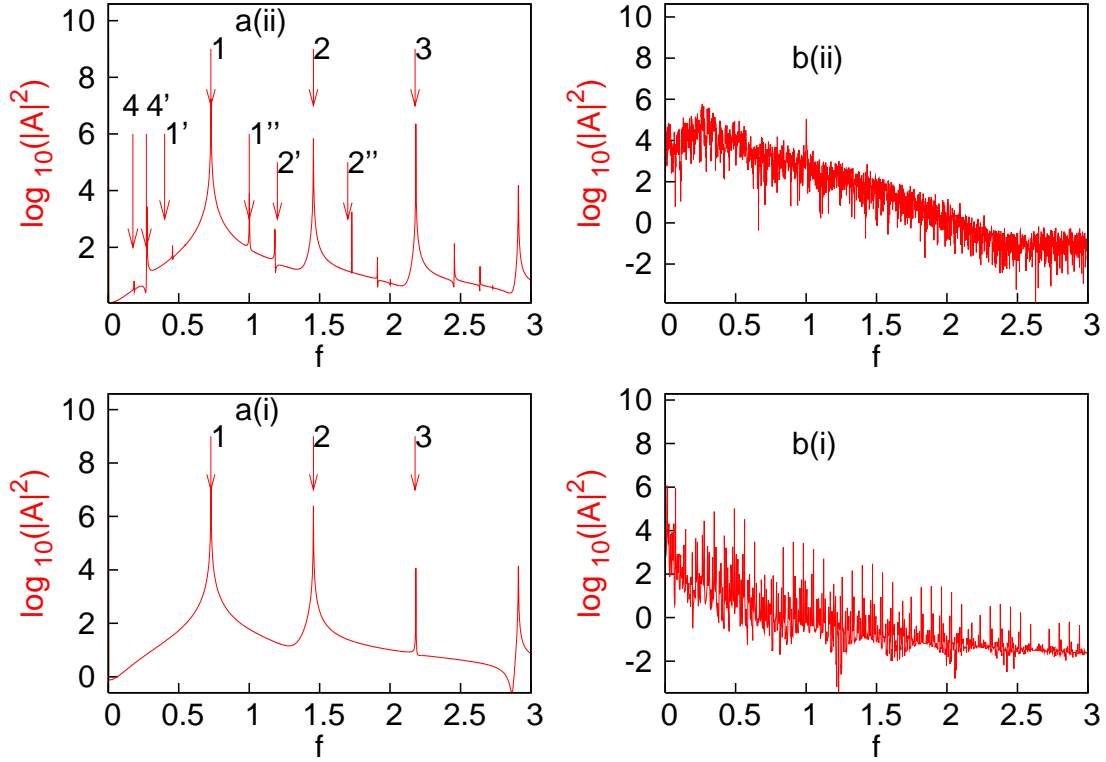
Figure 5.5: The two upper panels (a)(ii) and (b)(ii) show the power spectrum of s_1 against frequency f on a semi-log plot for states corresponding to a representative point in the regimes labelled (a) T and (b) C (complex or chaotic) in the phase diagram of Fig. 5.1. We choose $\dot{\gamma}$ to vary periodically with frequency ω_a, such that $\omega_a = 2\pi\Delta$ and $\gamma_1 = 0.1$. The lower panel, labelled (a)(i) and (b)(i) in both cases show the unperturbed power spectrum. The frequency peaks indicated in (a)(i), the system without periodic forcing, are indexed as follows: $1 = 0.729$ (the fundamental frequency), $2 = 1.456$ (twice the fundamental frequency) and $3 = 2.174$ (three times the fundamental frequency). The fundamental frequency of the applied signal is shown as $4 = 0.184$. The primed peaks indicated in (a)(ii) are combinations of the intrinsic frequency and the frequency of the applied signal and indexed as follows: $1' = 1 - 4'$, $2' = 2 - 4'$, $1'' = 1 + 4'$. Note that the broad-band structure of the power spectrum in b(i) remains intact when the forcing is applied.

stitutive relation[49]. Chakrabarty *et al.* report a study of the PDE's describing
the dynamics of **Q**, characterizing spatio-temporal routes to chaotic behaviour
in sheared nematics [26]. All these studies allow for spatial variation - although
restricted so far to the one-dimensional case - whereas our local map describes
the spatially uniform situation. However, the dynamical system we study is ob-
tained directly from the underlying dynamics, in contrast to the approaches of
Refs. [9, 49]. Whether coupling maps of the sort we construct permits a complete
description of the spatio-temporal structure obtained in Ref. [26] remains to be
seen.

In conclusion, we have proposed a local map describing the variety of dynami-
cal states obtained in a model for sheared nematics. Our phase diagram, Fig. 5.1,
contains all non-trivial dynamical states obtained in previous work. It also closely
resembles, even quantitatively, phase diagrams obtained in previous work which
used ordinary differential equations formulated in continuous time. We have also
studied the behaviour of the map under parametric oscillations of the shear rate,
a physical situation not addressed earlier. Our work thus supplies a crucial ingre-
dient in the construction of coupled map lattice approaches to the spatio-temporal
aspects of rheological chaos, a problem currently at the boundaries of our under-
standing of the dynamics of complex fluids.

6

A Coupled Map Lattice Model for Rheological Chaos in Sheared Nematic Liquid Crystals

6.1   Introduction

Unusual dynamical steady states are obtained in a large number of experiments on complex fluids driven out of equilibrium[87, 21, 116, 41, 59, 92]. When such fluids are sheared uniformly, the shear stress σ is typically regular at very small shear rates $\dot{\gamma}$. However, at larger shear rates the response is often unsteady, exhibiting oscillations in space and time as a prelude to intermittency and chaos [11, 108, 10, 52, 33]. In this non-linear regime, complex fluids under shear exhibit a variety of instabilities, including instabilities to "shear banded" states[124, 90, 125, 98, 96, 47]. Such banded states arise from an underlying multi-valued constitutive relation connecting the stress and the shear rate, and are often obtained as a precursor to spatio-temporal intermittency and chaotic behaviour in flow response[13, 83, 14, 18, 133, 57, 45, 84, 117].

Such rheological chaos must be a consequence of *constitutive non-linearities*, since Reynolds numbers associated with the flow are too small for convective non-linearities to be important[96, 47]. Such constitutive non-linearities originate in the non-trivial internal structure of the fluid and its coupling to the flow. Recent rheological studies of "living polymers" obtain an oscillatory stress response to steady shear at shear rates above a threshold value[11, 108, 10, 52]. Such an

oscillatory response turns chaotic at still larger shear rates[11, 108, 10, 52]. It has been argued that a hydrodynamic description of this behaviour requires coupling the internal *orientational* state of such a polymeric fluid to the flow, motivating the study of the problem addressed in this chapter[26, 37]. This is the model problem of the spatio-temporal description of an orientable fluid, such as a nematic liquid crystal, placed in a simple steady shear flow[61, 42, 43].

There is a substantial body of previous work on the dynamical states of complex fluids under shear. A model due to Fielding and Olmsted expresses the stress as a function of a microstructural parameter chosen, for illustrative purposes, to be the micellar length, which itself evolves in response to the shear rate. The microstructural parameter yields a viscoelastic contribution to the stress, over and above the regular fluid contribution[49]. Fielding and Olmsted show that their model exhibits spatio-temporal rheochaos. Aradian and Cates have proposed a one-dimensional model for the instabilities of a shear-banding fluid system, writing down an equation for the time-variation of the shear stress which depends both on the instantaneous value of the strain rate as well as on the previous history of the stress[9]. This single non-local equation can be cast as two coupled local equations, one for the stress as well as another for a "memory" term, arising out of the single equation for the stress evolution. This simple model yields regimes of periodic as well as chaotic behaviour[9].

Both these models assume simplified scalar descriptions of the internal microstructure. A recent, comprehensive study of a shear-banding interface by Fielding and Olmsted, based on the diffusive Johnson-Segalman (DJS) model, shows that the interaction of multiple shear bands can yield a time-dependent stress response possessing attributes of low-dimensional chaos[50]. However, such approaches do not examine how such a stress response might arise from an underlying microscopic equation of motion. Recent work by Chakraborty, Dasgupta and Sood on a one-dimensional model for nematic rheochaos extends the model of Refs. [26, 37] by incorporating hydrodynamics, finding stable shear banding as well as the coexistence of banded and spatio-temporally chaotic states[27]. Further, the DJS model is derivable as a specific limit of their model, in which the equation for the order-parameter part of the stress is linearized about the isotropic limit.

In this chapter, we present results from a comprehensive study of a simple coupled map lattice model for rheological chaos, as appropriate to nematic systems

under steady shear. Our local "microstructural" variable represents the orientation
and degree of coarse-grained order of nematic molecules in the flow, as in the work
of Refs. [27, 26, 37]. We compute the contribution to shear stresses arising from
the evolution of this local variable, showing how uniform, periodic and spatio-
temporally chaotic behaviour in this quantity can be accessed.

The use of coupled map lattices to represent, at a coarse-grained level, behav-
ior of intrinsically non-linear dynamical systems coupled in space is at least two
decades old[1]. Coupled map lattices provide relatively simple models whenever
it can be assumed that the dynamics can be naturally decoupled into a dominant
local dynamics representing behaviour at a single point in space (or small coarse-
grained region) and a spatial coupling term which connects this local dynamics
weakly across spatial locations. The coupling term idealizes gradient terms in the
underlying continuum equation of motion. Coupled map lattices are well-suited for
computer simulations, since they are naturally discrete in space and time. (Experi-
mental data are, in fact, close to the CML situation, since any real-life measurement
requires discrete sampling of the underlying time evolution and every experiment
has some minimum threshold for spatial discrimination, providing a lattice scale.)
Coupled map lattices have been used with success by several authors in the study
of phase-ordering problems as well as in a host of other applications[101, 1].

We begin by constructing a local map for nematics under shear, obtained by
discretizing a set of coupled ordinary differential equations (ODE's) describing
the continuous time, spatially local version of this dynamics. These *local* equations
have been shown to exhibit periodic and regular regimes as well as chaotic regimes.
We benchmark this map through a detailed comparison to the results from the
study of the ODE system, showing that the qualitative and quantitative aspects
of the phase diagram in this single site limit are rendered accurately. We then
generalize this to the spatially coupled case by connecting nearest neighbour maps
in a specified manner. The shear enters at the level of the local map, where
it is specified in terms of a single parameter. We take the point of view that
the complexity of the spatio-temporal behavior in the physical problem can be
captured by the most elementary version of spatial coupling, which, for simplicity
and following virtually all work on coupled map lattices, we take to be diffusive[1,
135].

This *local* map is shown, in agreement with previous work, to exhibit a large

number of complex phases, including uniform (flow aligning in the nematic), tumbling, kayaking and chaotic phases, in addition to phases which combine one or the other of these attributes[112, 113]. While the nematic responds to the fluid through flow alignment as well as reactive and dissipative terms in the equation of motion, we make the approximation of ignoring the back-reaction of changes in nematic order on the fluid. Thus, our approach omits the hydrodynamic interaction, since we assume that the flow always remains passive. This is a major assumption. However, it does have the virtue that a variety of spatio-temporal phenomena with relevance to both the experiments as well as to earlier modeling exercises can be demonstrated to exist in this simple system and are amenable to analysis.

Our second approximation is that we study, for the most part, simple diffusive couplings between sites, ignoring the advective terms. Consistent with this, we use simple periodic boundary conditions on the local field. (We would otherwise have had to implement a more complex Lees-Edwards boundary condition on the fields and ensure an appropriate anchoring condition at the boundaries[88].) Thus, in our model, the shear enters the *local* dynamics but its effects are ignored at larger scales. We also thus neglect the several non-linear, anisotropic spatial coupling terms which are included in continuum formulations of nematodynamics which go beyond the simplest one-Frank-constant approximation. We pursue this line of investigation because our interest is specifically in the effects of including spatial couplings into a model which provides an accurate description of the temporal behavior of sheared nematics assuming spatial behavior to be uniform. We believe – and in some cases have tested this assumption – that incorporating the simplest form of spatial coupling should be sufficient for us to be able to explore the full spatio-temporal complexity of the sheared nematic problem.

The outline of this chapter is the following: Section II outlines our numerical methods for the construction of the local map. We begin by providing the local equation of motion for a passively sheared fluid of nematogens, following the work of Refs. [112, 113]. To enforce symmetry and tracelessness, it is customary to project these (tensor) equations onto a suitable tensor basis. We then construct, through a simple Euler discretization, a map within this basis, showing that it can be used to obtain all the states obtained by ODE-based methods for this problem. The following section, Section III, describes the construction of the coupled map lattice, illustrating how the local maps constructed in Section II can be coupled

in space, in both one and two dimensions. Section IV describes our results in
the one-dimensional case, examining the effects of spatial coupling in both regular
and complex regions of the local map. Section V describes our results for the
two-dimensional case, studying, as in the one-dimensional case, the behaviour in
both regular and complex regimes of the local phase diagram. Section VI contains
a discussion of our results as they relate to a quantification of spatio-temporal
complexity in our model, while Section VII contains the conclusions of this study.

6.2   A Local Map for Nematodynamics

We begin with the continuum equations of motion for a nematic in a specified flow
field. These equations use the tensor representation of the order parameter in a
nematic. In thermal equilibrium, such order parameter configurations are weighted
by a Landau-Ginzburg-de Gennes free energy. In a specific Cartesian tensor basis,
these equations, in the approximation that spatial fluctuations in nematic order are
absent, can be cast in terms of equations of motion for five expansion coefficients,
corresponding to the five independent parameters characterizing a real symmet-
ric traceless tensor. These equations of motion, which are ordinary differential
equations (ODE's), are recast as a map, as shown below.

We have explored alternative constructions for such a local map in Ref. [67],
where we studied a quaternion representation of the local orientational degrees of
freedom. We tried several methods for coupling such "quaternion maps" in space,
to mimic the spatial coupling term in the CML formulation. However, because
the local frame can vary from site to site, there seems to be no straight-forward
way to generate such terms without involving considerable analytic complexity.
Thus, we work with a simpler local map, derived from the ODE's in a Cartesian
representation, in this chapter. Incorporating spatial coupling appear to be easiest
in this version of the model.

6.2.1   Equation of Motion for Nematics

The derivation of the nonlinear relaxation equations for the symmetric, traceless
second rank tensor $\mathbf{Q}$ characterizing local order in a sheared nematic is available
in earlier work [61, 42, 43, 62, 102, 82, 97, 107, 123, 58, 126]. The order parameter

is often conveniently expressed as

$$Q_{\alpha\beta} = \frac{3s_1}{2}\left(n_\alpha n_\beta - \frac{1}{3}\delta_{\alpha\beta}\right) + \frac{s_2}{2}\left(l_\alpha l_\beta - m_\alpha m_\beta\right), \tag{6.1}$$

where the director $\mathbf{n}$ is defined as the normalized eigenvector corresponding to the largest eigenvalue of $\mathbf{Q}$, the subdirector $\mathbf{l}$ is associated with the sub-leading eigenvalue, and their mutual normal $\mathbf{m}$ is obtained from $\mathbf{n} \times \mathbf{l}$. The quantities s_1 and s_2 represent the strength of uniaxial and biaxial ordering: $|s_1| \neq 0$, $s_2 = 0$ is the uniaxial nematic whereas $s_1, s_2 \neq 0$ with $s_2 < 3s_1$ defines the biaxial case[39].

Defining $\widehat{\mathbf{b}} := \frac{1}{2}(\mathbf{b} + \mathbf{b}^T) - \frac{1}{3}(tr\mathbf{b})\delta$ to be the symmetric-traceless part of the second-rank tensor $\mathbf{b}$, the equation of motion for $\mathbf{Q}$ in a velocity field is [61, 113]:

$$\frac{d\mathbf{Q}}{dt} - 2\widehat{\mathbf{\Omega} \cdot \mathbf{Q}} - 2\sigma'\widehat{\mathbf{\Gamma} \cdot \mathbf{Q}} + \tau_Q^{-1}\mathbf{\Phi} = -\sqrt{2}\frac{\tau_{ap}}{\tau_a}\mathbf{\Gamma}, \tag{6.2}$$

where the tensor $\mathbf{\Omega} = \frac{1}{2}((\nabla\mathbf{v})^T - \nabla\mathbf{v})$, $\mathbf{\Gamma} = \frac{1}{2}((\nabla\mathbf{v})^T + \nabla\mathbf{v})$ and $\nabla\mathbf{v}$ is the velocity gradient tensor, with $\mathbf{v} = \dot{\gamma}y\mathbf{e^x}$, where $\mathbf{e^x}$ is a unit vector in the $x-$ direction. The velocity is along the x direction, the velocity gradient is along the y direction, while z is the vorticity direction. The quantities $\tau_a > 0$ and τ_{ap} are phenomenological relaxation times, σ' describes the change of alignment caused by $\mathbf{\Gamma}$ and $\mathbf{\Phi} = \partial\phi/\partial\mathbf{Q}$, with the free energy $\phi(\mathbf{Q})$ given by

$$\phi(\mathbf{Q}) = \frac{1}{2}A\mathbf{Q} : \mathbf{Q} - \frac{1}{3}\sqrt{6}B(\mathbf{Q} \cdot \mathbf{Q}) : \mathbf{Q} + \frac{1}{4}C(\mathbf{Q} : \mathbf{Q})^2. \tag{6.3}$$

If the spatial variation is also taken into account, $\nabla^2\mathbf{Q}$ and $\nabla\nabla\cdot\mathbf{Q}$, as well as higher order terms, should also be included in the above expression. Such gradient terms are weighted by coefficients L_1, L_2 and L_3, yielding the three Frank elastic constants of the nematic state. The notation $Q : Q$ represents $Q_{ij}Q_{ji}$, with repeated indices summed over. Here $A = A_0(1 - T^*/T)$, and B and C are constrained by the conditions $A_0 > 0$, $B > 0, C > 0$ and $B^2 > \frac{9}{2}A_0C$.

The symmetric traceless alignment tensor $\mathbf{Q}$ has five independent components. Assuming spatial uniformity, so that gradients of the $\mathbf{Q}$ tensor can be dropped, a system of 5 coupled ordinary differential equations (ODEs) for the 5 independent components of $\mathbf{Q}$ can be obtained with the choice of a suitable tensor basis. Choos-

ing the standard orthonormalized Cartesian tensor basis leads to the expansion

$$\mathbf{Q} = \sum_{k=0}^{4} a_k \mathbf{T^k}, \tag{6.4}$$

with

$$\mathbf{T^0} = \sqrt{3/2}\,\widehat{\mathbf{e}^z\mathbf{e}^z}, \quad \mathbf{T^1} = \sqrt{1/2}(\mathbf{e}^x\mathbf{e}^x - \mathbf{e^y}\mathbf{e^y}),$$

$$\mathbf{T^2} = \sqrt{2}\,\widehat{\mathbf{e}^x\mathbf{e}^y}, \quad \mathbf{T^3} = \sqrt{2}\,\widehat{\mathbf{e}^x\mathbf{e}^z}, \quad \mathbf{T^4} = \sqrt{2}\,\widehat{\mathbf{e}^y\mathbf{e}^z}. \tag{6.5}$$

6.2.2   Dynamics of Sheared Nematics from a Local Map

We work in the tensor basis described above, representing the equations of motion of Eq. 6.2 in terms of the coupled equations of motion for the five coefficients $a_0 \ldots a_4$. The problem of representing the time updates in terms of a local map is most easily approached by considering the lowest order Euler discretization of the underlying differential equations. (There are alternative methods of constructing maps from local dynamics governed by ODE's, including stroboscopic methods and methods which use Poincare sections; however, the choice we have made is the simplest given the variety and complexity of the dynamical states we would like to describe.)

Scaling parameters as in Ref. [112, 113], and making the same choice of numerical values as in Ref. [26, 37], we obtain the following map

$$f_0(a_0{}^t) \;\; = a_0{}^t + \;\; \Delta\left(-(2a^2 - 3a_0)a_0 - 3(a_1^2 + a_2^2) + \frac{3}{2}(a_3^2 + a_4^2)\right)^t$$

$$f_1(a_1{}^t) \;\; = a_1{}^t + \;\; \Delta\left(-(2a^2 + 6a_0)a_1 + \dot{\gamma}a_2 + \frac{3}{2}\sqrt{3}(a_3^2 - a_4^2)\right)^t$$

$$f_2(a_2{}^t) \;\; = a_2{}^t + \;\; \Delta\left(-(2a^2 + 6a_0)a_2 - \dot{\gamma}a_1 + 3\sqrt{3}a_3a_4 + \frac{\sqrt{3}}{2}\lambda_k\dot{\gamma}\right)^t$$

$$f_3(a_3{}^t) \;\; = a_3{}^t + \;\; \Delta\left(-(2a^2 - 3a_0)a_3 + \frac{1}{2}\dot{\gamma}a_4 + 3\sqrt{3}(a_1a_3 + a_2a_4)\right)^t$$

$$f_4(a_4{}^t) \;\; = a_4^t + \;\; \Delta\left(-(2a^2 - 3a_0)a_4 - \frac{1}{2}\dot{\gamma}a_3 + 3\sqrt{3}(a_2a_3 - a_1a_4)\right)^t. \tag{6.6}$$

Here t indicates discrete time steps, and $\{.\}^t$ denotes the value of the quantity $\{.\}$ at time step t. All the functions f denote the locally updated value of their argument at a time step $(t+1)$. For the purely local map, $f_i(a_i^t) \equiv a_i^{t+1}$; however, for the coupled map, the value of $f_i(a_i^t)$ is computed as an intermediate step, prior to the diffusive step which yields the final quantity a_i^{t+1}. The quantity $a^2 = a_0^2 + a_1^2 + a_2^2 + a_3^2 + a_4^2$.

We choose the time step to be small, ensuring the stability of the Euler discretization scheme; specifically, $\Delta = 0.01$ for all our calculations. Our approach thus contrasts to approaches in which the discrete space-time update rules are chosen such that they represent a regime in which standard Euler discretization of the governing equations breaks down, yielding a complex bifurcation structure which can be argued to resemble one or the other physical behaviour. Here, our approach is to render the local physics, in particular the topology of the complex phase diagram with its many non-trivial phases, as accurately as possible. (Our essential simplifications enter our representation of the non-local terms, incorporated so as to represent the physics of the spatially coupled case.) We have checked that changing Δ by upto an order of magnitude does not affect our results. Thus, the qualitative dynamics, which is complex in state space and parameter space, is completely robust in the range of Δ chosen for this study. Our choice of parameters implies that the system in the absence of shear is at the limit of metastability of the isotropic phase. Our choice of the value for Δ captures all the features of the full local phase diagram obtained in Refs. [112, 113].

The order parameter part of the stress is proportional to contributions from the Landau-de Gennes free energy as well as from the gradient terms, which we represent through the spatial coupling term in the coupled map lattice. This is obtained as described in the following sections.

6.2.3   Phase Behaviour of the Local Map

Examining the dynamical steady states of this map at a large number of points in the space spanned by $(\dot{\gamma}, \lambda_k)$ yields a complex phase diagram admitting many states – aligned, tumbling, wagging, kayak-wagging, kayak-tumbling and chaotic – as functions of the shear rate $\dot{\gamma}$ and a phenomenological relaxation time λ_k which is a parameter in the equations of motion[112, 113, 56]. Fig. (6.1) exhibits the

dynamical states found in the map for the uncoupled case, in terms of a phase
diagram in the quantities λ_k and $\dot{\gamma}$. Such a phase diagram bears considerable sim-
ilarities to phase diagrams obtained by other authors in the PDE representation;
see, for example, Fig. 7 of Ref. [113].
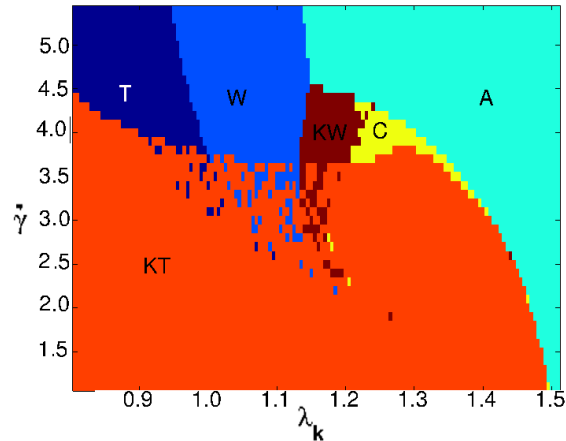
Figure 6.1: Phase diagram for dynamical behaviour in the local map defined
through Eqns.6.6, with the parameter λ_k plotted on the x axis and $\dot{\gamma}$ on the y
axis. Here T denotes the tumbling state, W the wagging state, KT the kayak-
tumbling, KW the kayak-wagging state, A the aligned state and C the state in
which complex dynamics is seen. These states are discussed further in the text.

The states in this phase diagram are labeled as follows: The first is the state
labeled A, which is the **Aligned state**, where all dynamics ceases, and the director
is aligned at an angle to the flow. In the standard Couette geometry, the velocity
field and the velocity gradient form a plane, called the vorticity plane. In our case,
this is the $x - y$ plane. If the director lies in the vorticity plane and rotates about
an axis (the $z-$axis) perpendicular to this plane, the dynamical state is called
a **Tumbling state**. The tumbling state is denoted by T in the phase diagram
of Fig. (6.1). If the director, while lying in the plane, executes oscillations, the
dynamical state is called a **Wagging state**. The wagging state is represented in
the local phase diagram by the symbol W.

If the director rotates and oscillates, moving out of the vorticity plane, the
dynamical states are called **Kayak-Tumbling** and **Kayak-Wagging** respectively.
They are represented as KT and KW in the local phase diagram. If the dynamics
is a mixture of complex intermittent behaviour and coexisting attractors, the state

is called **Complex** and is represented by C in the phase diagram. Clearly the
interesting region in the phase diagram lies in and near the region labeled C.

Fig. 6.1 is obtained in the following way. The phase-space of the $\dot{\gamma}$ and λ_k
variables is gridded and an initial random initial condition chosen at each point.
After the passage of an initial transient state, the system goes to dynamical at-
tractors, ranging from simple spatiotemporal fixed points to complex intermittent
behaviour. These dynamical attractors are identified with one of the states de-
scribed above, i.e. A, K, T, KW, KT or C. In some regimes, one sees a coexistence
of states *i.e.* KT and T and KW and W *i.e.* different initial conditions can give
rise to different asymptotic behaviour in the long time limit.

Near the phase boundary of KW, one obtains isolated points which show com-
plex behavior for generic initial conditions. However, choosing a point in the close
vicinity of such points generically produces KW states. Thus, such C points are
isolated. However, deep into the KW phase any such complex behavior is found to
be purely an initial transient, with the state settling down to KW in the long-time
limit.

6.3   Coupled Maps for Nematodynamics

Our spatially coupled model is built up from the local maps given in Eq. 6.6. These
maps are placed on the sites of a regular lattice in one and two dimensions and
can be coupled via several different coupling schemes, as described below. The
generalization to arbitrary dimensions as well as different coupling schemes is a
straightforward one.

For a one dimensional lattice, with sites indexed by the label i, the five variables
$(a_0(i) \ldots a_4(i))$ on each lattice site evolve in discrete time t as:

$$\phi_i = \phi'_i + \frac{1}{3}\epsilon \left(\phi^t_{i+1} + \phi^t_{i-1} - 2\phi^t_i\right), \qquad (6.7)$$

where $\phi \in (a_0^{t+1},\, a_1^{t+1},\, a_2^{t+1},\, a_3^{t+1},\, a_4^{t+1})$ and $\phi' \in (f_0(a_0^t), f_1(a_1^t), f_2(a_2^t), f_3(a_3^t), f_4(a_4^t))$ $.Here \epsilon$
is a coupling constant which is chosen to take values between 0 and 3/2.

For the two dimensional case we consider a square lattice with site index (i,j)
and with the set of five variables $(a_0(i,j),\ a_1(i,j),\ a_2(i,j),\ a_3(i,j),\ a_4(i,j))$ on

each lattice point at time-step t evolving in time as :

$$
\begin{aligned}
\phi_{i,j} \; = \; \phi'_{i,j} \quad & +\frac{1}{6}\epsilon \left(\phi^t_{i+1,j} + \phi^t_{i-1,j} + \phi^t_{i,j+1} + \phi^t_{i,j-1} \right) \\
& +\frac{1}{12}\epsilon \left(\phi^t_{i+1,j+1} + \phi^t_{i-1,j-1} + \phi^t_{i-1,j+1} + \phi^t_{i+1,j-1} \right) - \epsilon \phi^t_{i,j}, \quad (6.8)
\end{aligned}
$$

where $\phi \in (a_0^{t+1},\, a_1^{t+1},\, a_2^{t+1},\, a_3^{t+1},\, a_4^{t+1})$ and $\phi' \in (f_0(a_0^t), f_1(a_1^t), f_2(a_2^t), f_3(a_3^t), f_4(a_4^t))$, and ϵ is a coupling constant having value between 0 and 1. The choice of the numerical coefficients 1/6 and 1/12 in the coefficients of the nearest and next-nearest neighbour terms are standard choices in the CML literature. They represent choices of lattice discretization which are as close as possible to the continuum limit.

The local value of the shear stress $(\sigma_{xy})_{i,j}$ at the (two-dimensional) site (i,j) is obtained from the following definition.Strictly speaking, the quantity defined is *proportional* to the stress. In particular, it is multiplied by an overall multiplicative factor involving λ_k; see Eqn. A.1 of Ref. [112]:

$$
\begin{aligned}
(\sigma_{xy})_{i,j} \; = \; (\sigma'_{xy})_{i,j} \quad & +\frac{\sqrt{2}}{6}\epsilon \left(\phi_{i+1,j} + \phi_{i-1,j} + \phi_{i,j+1} + \phi_{i,j-1} \right) \\
& +\frac{\sqrt{2}}{12}\epsilon \left(\phi_{i+1,j+1} + \phi_{i-1,j-1} + \phi_{i-1,j+1} + \phi_{i+1,j-1} \right) - \sqrt{2}\epsilon\phi_{i,j}, \quad (6.9)
\end{aligned}
$$

where $(\sigma'_{xy})_{i,j}$ is given by

$$
(\sigma'_{xy})_{i,j} = (2\sqrt{2}a_2 a^2 - 6\sqrt{6}(a_3 a_4/2 - (a_2 a_0/\sqrt{3})))_{i,j}, \qquad (6.10)
$$

and $\phi = a_2$.

The definition for the one-dimensional case follows from:

$$
(\sigma_{xy})_i \; = \; (\sigma'_{xy})_i \quad +\frac{\sqrt{2}}{3}\epsilon \left(\phi_{i+1} + \phi_{i-1} - 2\phi_i \right), \qquad (6.11)
$$

where $(\sigma'_{xy})_i$ is given by

$$
(\sigma'_{xy})_i = (2\sqrt{2}a_2 a^2 - 6\sqrt{6}(a_3 a_4/2 - (a_2 a_0/\sqrt{3})))_i, \qquad (6.12)
$$

and $\phi = a_2$.

We have also experimented with other choices of the update rule. While the
update rule of Eq. 6.7 can be termed as the *pre-update* rule, in which the terms
on the right hand side are calculated using the variables at time t, one could
alternatively use the *post-update* rule, in which the diffusive terms on the right
hand-side are calculated using the variables at time $t + 1$. We have checked that
varying this choice of update rule does not affect our results. In the equation
for the two-dimensional update, (Eq. 6.8), we have checked that dropping the
next-nearest neighbour term also does not affect our results significantly. Thus, a
variety of possible update schemes appear to yield consistent results for the spatio-
temporal behaviour of our coupled map lattice, underlining the generic nature of
our results.

Finally, we stress one important feature of our approach. We work with local
maps which are obtained by Euler discretization of the governing equations, in a
limit in which such discretization is stable. Thus, we are assured that the *local*
physics is rendered accurately, an important consideration given the complexity
of the local phase diagram. However, our crucial approximations are made at the
level of the spatial coupling terms where we *ignore* the effects of the shear at scales
beyond that of the local map, replacing the required convective term by a simple
diffusive term. In addition, while the derivative terms involving L_2 and higher
order terms conventionally retained in the Landau-Ginzburg-de Gennes expansion
are highly anisotropic and non-linear, we neglect all such terms, proposing that
both the regular and spatio-temporally complex behaviour of interest to us can be
obtained by incorporating the simplest form of (diffusive) spatial coupling in our
coupled map lattice.

6.4   The One-dimensional Coupled Map Lattice

In this section, we describe our results for the one-dimensional case, concentrating
on the effects of the inter-site coupling, both within and outside the regime labelled
C in the phase diagram.
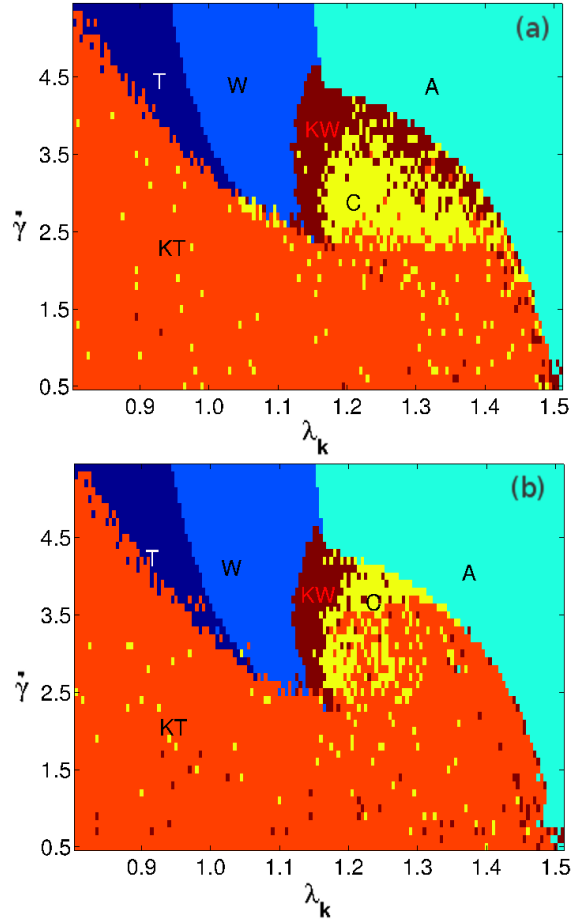
Figure 6.2: Phase diagram summarizing the local dynamical behaviour of the spatially coupled one-dimensional system, with λ_k plotted on the x axis and $\dot{\gamma}$ on the y axis. As before, T denotes the tumbling state, W the wagging state, KT the kayak-tumbling, KW the kayak-wagging state, A the aligned state and C the state of complex dynamics. The spatial coupling constant $\epsilon = 0.1$ (a) and 0.5 (b), for a ring of 200 lattice points. The location of the states in the phase diagram is largely similar to that of Fig. 6.1 with the exception that, at isolated points, mainly within the KT phase, one sees complex behaviour. The regime in the phase diagram occupied by the C phase shrinks as the coupling constant ϵ is increased.

6.4.1 Local dynamics

Fig. (6.2) shows the dynamical phases exhibited by a generic site randomly chosen
from the one dimensional ring. The sites are coupled according to the scheme given
in Eq. 6.8, with coupling constant $\epsilon = 0.1$ (a) and $\epsilon = 0.5$ (b).

It is evident from comparisons with Fig. (6.1) that the local dynamics of a
generic site in the coupled system is similar to the uncoupled case. This indicates
that spatial coupling does not alter the nature of the local dynamics qualitatively.
The most significant influence of spatial coupling occurs near the C region, which
appear to be somewhat broadened with spatial coupling, while the coexistence
regimes are reduced in size. In addition, the fairly uniform KT state is now "stud-
ded" with points displaying complex behaviour. This indicates coexistence of com-
plex and KT behaviour, with certain initial states leading to complex dynamics,
while others lead to a uniform KT state. (It is difficult to determine whether the
complex behaviour we see is a very long transient or true asymptotic behaviour.)
The tumbling T and wagging W regions, however, are very stable.

Local behaviour of regular regions

Figs. (6.3)-(6.4) show the value of the scalar order parameter s_1, the biaxiality
parameter s_2 and the z component of the director **n**. Fig. (6.3) is obtained using
parameter values appropriate to the T and W regions of the local phase diagram,
with a coupling constant $\epsilon = 0.1$. This displays completely regular behaviour,
with these quantities varying periodically keeping the director in the vorticity
plane. Fig. (6.4) is obtained using parameter values appropriate to the KT and
KW regions of the local phase diagram and indicate that the director can now
fluctuate out of plane whereas all quantities vary smoothly and periodically. The
local time period $T(\dot{\gamma})$ with which these quantities oscillate is found to be inversely
proportional to shear rate, with $T \sim \frac{1}{\dot{\gamma}}$, as $\dot{\gamma}$ is varied across the T and KT regions
of the phase diagram.

Local Dynamics in the Complex Region

The local behaviour in the complex region, denoted by C in the local phase dia-
gram, is exhibited in Fig. (6.5), which shows s_1 and s_2 and n_z. The results suggest
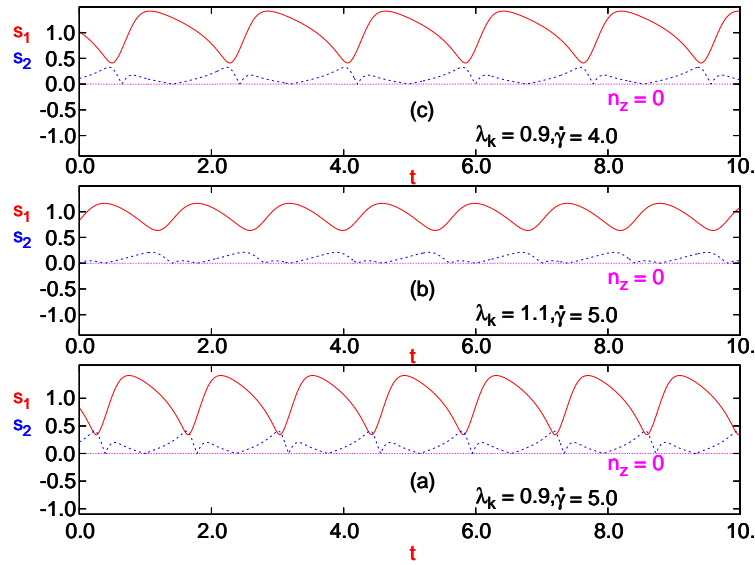
Figure 6.3: Local dynamics in a ring of 200 lattice points, with coupling $\epsilon = 0.1$, showing the temporal evolution of s_1, s_2 and n_z. These are displayed for (a) s_1, s_2 and n_z with (a) $\lambda_k = 0.9$ and $\dot{\gamma} = 5.0$ (b) $\lambda_k = 1.1$ and $\dot{\gamma} = 5.0$, and (c) $\lambda_k = 0.9$ and $\dot{\gamma} = 4.0$. These states are all drawn from the T and W parts of the local phase diagram. Note that $n_z = 0$ in all these states whereas s_1 and s_2 are periodic functions of time.

that the sites display *intermittent* behaviour. These results are obtained for parameter values at the boundary of the complex region and the kayak-wagging region, with paramters $\dot{\gamma} = 4.0$ and $\lambda_k = 1.2$. In part (a), the coupling constant $\epsilon = 0.5$, in part (b) $\epsilon = 0.15$ and in part (c) $\epsilon = 0.1$. All of these show qualitatively similar temporally intermittent behaviour. The fourier transform of the time series of stress calculated at a generic site and plotted on a doubly logarithmic scale is shown in Fig. (6.6). The spectrum in (c) of Fig. (6.6) fits the relation $P(f) \sim 1/f^2$.

6.4.2 Spatio-temporal coherence and dynamics

In order to quantify the degree of spatial coherence, we calculate the following quantity for the one-dimensional lattice:

$$\overline{d} = \sqrt{\frac{1}{NT} \sum_{t=1}^{T} \sum_{i=1}^{N} (a_0^t(i) - \overline{a}^t)^2}, \qquad (6.13)$$
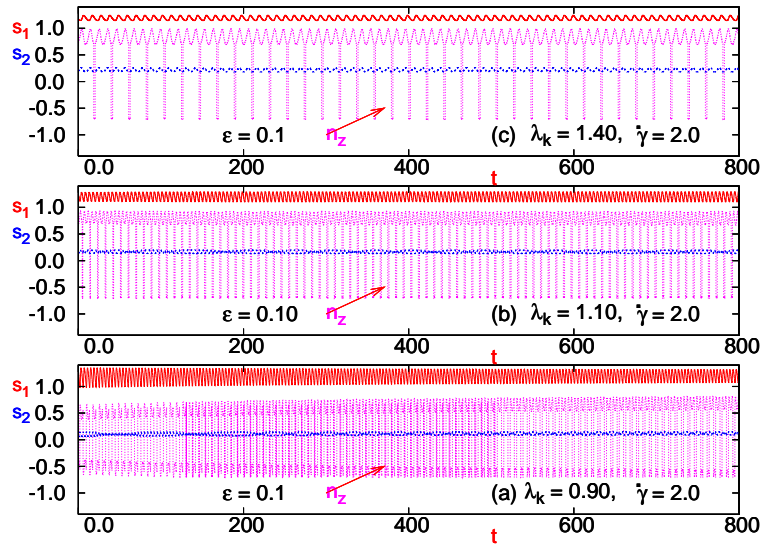
Figure 6.4: Local dynamics in a ring of 200 lattice points, with coupling $\epsilon = 0.1$, showing the temporal evolution of s_1, s_2 and n_z. These are displayed for for (a) $\lambda_k = 0.9$ and $\dot{\gamma} = 2.0$ (b) $\lambda_k = 1.1$ and $\dot{\gamma} = 2.0$, and (c) $\lambda_k = 1.4$ and $\dot{\gamma} = 2.0$. These points are drawn from the KT and KW part of the local phase diagram and represent states in which the director exhibits out-of-plane fluctuations *i.e.* $n_z \neq 0$. However, s_1 and s_2 continue to exhibit regular, periodic oscillations.

where

$$\overline{a^t} = \frac{1}{N} \sum_{i=1}^{N} a_0^t(i). \tag{6.14}$$

We have calculate such a spatial coherence parameter for one specific component of the vector $(a_0, \ldots, a_4)$; however, qualitatively similar results are obtained for other components as well as for the full local stress, in the C region. When $\overline{d}$ tends to zero the degree of synchronization of the local variables is very high. On the other hand large $\overline{d}$ indicates low spatial synchronization, arising from a wide distribution of values of the local variables in the lattice. This quantity thus serves as a global order parameter characterizing the smoothness of the spatial patterns exhibited by the evolution of the map.

Fig. (6.7) shows the time average of the deviation $< \overline{d} >$ of a_0 from the average value a_0. To compute this, we first calculate the instantaneous deviation $\overline{d}$ via Eqs. (6.14) and (6.13), and then find the long-time average of this quantity. The spatial profile of the regular region with low $< \overline{d} >$ is characterised either by

117
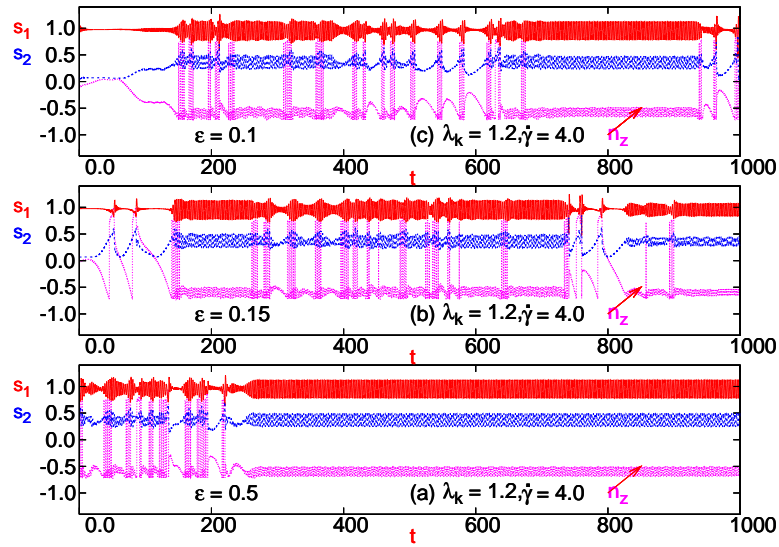
Figure 6.5: Local dynamics of a ring of 200 lattice points, with $\lambda_k = 1.2$ and $\dot\gamma = 4.0$, showing the time evolution of s_1, s_2 and n_z. These are shown for (a) $\epsilon = 0.5$ (b) $\epsilon = 0.15$ and (c) $\epsilon = 0.1$, illustrating behaviour in the complex or C regime. Note that regular time-periodic behaviour is favoured at large values of the spatial coupling constant ϵ, following an initial transient.

spatiotemporal fixed behaviour with all sites aligned, or spatial uniformity and temporal periodicity. There are also cases in the regular region where the sites, though not completely synchronized in space, are nevertheless phase synchronized.

Spatio-temporal dynamics in the regular region

Fig. (6.8) displays the space-time plot for $\dot\gamma = 4$, $\lambda_k = 1.1$ and coupling constant $\epsilon = 0.1$ (a) and 0.5 (b). The x-axis displays the lattice index and time is shown on y-axis, increasing from top to bottom. The profile is not spatially uniform and periodic in time for very weak coupling. As the coupling is increased, the system acquires spatial coherence and temporal periodicity.

Spatio-temporal dynamics in the complex region

The spatiotemporal behaviour of a representative case in the C or complex region is displayed in Fig. (6.9), where $\dot\gamma = 4$, $\lambda_k = 1.17$ and coupling constant $\epsilon = 0.1$ (a) and 0.5 (b). It is evident that the space-time profile splits into bands, i.e. clusters of

118
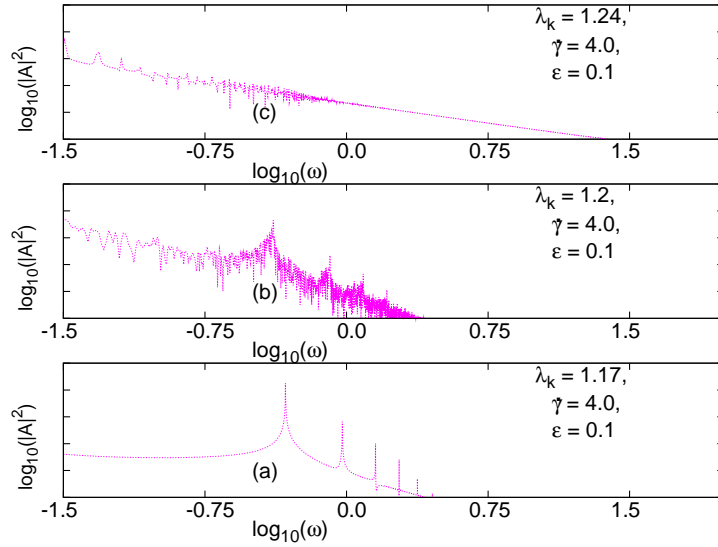
Figure 6.6: Log-Log plot of the Fourier transform vs. frequency, for (a) $\lambda_k = 1.17$,
(b) $\lambda_k = 1.20$ and (c) $\lambda_k = 1.24$. Here $\epsilon = 0.1$ and $\dot{\gamma} = 4.0$. The lattice is a ring
of 200 sites. Note that for $\lambda_k = 1.17$ (the wagging region), the regular oscillations
show up as a delta function in the fourier transform. In the C or complex region,
a smooth distribution of frequencies is seen, with a $1/f^2$ falloff.

synchronized sites, where the local dynamics is either fixed (blue) or time-periodic
(stripes). As we increase λ_k (with $\dot{\gamma} = 4$) in Figs. (6.9 - 6.11) the length scale of
the spatio-temporally intermittent pattern increases, finally yielding to the aligned
region. This progression from frozen localized kinks/domains of fixed points in
the spatial background of time-periodic behaviour, to infective bursts bearing the
signature of spatiotemporal intermittency, is seen in many systems [36, 70, 71],
and often arises from a competition of fixed point patterns and time-periodic and
quasi-periodic patterns.

6.5 The Two-dimensional Coupled Map Lattice

In this section, we investigate the phenomenology of two-dimensional systems ex-
hibiting nematic rheochaos, arguing that it is important to gain intuition about
the differences and similarities in the spatiotemporal dynamics arising in higher
dimensional models vis-a-vis one-dimensional models. While one-dimensional sys-
tems have been investigated fairly extensively, very little work describes the be-
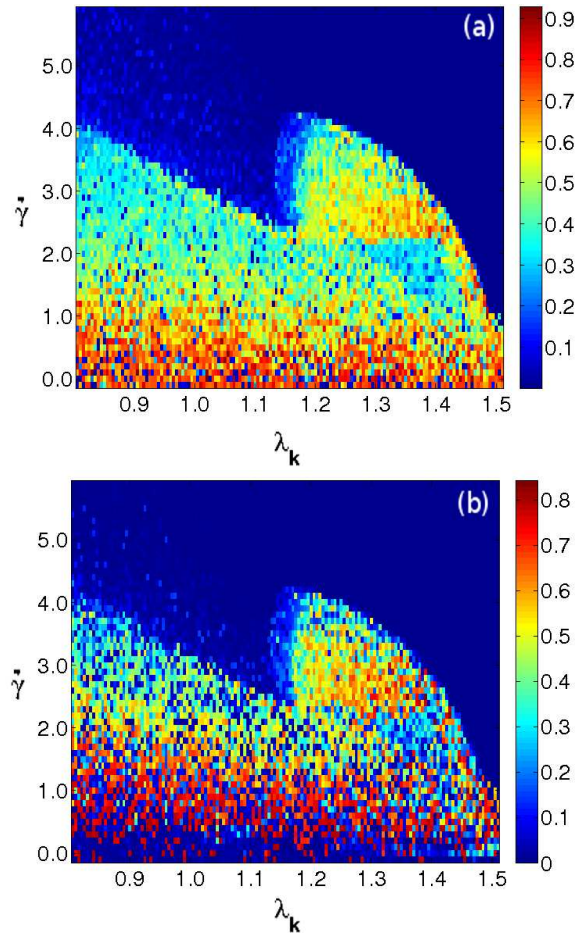
Figure 6.7: Average deviation from the mean value for $\epsilon = 0.1$ (a) and $\epsilon = 0.5$ (b), with λ_k on the x-axis and $\dot{\gamma}$ on the y axis. Note that large fluctuations (roughness) are seen in the KW and C regions. These data are for the 1-d system wiith the number of sites $N = 200$ and parameters as indicated on the figure.
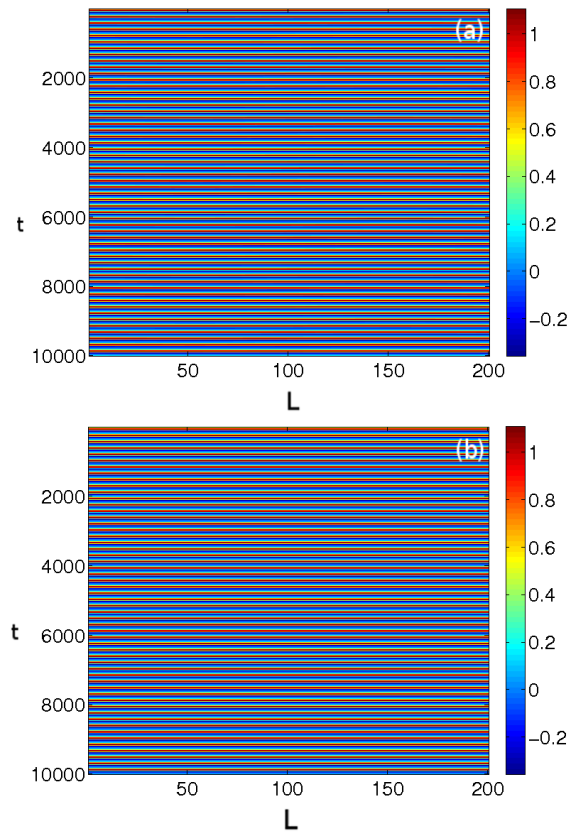
Figure 6.8: Density plot of order parameter part of shear stress. Here $\lambda_k = 1.1$, $\dot{\gamma}$ =4.0 and $\epsilon = 0.1$ (a) and 0.5 (b). Time steps (running from top to bottom) are on the y-axis, and the lattice site index $(i = 1, 200)$ is on the x-axis. These figures represent space-uniform and time-periodic states, obtained using parameter values corresponding to the T region of the phase diagram.
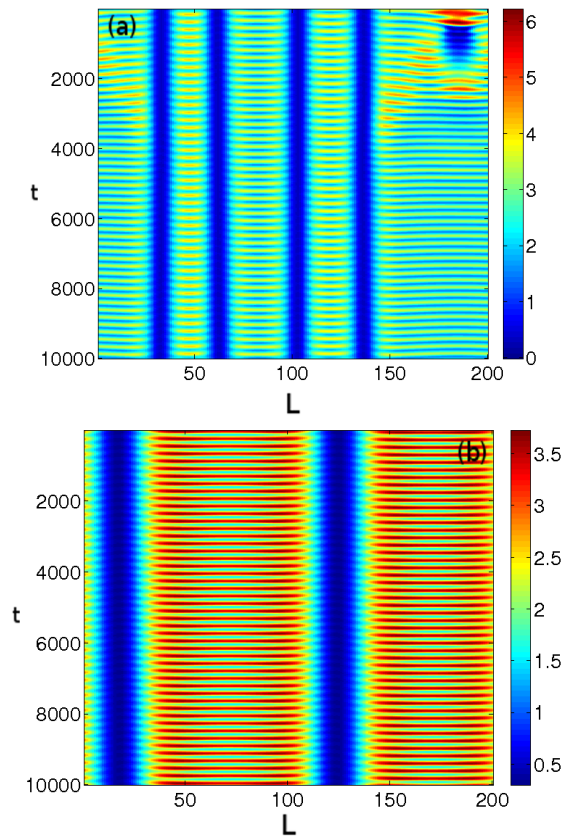
Figure 6.9: Density plot of order parameter part of shear stress. Here $\lambda_k = 1.17$, $\dot{\gamma}$ =4.0 and $\epsilon = 0.1$ (a) and 0.5 (b). Time steps (running from top to bottom) are on the y-axis, and the lattice site index ($i = 1, 200$) is on the x-axis. These figures represent space non-uniform and time-periodic states, obtained using parameter values corresponding to the KW region of the phase diagram
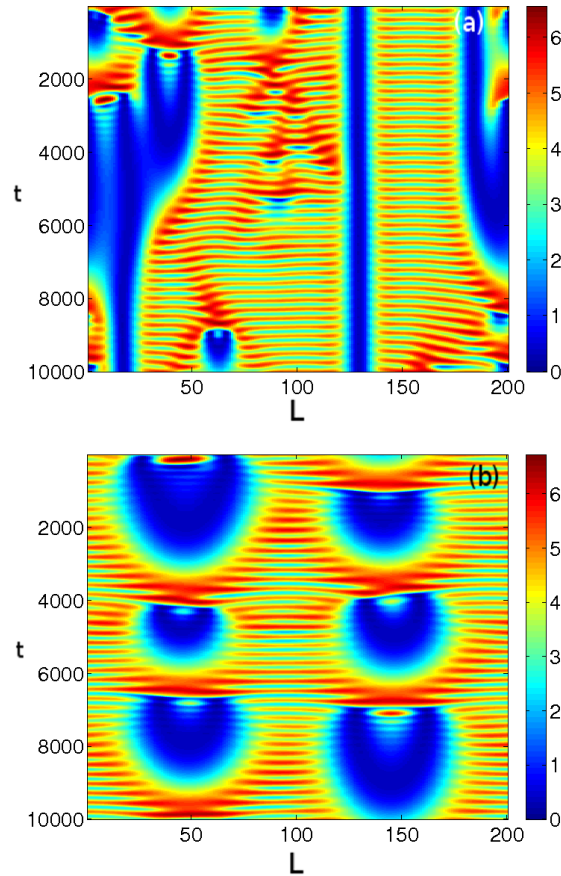
Figure 6.10: Density plot of order parameter part of shear stress. Here $\lambda_k = 1.20$, $\dot{\gamma} =$4.0 and $\epsilon = 0.1$ (a) and 0.5 (b). Time steps (running from top to bottom) are on the y-axis, and the lattice site index ($i = 1, 200$) is on the x-axis. These figures illustrate how time-periodic regions are interspersed with domains of fixed point behaviour, reminiscent of spatiotemporal intermittency. The parameter values corresponding to the C region of the phase diagram, in a regime where the chaos is weak.
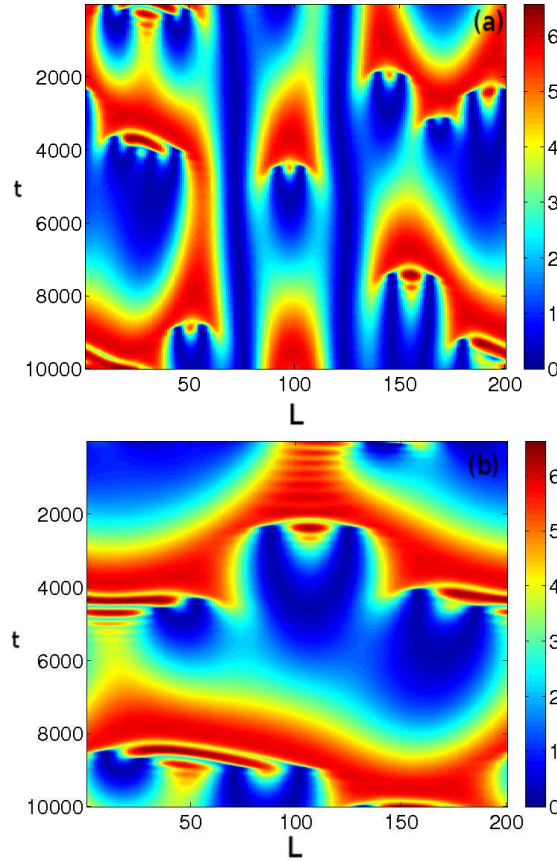
Figure 6.11: Density plot of order parameter part of shear stress. Here $\lambda_k = 1.24$, $\dot{\gamma} = 4.0$ and $\epsilon = 0.1$ (a) and 0.5 (b). Time steps (running from top to bottom) are on the y-axis, and the lattice site index ($i = 1, 200$) is on the x-axis. These figures illustrate non-uniform, time-varying states characteristic of spatio-temporally chaotic behaviour. The parameter values correspond to the C region of the phase diagram, in a regime where the chaos is strong. Note that larger values of ϵ lead to larger and more uniform spatial structures.
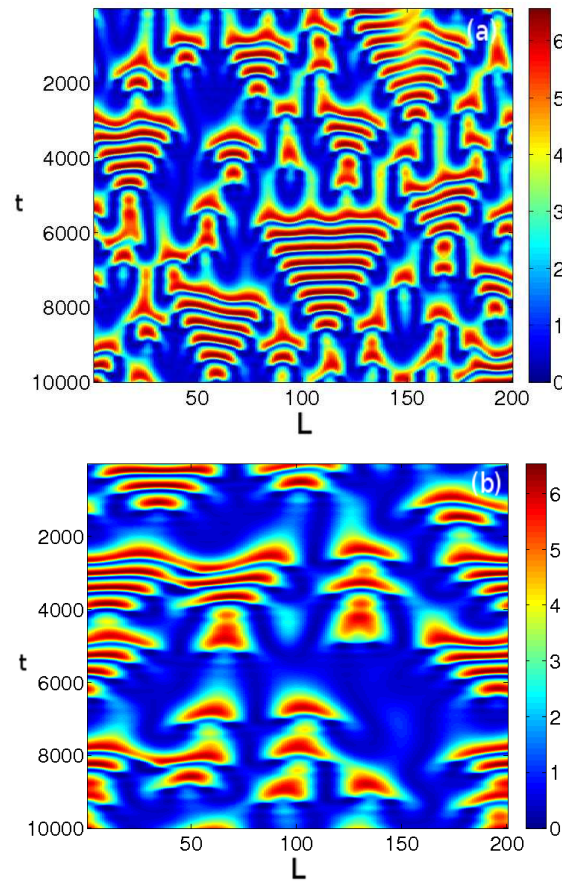
Figure 6.12: Density plot of order parameter part of shear stress. Here $\lambda_k = 1.24$, $\dot{\gamma} = 3.0$ and $\epsilon = 0.1$ (a) and 0.5 (b). Time steps (running from top to bottom) are on the y-axis, and the lattice site index ($i = 1, 200$) is on the x-axis.

haviour of two-dimensional systems due, largely, to the prohibitive computational costs involved in studying PDEs with two-dimensional spatial extent. Coupled map lattice methods provide an alternative way of addressing higher-dimensional systems, at far less attendant computational cost.

6.5.1 Local temporal behaviour

In the regular regions of the phase diagram, corresponding to the T,W, KT and KW states, the temporal behavior is very similar to that of the one dimensional case and is thus not shown separately. We thus concentrate on behavior in the complex or C region. Representative data showing the local temporal dynamics of the complex region is given in Fig (6.13). They show chaotic behaviour, and there appears to be no qualitative difference between the one dimensional and two dimensional lattice cases. As in the one-dimensional lattice, increased coupling strengths suppress the chaotic region. The log-log plot of the fourier transform is shown in Fig. (6.14); a similar fit to $P(f) \sim f^{-2}$ of the frequency spectrum of the stress can be obtained, as in the one-dimensional case.

6.5.2 Spatio-temporal behaviour

To quantify the degree of spatial coherence in 2-dimensional lattices we calculate the quantity, generalizing from the one-dimensional case studied in an earlier section:

$$\overline{d} = \sqrt{\frac{1}{N_1 N_2 T} \sum_{t=1}^{T} \sum_{i,j=1}^{N1,N2} (a_0^t(i,j) - \overline{a}^t)^2}, \qquad (6.15)$$

with

$$\overline{a} = \frac{1}{N_1 N_2} \sum_{i,j=1}^{N_1,N_2} a_0(i,j). \qquad (6.16)$$

Again, as in the 1-dimensional case, when $\overline{d}$ tends to zero the degree of synchronization of the local variables is very high. On the other hand large $\overline{d}$ indicates low spatial synchronization, and arises from a wide distribution of values of the local variables in the lattice.

Fig. (6.15) shows the space-time average of the deviation defined in Eqn. (6.15). The panel (a) displays results for $\epsilon = 0.1$ and the panel (b) for $\epsilon = 0.5$. It is clear

126
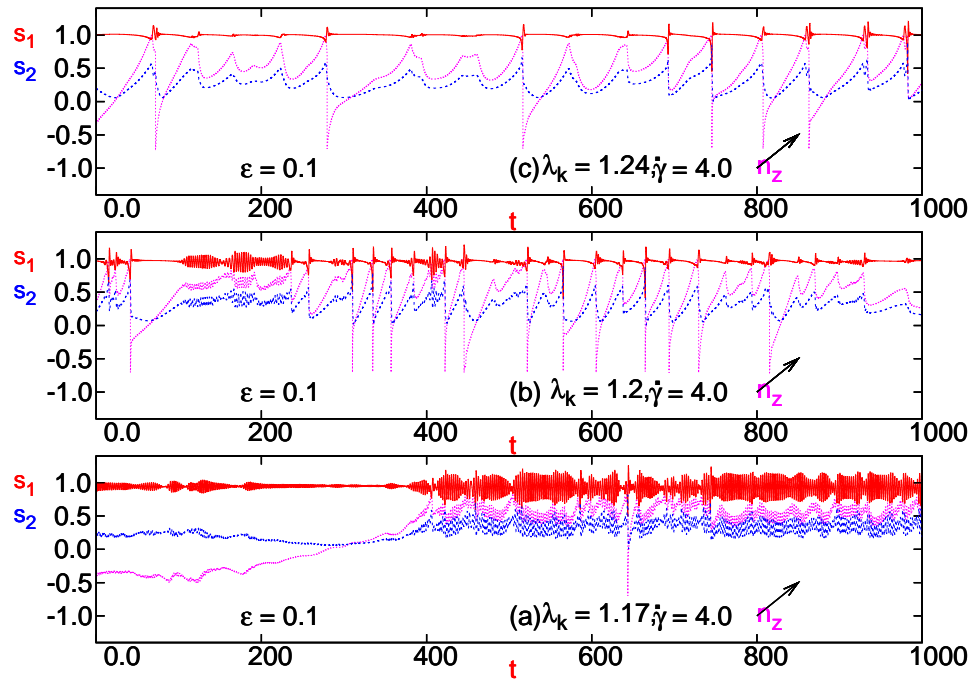
Figure 6.13: Temporal evolution of s_1, s_2 and n_z in a two dimensional lattice of size 102×102, with $\epsilon = 0.1$, for (a) $\lambda_k = 1.17$ and $\dot{\gamma} = 4.0$ (b) $\lambda_k = 1.20$ and $\dot{\gamma} = 4.0$ (c) $\lambda_k = 1.24$ and $\dot{\gamma} = 4.0$. All these state points are drawn from the C region of the local phase diagram. Note the existence of temporally intermittent behavior, analysed in terms of its frequency spectrum in Fig. 6.14.
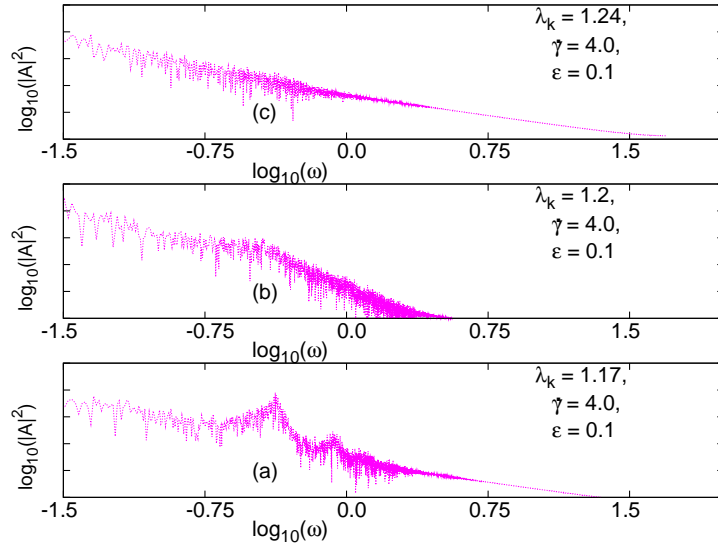
Figure 6.14: Log-Log plot of the absolute value of the Fourier transform of the stress vs. frequency ω, for (a) $\lambda_k = 1.17$, (b) $\lambda_k = 1.20$ and (c) $\lambda_k = 1.24$. Here $\epsilon = 0.1$ and $\dot{\gamma} = 4.0$. The lattice contains 100×100 sites. Note the relatively smooth background, indicating the presence of a continuous set of frequencies. The fall-off is consistent with a $1/\omega^2$ behaviour.

that higher coupling strengths make the system more uniform in space. Also, it appears that the regions with kayak-tumbling, kayak-wagging and complex local dynamical behaviour show more deviation in the spatial profile, exhibiting more spatial inhomogeneity.

Regular regime

In this section we discuss the spatial profile of our coupled map lattice in two dimensions. As in the one-dimensional case, we start with random initial conditions and analyze the space profile after omitting a transient regime. We analyse the density plots of the shear stress contribution to the order parameter, in different dynamical regions. Considering the space-time behaviour of the system in the regular region, with local dynamics belonging to the aligned, wagging, tumbling and kayak-tumbling region, reveals spatially uniformity states which are periodicity in time. These are closely related to the states obtained in the oine-dimensional case and are not discussed further here, as we will concentrate on results obtained

in the physically more interesting C regime.

Complex regime

The configurations in Figs. (6.16) is from the complex region. When the coupling becomes very large, one obtains spatially uniform states. In Fig. 6.17, we have chosen points (a) and (b) from the KT region of the local phase diagram and (c) from the C dynamical region. After leaving 10^4 transient steps , we have plotted one row of a 100×100 lattice at a single time instant. On the x axis we plot ϵ and on the y axis we plot the stress at 100 points of the lattice at one time step. It is evident that for high coupling strength ϵ, the system goes to a space-synchronized state. For low coupling constants, on the other hand, there is a typically wide distribution of stress values at different sites, indicating spatial inhomogeneity.

6.6   Quantifying Spatio-Temporal Complexity

In this section, we report results quantifying spatio-temporal complexity in the one-dimensional coupled map lattice specified in Eq. 6.6. To understand the nature of the complex behaviour represented in the phase diagram, we perform calculations of the spectrum of Lyapunov exponents. These are shown in Fig. 6.18. We first choose several values of the parameters λ_k and $\dot{\gamma}$ within the complex region and evolve the coupled map. After waiting for an initial number of time steps to eliminate transients, we calculate the Jacobian matrix at each time step. We then consider a small deviation from the attractor and iteratively multiply this deviation by the Jacobian, orthonormalizing this vector at each time step. From this we calculate the Lyapunov exponent, using the method described in Ref. [85].

These results are illustrated in Fig. 6.18, which exhibits the values of the first four Lyapunov exponents, computed for parameter values λ_k and $\dot{\gamma}$ for system sizes $L = 3, 10, 50$ and 100, as a function of the coupling constant ϵ. Our results, following the data shown in these figures, are the following. Qualitatively, in the complex regime, the first Lyapunov exponent is always positive, even as the system size and the spatial coupling are increased. The local value of this exponent is also positive. This value decreases further with spatial coupling but remains positive. Roughly speaking, larger lattice sizes show larger values for this exponent,
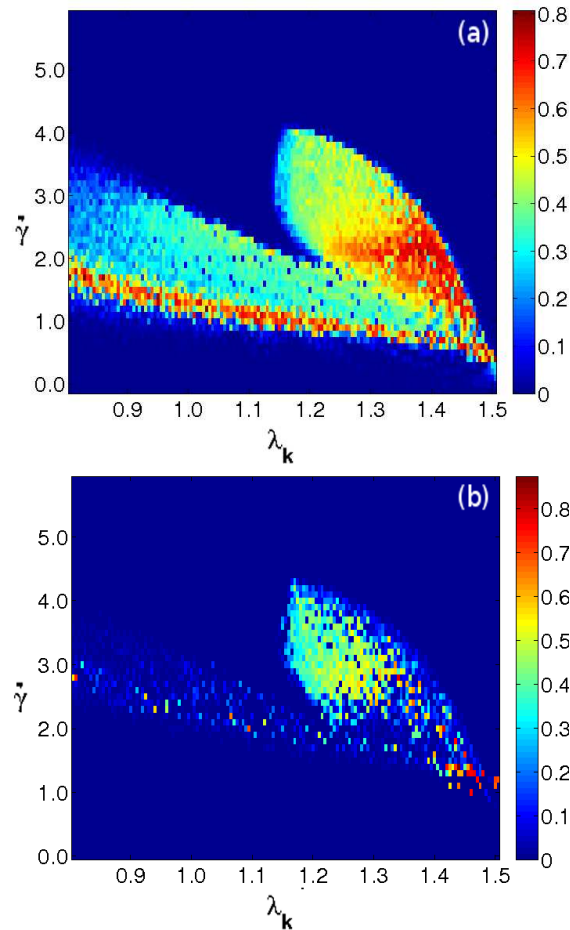
Figure 6.15: Average deviation $\overline{d}$ (see text) from the mean value of a_0 for $\epsilon = 0.1$(a) and $\epsilon = 0.5$(b). The quantity λ_k is plotted on the x-axis and $\dot{\gamma}$ on the y-axis. The lattice is a 100×100-site lattice. Note that this roughness is largest in the KT, KW and C regions, especially for large values of $\dot{\gamma}$. As ϵ is increased, the roughness decreases, as increasing spatial homogeneity is promoted.
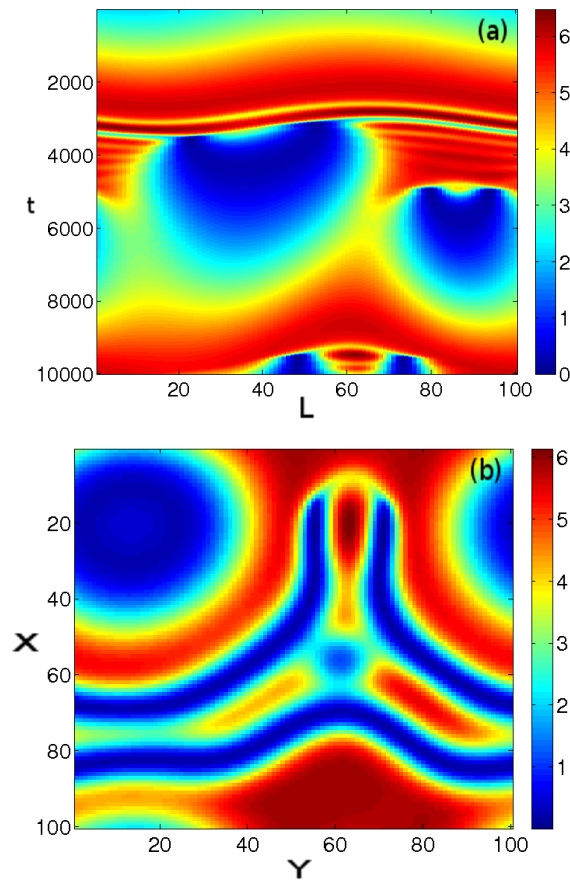
Figure 6.16: (a) A color plot of order parameter part of shear stress. The quantities
$\lambda_k = 1.25$, $\dot{\gamma} = 4.0$ and $\epsilon = 0.1$. The time t is plotted on the y-axis, which depicts
the time evolution of the stress computed on one row (x-axis) of the 100×100
lattice. (b) shows a snap shot of the full lattice at an intermediate time step.
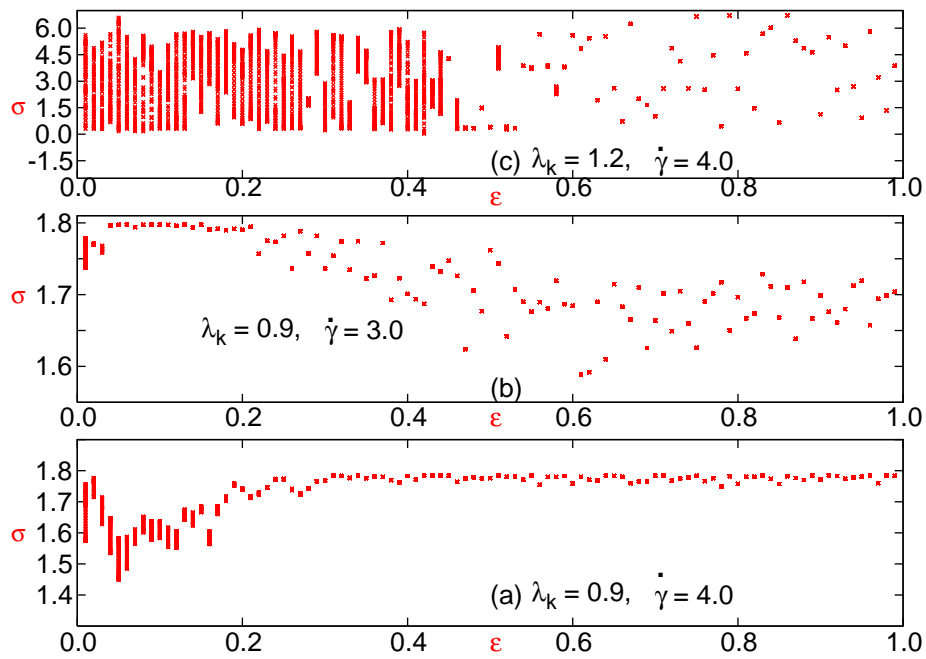
Figure 6.17: Value of stress of one row of the lattice at one instant of time on the
y axis as a function of the coupling strength ϵ on the x axis. Note that the broad
spectrum of local stress values seen at small values of the coupling contract to an
essentially unique value at large ϵ.
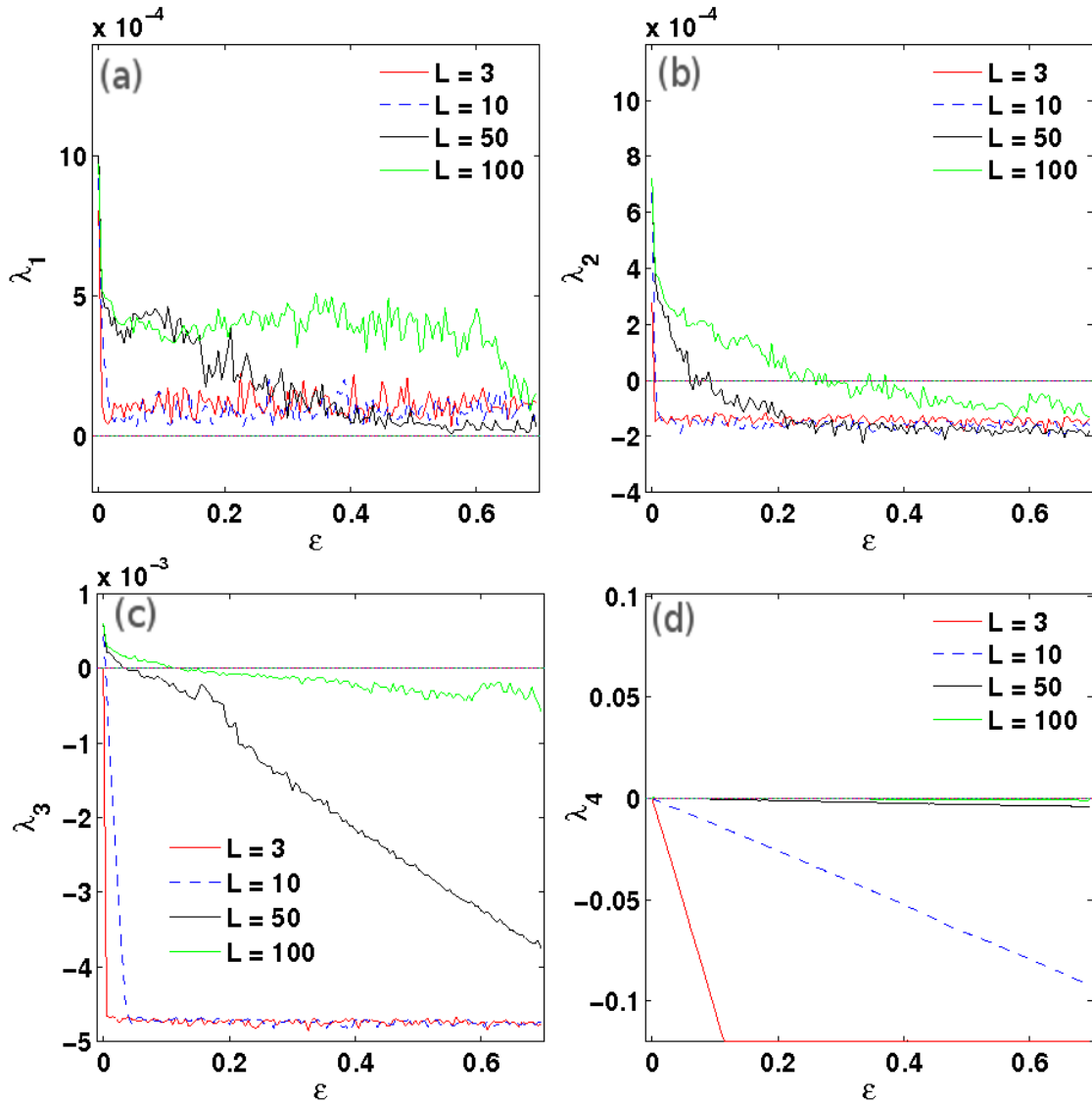
Figure 6.18: Plots of the Lyapunov exponents obtained from our calculation (see text) for different system sizes as a function of the coupling constant. The figures represent (a) the first Lyapunov exponent λ_1 (b) the second Lyapunov exponent λ_2 c) the third Lyapunov exponent λ_3 d) the fourth Lyapunov exponent λ_4. Note that all these exponents tend to zero from below in the limit of large system size. Hence, increasing the coupling between sites has the effect of reducing the magnitude of the negative Lyapunov exponent.

consistent with results from the one-dimensional PDE calculation. These values
appear to saturate for small coupling values but decrease for larger values of the
spatial coupling.

The second and higher order Lyapunov exponents, in our calculation, are small
and *negative* for the smallest lattice sizes, but move to values that are close to zero
as the lattice size is increased. At small couplings, for the larger lattices, this value
is positive but goes negative as the coupling strength is increased. Thus, the data
for the Lyapunov exponents are consistent with the general conclusion that going
to larger lattice sizes stabilizes chaos, whereas increasing the coupling between
sites suppresses complex spatial behaviour. The clustering of Lyapunov exponents
around zero in the large system size limit is consistent with the emergence of
spatio-temporal intermittency on large scales [28, 7, 65].

Kaplan-Yorke Lyapunov Dimension: J. Kaplan and J. A. Yorke [74] have
conjectured that the dimension of a strange attractor can be approximated from the
spectrum of Lyapunov exponents. Such a dimension has been called the Kaplan-
Yorke (or Lyapunov) dimension, and it has been shown that this dimension is
close to other dimensions such as the box-counting, information, and correlation
dimensions for typical strange attractors (Frederickson et al. 1983). We calcu-
lated the Kaplan-Yorke Lyapunov Dimension, defined in terms of the Lyapunov
exponents λ_i, $i = 1, 2, \ldots N$ (where the subscript labeling the λ's is chosen so that
$\lambda_1 \geq \lambda_2, \lambda_3, \ldots \lambda_N$) as:

$$D_L = k + \frac{\sum_{i=1}^{k} \lambda_i}{|\lambda_{k+1}|}. \tag{6.17}$$

Here, k is the maximum value of i, such that $\lambda_1 + \lambda_2 \cdots + \lambda_k > 0$.

From Fig. 6.19, it appears that both the number of positive Lyapunov ex-
ponents, as well as the Kaplan-Yorke (Lyapunov) dimension, scale linearly with
increasing system size, *i.e.* they are "extensive quantities". We thus conclude that
up to the system sizes we explore, the chaos is *extensive* [127]. It is also evident
that both the Kaplan-Yorke dimension and the number of positive Lyapunov ex-
ponents decrease with increasing ϵ. This again underscores the regularizing effect
of coupling interactions which induce spatial correlations, in effect reducing the
dimensionality of the system. We have also estimated the Kolmogorov-Sinai (KS)
entropy, defined as the sum of positive exponents, and observed that this too shows
a linear increase with system size.
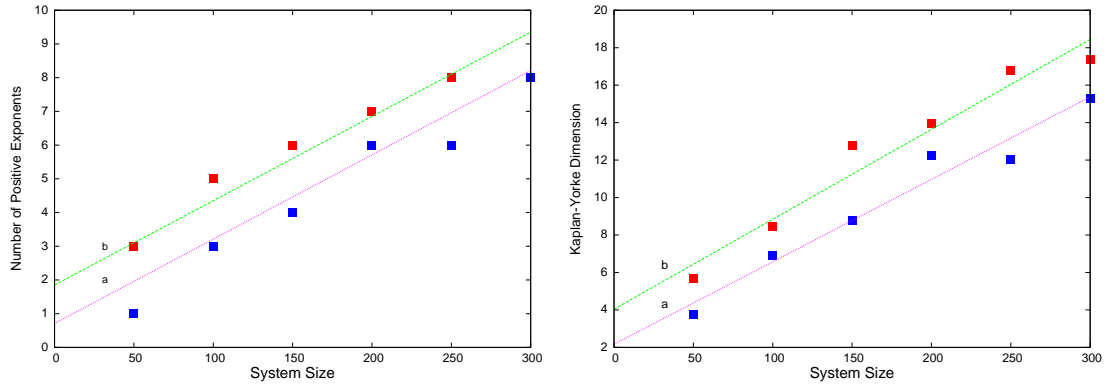
Figure 6.19: Plot of the number of positive Lyapunov Exponents (left) and Kaplan-Yorke Lyapunov dimension (right) for different system sizes, for coupling strengths : (a) $\epsilon = 0.1$ and (b) $\epsilon = 0.05$.
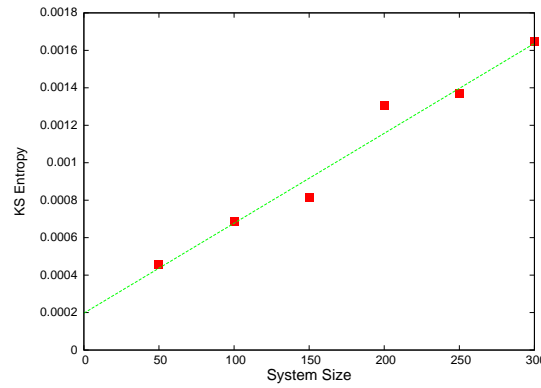
Figure 6.20: Plot of the KS Entropy for different system sizes, for coupling strength $\epsilon = 0.1$.

Further, the Kolmogorov-Sinai (KS) entropy, defined as the sum of positive exponents, can also be estimated. This too shows linear increase with increasing system size (see Fig. 6.20).

6.7 Conclusions

In summary, this chapter presents a study of a coupled map lattice model constructed to study spatio-temporal aspects of rheological chaos in sheared nematic solutions. Our study was based on the construction of a local map capable of

reproducing the physics of the spatially uncoupled (equivalently, uniform) limit,
including the large variety of phases and the complex phase diagram obtained
for that case. Such maps are placed on a regular lattice and coupled diffusively
through a variety of coupling schemes, thus representing the effects of coupling
these degrees of freedom in space.

Our general approach to the problem of spatio-temporal aspects of rheological
chaos in sheared nematics can be described in the following way: We "benchmark"
our local map against ODE solutions, requiring that our choice of discretization
maintain the basic phase behaviour and phase diagram found in the ODE case.
We then use this local map as an ingredient in the construction of a coupled map
lattice. Our principal approximations in this construction are our representation of
the spatial coupling in simple terms, in that we ignore both the convective effects
of the shear as well as anisotropies arising from allowed elastic couplings in the free
energy. Crucially, we stress that we are not solving a (discretized) version of the
non-linear coupled PDE's of the original continuum problem. We study, instead, a
far simpler discrete-space problem, one in which only the simplest spatial couplings
are retained. This approach is consistent with our intuition that spatio-temporal
complexity in this problem should be understood as arising from spatially coupling,
in a straightforward, minimal manner, a local degree of freedom with the requisite
complex dynamics.

Our approximations, though severe, nevertheless constitute a powerful enough
approach to the original problem to yield, on their own, a rich spectrum of spa-
tiotemporal patterns, going far beyond the temporal diversity obtained in earlier
studies of the local behavior. A deeper understanding of pattern formation is
possible in our approach, as the emergent dynamics is naturally decomposed into
components influenced by the local behaviour and those arising from coupling in-
teractions. Thus, though our model is simple and constructive, it clarifies the
emergence of a wide range of spatiotemporal patterns in this system.

Our studies of the coupled map in both one and two dimensions indicates
that regimes of regular behaviour largely exhibit space-uniform and time-periodic
states, with the coupled dynamics roughly following the uncoupled case. We have
analysed the dynamical behaviour of the two quantities which characterize local
order in the nematic, the uniaxial s_1 and the biaxial s_2 order parameters, examining
their time evolution in the different states.

In contrast, in the complex or C region of the local phase diagram, such coupling leads to states that exhibit spatio-temporal intermittency and chaos. We have characterized such states by examining the Lyapunov spectra as well as the frequency dependence of the time series of physical quantities such as the stress. We find evidence for a broad, power-law distribution of time-scales in the problem. Further, in the complex region, one often sees a coexistence of regular (lamina) and chaotic regimes as a prelude to fully developed chaos in which dynamical fluctuations occur independently from site to site. In some regimes, periodic bands immersed in a more complex, fluctuating background are obtained, suggestive of the possibility of transient shear bands stabilized by the dynamics, a feature also present in ODE-based studies of this problem[26, 37, 27]. The basic scale of these complex dynamical patterns is alterable by changing the coupling constant, indicative of self-similarity in the spatio-temporally intermittent case. At very large values of the coupling constant, the space profile is expected to become uniform; however, for small and intermediate values of this coupling constant, the spectrum of Lyapunov exponents merges to zero, consistent with our observation of generic spatio-temporal intermittency in the weak coupling case.

We have experimented with using spatial coupling terms which represent the advective effects of the shear flow, coupled to fixed boundary conditions where the orientation and magnitude of the order parameter are fixed at the boundary. Such terms appear, at small amplitude, to mainly distort the sorts of dynamical structures obtained for the symmetric coupling state and seem to evolve smoothly from them.

The usefulness of coupled map lattice representations of the spatio-temporal dynamics of systems exhibiting chaos in their local dynamics is that such representations often provide both useful physical insights as well as are computationally easier to simulate than their PDE versions. In that sense, the problem of rheochaos in sheared nematics offers an ideal setting for CML methods, since the *local* dynamics of the sheared nematic is highly non-trivial, exhibiting a variety of temporally periodic as well as chaotic states. As shown here, the variety of non-trivial spatio-temporal behaviour exhibited by sheared nematics is very largely a consequence of simply coupling these dynamical degrees of freedom in space. The physics appears substantially independent of how precisely this spatial coupling is done, with the simple lattice model with parallel update exhibiting virtually all the behaviour of

the more complex and computationally intensive studies of the appropriate PDE's.
This, together with the specific results presented in this chapter for our coupled
map approach to rheochaos in sheared nematics, is our central conclusion.

Further, order-parameter-based models, such as the one described in this chap-
ter and in the work of Refs. [27, 26, 37], contain essential non-linear terms in the
free energy. It is these terms that are responsible for the non-trivial local dy-
namics captured in our local map as well as in the coupled map lattice. Ref. [27]
emphasizes the role of "additional complex collective dynamics" arising from such
nonlinearities which is not captured in the DJS model but is relevant to the qual-
itative nature of the intermittent and chaotic behaviour seen in this system. Such
non-linearities are naturally accounted for in our approach.

Our study of the spatio-temporal dynamics of sheared nematics using CML
methods possibly represents the first extension of such methods to the problem
of rheochaos. In contrast to previous work based on ODE's which studied only
the one-dimensional case, it is relatively easy to extend our CML methodology to
higher dimensions, even to the experimentally relevant three-dimensional case. It
would be interesting to see how, if at all, hydrodynamic effects can be incorporated
in models of this type. Whether other experimental systems of sheared complex
fluids which exhibiting rheochaos can be fruitfully analysed using similar coupled
map approaches remains to be seen.

7
Conclusions

The work described in this thesis has dealt with some problems in the statics and dynamics of nematic liquid crystals. These problems fell into two broad classes. The first class dealt with the static properties of the isotropic-nematic interface. The second class of problems involved the study of the dynamics of the order parameter for a nematic liquid crystal in an external shear flow.

In our study of the isotropic-nematic interface, results were derived for the uniaxial and biaxial profiles, specialized to the case of planar anchoring. We showed how a term in the Euler-Lagrange equations neglected in previous work contributes substantially to determining the structure of the interface. Our approach yielded close agreement with numerics for both the uniaxial and biaxial profiles. We also studied the case where a general anchoring condition is imposed on the nematic side of the interface. We used variational methods in our analysis, showing that while spatial variations of the uniaxial and biaxial order parameters are approximately confined to the neighbourhood of the interface, nematic elasticity requires that the director orientation interpolate smoothly between planar anchoring at the location of the interface and the imposed boundary condition at infinity. Our variational results were shown to agree well with numerical results as well as results from molecular simulations.

The accuracy of these results relied on the careful choice of an appropriate variational function, powerful enough to describe the variation of the strength of uniaxial and biaxial orders across the interface as well as the spatial variation of the director field. Similar variational methodologies should be useful in other contexts where both uniaxial and biaxial orders might be expected to vary strongly in space,

including close to surfaces or in the presence of external fields.

In our study of the sheared nematic, we proposed and studied a local map capable of describing the full variety of dynamical states, ranging from regular to chaotic, obtained when a nematic liquid crystal is subjected to a steady shear flow. The map was formulated in terms of a quaternion parametrization of rotations of the local frame described by the axes of the nematic director, subdirector and the joint normal to these, with two additional scalars describing the strength of ordering. Our model yielded kayaking, wagging, tumbling, aligned and coexistence states, in agreement with previous formulations based on coupled ordinary differential equations. We then went on to discuss and study a coupled map lattice model for a nematogenic fluid in a passive shear flow. Our results provided evidence for spatially and temporally uniform states, as well as states which are spatially uniform but temporally periodic. We demonstrated the presence of spatio-temporally chaotic behaviour in some regimes, and a detailed characterization of such behavior was provided.

The work described in this thesis shows that coupled map lattice models of rheological chaos can provide accurate yet computationally tractable descriptions of the steady states of a prototypical driven complex fluids. This work provides the first example of coupled-map lattice methods applied to the problem of rheochaos. One might expect that CML models could provide helpful insights into the dynamical behaviour of other driven complex fluids known to exhibit chaotic behaviour at low Reynolds number. This would be a fruitful direction for future work.

Bibliography

[1] *Theory and Application of Coupled Map Lattices.* (ed. by K. Kaneko), 1993.

[2] Focus issue on coupled map lattices (ed. by k. kaneko). *Chaos*, **2**, 1993.

[3] M. Abramowitz and I. A. Stegun. *Handbook of Mathematical Functions: with Formulas, Graphs, and Mathematical Tables.* Dover, 1964.

[4] Muataz S. Al-Barwani and Michael P. Allen. Isotropic-nematic interface of soft spherocylinders. *Phys. Rev. E*, **62**(5):6706–6710, Nov 2000.

[5] Michael P. Allen. Molecular simulation and theory of the isotropicânematic interface. *The Journal of Chemical Physics*, **112**:5447, Dec 2000.

[6] S. L. Altmann. Rotations, Quaternions, and Double Groups. Dover Publications, 1986.

[7] G. Ananthakrishna and M. S. Bharathi. Dynamical approach to the spatiotemporal aspects of the portevin–le chatelier effect: Chaos, turbulence, and band propagation. *Phys. Rev. E*, **70**(2):026111, Aug 2004.

[8] V. J. Anderson, J. R. A. Pearson, and E. S. Boek. *The Rheolgy of Worm-like Micellar Fluids. Rheology Reviews*, pages 217 –253, 2006.

[9] A. Aradian and M. E. Cates. Minimal model for chaotic shear banding in shear thickening fluids. *Phys. Rev. E*, **73**(4):041508, Apr 2006.

[10] R. Bandyopadhyay and A. K. Sood. Chaotic dynamics in shear-thickening surfactant solutions. *Europhys Lett*, **56**:447–453, 2001.

[11] Ranjini Bandyopadhyay, Geetha Basappa, and A. K. Sood. Observation of chaotic dynamics in dilute sheared aqueous solutions of ctat. *Phys. Rev. Lett.*, **84**(9):2022–2025, Feb 2000.

[12] M. A. Bates and C. Zannoni. A molecular dynamics simulation study of the nematic-isotropic interface of a gay-berne liquid crystal. *Chemical Physics Letters*, **280**:40, November 1997.

[13] J.-F. Berret, D. C. Roux, and G. Porte. Isotropic-to-nematic transition in wormlike micelles under shear. *Journal de Physique II*, **4**:1261–1279, August 1994.

[14] J.-F. Berret, D. C. Roux, G. Porte, and P. Lindner. Tumbling Behaviour of Nematic Worm-like Micelles under Shear Flow. *Europhysics Letters*, **32**:137–142, October 1995.

[15] Jean-Fran çois Berret, Grégoire Porte, and Jean-Paul Decruppe. Inhomogeneous shear flows of wormlike micelles:ma master dynamic phase diagram. *Phys. Rev. E*, 55(2):1668–1676, Feb 1997.

[16] A. Bhardwaj, E. Miller, and J. P. Rothstein. *Filament streching and capillary breakup extentional rheometry measurements of viscoelastic wormlike micelle solution. J.Rheol.*, **51**(4):693–719., 2007.

[17] A. K. Bhattacharjee, Gautam I. Menon, and R. Adhikari. Numerical method of lines for the relaxational dynamics of nematic liquid crystals. *Phys. Rev. E*, **78**(2):026707, Aug 2008.

[18] Philippe Boltenhagen, Yuntao Hu, E. F. Matthys, and D. J. Pine. Observation of bulk phase separation and coexistence in a sheared micellar solution. *Phys. Rev. Lett.*, **79**(12):2359–2362, Sep 1997.

[19] M. E. Cates. *Reptation of living polymers: Dynamics of entangled polymers in the presence of reversible chain-scission reactions. Macromol.*, **20**:2289–2296., 1987.

[20] M. E. Cates. Nonlinear viscoelasticity of wormlike micelles (and other reversibly breakable polymers). *J. Phys. Chem.*, **94**(1):371–375, January 1990.

[21] M. E. Cates. *Slow Relaxations and Nonequilibrium Dynamics in Condensed Matter,Les Houches Session LXXVII*. Springer, New York, 2003.

[22] M. E. Cates and S. J. Candau. *Statics and dynamics of worm-like surfactant micelles. J. Phys.: Condens. Matter*, **2**:6869–6892., (1990).

[23] M. E. Cates and S. M. Fielding. Rheology of giant micelles. *Advances in Physics*, **55**(7-8):799–879, December 2006.

[24] S. Chadrasekhar. *Liquid Crystals.* Cambridge University Press, 1977.

[25] P.M. Chaikin and T.C. Lubensky. *Principles of Condensed Matter Physics.* Cambridge University Press, first edition, 1995.

[26] Buddhapriya Chakrabarti, Moumita Das, Chandan Dasgupta, Sriram Ramaswamy, and A. K. Sood. Spatiotemporal rheochaos in nematic hydrodynamics. *Phys. Rev. Lett.*, **92**(5):055501, Feb 2004.

[27] D. Chakraborty, C. Dasgupta, and A. K. Sood. Banded spatiotemporal chaos in sheared nematogenic fluids. *ArXiv e-prints*, February 2010.

[28] H. Chate. Lyapunov Analysis of Spatiotemporal Intermittency. *Europhys Lett*, **21**:419, 1993.

[29] H. Chate and M. Courbage. *Lattice Dynamics. Physica D*, **103**:1–612, 1997.

[30] J. R. Chazottes and B. Fernandez. *The CML2004 Project, Lect. Notes Phys.* . Springer, Berlin Heidelberg, 2005.

[31] Zheng Yu Chen. Biaxial effect at an isotropic-nematic interface. *Phys. Rev. E*, **47**(5):3765–3767, May 1993.

[32] Zheng Yu Chen and Jaan Noolandi. Numerical solution of the onsager problem for an isotropic-nematic interface. *Phys. Rev. A*, **45**(4):2389–2392, Feb 1992.

[33] P. E. Cladis and W. Van Saarloos. Solitons in Liquid Crystals. Springer, New York, 1992.

[34] T. M. Clausen, P. K. Vinson, J. R. Minter, H. T. Davis, Y. Talmon, and W. G. Miller. *Viscoelastic micellar solutions: Microscopy and rheology. J. Phys. Chem.*, **96**:474–484., (1992).

[35] Michel Cloitre, Régis Borrega, and Ludwik Leibler. Rheological aging and rejuvenation in microgel pastes. *Phys. Rev. Lett.*, **85**(22):4819–4822, Nov 2000.

[36] Kaneko K. Crutchfield J. P. *Phenomenolgy of spatio-temporal chaos* in:. *Direction in Chaos, 1987*, (ed. Hao Bai-lin):272–353.

[37] Moumita Das, Buddhapriya Chakrabarti, Chandan Dasgupta, Sriram Ramaswamy, and A. K. Sood. Routes to spatiotemporal chaos in the rheology of nematogenic fluids. *Phys. Rev. E*, **71**(2):021707, Feb 2005.

[38] P. G. de Gennes. Short range order effects in the isotropic phase of nematics and cholesterics. *Molecular Crystals and Liquid Crystals*, **12**:193–214, 1971.

[39] P. G. de Gennes and J. Prost. *The Physics of Liquid Crystals*. Clarendon Press, Oxford, second edition, 1993.

[40] Jan K. G. Dhont and Wim J. Briels. *Gradient and vorticity banding. Rheol Acta*, **47**:257–281, 2008.

[41] O. Diat, D. Roux, and F. Nallet. Effect of shear on a lyotropic lamellar phase. *Journal de Physique II*, **3**:1427–1452, September 1993.

[42] M. Doi. Molecular dynamics and rheological properties of concentrated solutions of rodlike polymers in isotropic and liquid crystalline phases. *Journal of Polymer Science B Polymer Physics*, **19**:229–243, February 1981.

[43] M. Doi and S. F. Edwards. The Theory of Polymer Dynamics. Clarendon Press, Oxford, 1986.

[44] C. A. Dreiss. *Wormlike micelles: where do we stand? Recent developments, linear rheology and scattering techniques. Soft matter*, **3**:956–970., 2007.

[45] G. Porte E. Eiser, F. Morino and X. Pithon. Flow in micellar cubic crystals. *Rheol. Acta*, **39**:201–208, 2000.

[46] S. Faetti and V. Palleschi. *J. Physique Lett.*, **45**:313, 1984.

[47] S. M. Fielding. *Complex dynamics of shear banded flows. Soft Matter*, **3**:1262–1279, 2007.

[48] S. M. Fielding and P. D. Olmsted. Flow phase diagrams for concentration-coupled shear banding. *Eur. Phys. J. E.*, **11**:65, 2003.

[49] S. M. Fielding and P. D. Olmsted. Spatiotemporal oscillations and rheochaos in a simple model of shear banding. *Phys. Rev. Lett.*, **92**(8):084502, Feb 2004.

[50] S. M. Fielding and P. D. Olmsted. Nonlinear dynamics of an interface between shear bands. *Phys. Rev. Lett.*, **96**(10):104502, Mar 2006.

[51] Rajesh Ganapathy, Govindan Rangarajan, and A. K. Sood. Granger causality and cross recurrence plots in rheochaos. *Phys. Rev. E*, 75(1):016211, Jan 2007.

[52] Rajesh Ganapathy and A. K. Sood. Intermittency route to rheochaos in wormlike micelles with flow-concentration coupling. *Phys. Rev. Lett.*, **96**(10):108301, Mar 2006.

[53] E. F. Gramsbergen, L. Longa, and W. H. de Jeu. Landau theory of the nematic-isotropic phase transition. *Physics Reports*, **135**:195–257, 1986.

[54] R. Granek and M. E. Cates. *Stress relaxation in living polymers: Results from a Poisson renewal model. J. Chem. Phys.*, **96**:4758–4767., 1992.

[55] S. R. De Groot and P. Mazur. *Non-Equuilibrium Thermodynamics*. North-Holland Publishing Company, 1962.

[56] M. Grosso, R. Keunings, S. Crescitelli, and P. L. Maffettone. Prediction of chaotic dynamics in sheared liquid crystalline polymers. *Phys. Rev. Lett.*, **86**(14):3184–3187, Apr 2001.

[57] Claudia Schmidt Gudrun Schmidt, Stefan Müller and Walter Richtering. Rheo-optical investigations of lyotropic mesophases of polymeric surfactants . *Rheol. Acta*, **38**:486–494, 1999.

[58] M. Liu H. Pleiner and H. R. Brand. Convective nonlinearities for the orientational tensor order parameter in polymeric systems. *Rheol. Acta*, **41**:375–382, 2002.

[59] J. Mewis V. Abetz J. W. van Egmond H. Yanase, P. Moldenaers and G. G. Fuller. Structure and dynamics of a polymer solution subject to flow-induced phase separation. *Rheol. Acta*, **30**:89–97, 1991.

[60] John P. Heller and Murty S. Kuntamukkula. Critical review of the foam rheology literature. *Ind. Eng. Chem. Res.*, **26**(2):318–325, 1987.

[61] S. Hess. Fokker-Planck-Equation Approach to Flow Alignment in Liquid Crystals. *Zeitschrift Naturforschung Teil A*, **31**:1034–+, 1976.

[62] S. Hess and I. Pardowitz. On the Unifed Theory for Non-Equilibrium Phenomena in the Isotropic and NEmatic Phases of a Liquid Crystal; Spatially Inhomogeneous Alignment. *Zeitschrift Naturforschung Teil A*, **36**:554–+, 1981.

[63] R. Holyst and A. Poniewierski. Director orientation at the nematic-phase–isotropic-phase interface for the model of hard spherocylinders. *Phys. Rev. A*, **38**(3):1527–1533, Aug 1988.

[64] J. Israelachvili. *Intermolecular and Surface Forces*. Academic Press, London, second edition, 1992.

[65] Zahera Jabeen and Neelima Gupte. Spatiotemporal intermittency and scaling laws in the coupled sine circle map lattice. *Phys. Rev. E*, **74**(1):016210, Jul 2006.

[66] S. M. Kamil, A. K. Bhattacharjee, R. Adhikari, and Gautam I. Menon. Biaxiality at the isotropic-nematic interface with planar anchoring. *Phys. Rev. E*, **80**(4):041705, Oct 2009.

[67] S. M. Kamil, Sudeshna Sinha, and Gautam I. Menon. Regular and chaotic states in a local map description of sheared nematic liquid crystals. *Phys. Rev. E*, **78**(1):011706, Jul 2008.

[68] K Kaneko. Period doubling of kink-antikink patterns, quasiperiodicity in antiferro-like structures and spatial intermittency in coupled map lattices. *Prog. Theor. Phys.*, **72**:480–486, 1984.

[69] K Kaneko. Spatial period-doubling in open flow. *Phys. Lett. A*, **111**:321–325, 1985.

[70] K. Kaneko. Spatiotemporal Intermittency in Coupled Map Lattices. *Progress of Theoretical Physics*, 74:1033–1044, November 1985.

[71] K. Kaneko. Pattern dynamics in spatiotemporal chaos Pattern selection, diffusion of defect and pattern competition intermettency. *Physica D Nonlinear Phenomena*, 34:1–41, January 1989.

[72] K. Kaneko and I. Tsuda. *Chaos and Beyond.* Springer, Berlin, 2000.

[73] Kyongok Kang, M. Paul Lettinga, and Jan K. G. Dhont. *Is vorticity-banding due to an elastic instability? Rheol Acta*, **47**:499–508, 2008.

[74] J. Kaplan and J. A. Yourk. *Springer Lecture Notes in Mathematics.* **730**(204), 1979.

[75] R. Kapral. Pattern formation in two-dimensional arrays of coupled discrete time oscillators. *Phys. Rev. A*, **31**:3868–3879, 1985.

[76] F. Kern, P. Lemarechel, S. J. Candau, and M. E. Cates. *Rheological Properties of Semidilute and Concentrated Aqueous Solutions of Cetyltrimethylammonium Bromide in the Presence of Potassium Bromide. Langmuir*, **8**:437–440., (1992).

[77] F. Kern, F. Lequeux, R. Zana, and S. J. Candau. *Dynamics properties of salt-free viscoelastic micellar solutions. Langmuir*, **10**:1714–1723., (1994).

[78] M. Kleman and O. Lavrentovich. *Soft Matter Physics: An Introduction.* Springer Verlag, New York, 2002.

[79] H. J. Kreuzer. *Nonequilibrium thermodynamics and its statistical foundations.* 1981.

[80] S. P. Kuznetsov. On critical behaviour of one-dimensional lattices. *Pis'ma J. Technich. Fiz.*, **9**:94–98, 1983.

[81] S. P. Kuznetsov. On model description of coupled dynamical systems near the transition point order-disorder. *Izv. VUZov-Fizika*, **27**:87–96, 1984.

[82] N. Kuzuu and M. Doi. Constitutive Equation for Nematic Liquid Crystals under Weak Velocity Gradient Derived from a Molecular Kinetic Equation. *Journal of the Physical Society of Japan*, **52**:3486–+, October 1983.

[83] B. J. Ackerson C. F. Zukoski L. B. Chen, M. K. Chow. Rheological and Microstructural Transitions in Colloidal Crystals. *Langmuir*, **10**(8):2817–2829, 1994.

[84] I. Tucker J. Penfold L. Soubiran, E. Staples and A. Creeth. Effects of Shear on the Lamellar Phase of a Dialkyl Cationic Surfactant. *Langmuir*, **17**(26):7988–7994, 2001.

[85] M. Lakshmanan and S. Rajasekar. *Nonlinear Dynamics*. Springer-Verlag, 2003.

[86] D. Langevin and Bouchiat M. A. Molecular order and surface tension for the nematic-isotropic interface of mbba, deduced from light reflectivity and light scattering measurements. *Mol. Cryst. Liq. Cryst.*, **22**:331, 1973.

[87] R. G. Larson. *The Structure and Rheology of Complex Fluids*. Oxford University Press, Oxford, 1999.

[88] A. W. Lees and S. F. Edwards. The computer study of transport processes under extreme conditions. *Journal of Physics C Solid State Physics*, **5**:1921–1928, August 1972.

[89] Sandra Lerouge and Jean-Francois Berret. *Shear-induced transitions and instabilities in surfactant wormlike micelles.* *arXiv:***0910.1854v1**, [cond-mat.soft], 9 Oct. 2009.

[90] T. C. B. McLeish M. E. Cates and G. Marrucci. The rheology of entangled polymers at very high shear rates. *Europhys Lett*, **21**:451, 1993.

[91] Andrew J. McDonald, Michael P. Allen, and Friederike Schmid. Surface tension of the isotropic-nematic interface. *Phys. Rev. E*, **63**(1):010701, Dec 2000.

[92] K. Migler, C.-H. Liu, and D. J. Pine. Structure Evolution of a Polymer Solution at High Shear Rates. *Macromolecules*, **29**:1422–1432, January 1996.

[93] R Miyazaki, S. Yoshida, Y. Dobashi, and T. Nishita. *Proc. of Pacific Graphics*, pages 363–372, 2001.

148

[94] Brian G. Moore and William E. McMullen. Isotropic-nematic interface of hard spherocylinders: Beyond the square-gradient approximation. *Phys. Rev. A*, **42**(10):6042–6051, Nov 1990.

[95] P. Mukerjee. *J. Phys. Chem*, **76**(565), 1972.

[96] Peter D. Olmsted. Perspectives on shear banding in complex fluids. *Rheol. Acta*, **47**:283–300, 2008.

[97] Peter D. Olmsted and Paul Goldbart. Theory of the nonequilibrium phase transition for nematic liquid crystals under shear flow. *Phys. Rev. A*, **41**(8):4578–4581, Apr 1990.

[98] Peter D. Olmsted and C.-Y. D. Lu. Coexistence and phase separation in sheared complex fluids. *Phys. Rev. E*, **56**(1):R55–R58, Jul 1997.

[99] L. Onsager. Reciprocal Relations in Irreversible Processes. I. *Physical Review*, **37**:405–426, February 1931.

[100] L. Onsager. Reciprocal Relations in Irreversible Processes. II. *Physical Review*, **38**:2265–2279, December 1931.

[101] Y. Oono and S. Puri. Study of phase-separation dynamics by use of cell dynamical systems. i. modeling. *Phys. Rev. A*, **38**(1):434–453, Jul 1988.

[102] C. Pereira Borgmeyer and S. Hess. Unified Description of the Flow Alignment and Viscosity in the Isotropic and Nematic Phases of Liquid Crystals. *Journal of Non Equilibrium Thermodynamics*, **20**:359–384, January 1995.

[103] A. C. Pipkin and R. I. Tauner. Mechanics today. 1972.

[104] V. Popa-Nita and T. J. Sluckin. Kinetics of the nematic-isotropic interface. *J. Phys. II (France)*, **6**:873–884, 1996.

[105] V. Popa-Nita, T. J. Sluckin, and A. A. Wheeler. Statics and kinetics at the nematic-isotropic interface: Effects of biaxiality. *J. Phys. II (France)*, **7**:1225–1243, 1997.

[106] G. Porte, J.-F. Berret, and J. L. Harden. Inhomogeneous Flows of Complex Fluids: Mechanical Instability Versus Non-Equilibrium Phase Transition. *Journal de Physique II*, **7**:459–472, March 1997.

[107] Tiezheng Qian and Ping Sheng. Generalized hydrodynamic equations for nematic liquid crystals. *Phys. Rev. E*, **58**(6):7475–7485, Dec 1998.

[108] G. Basappa R. Bandyopadhyay and A. K. Sood. Linear and nonlinear rheology of wormlike micelles. *Pramana*, **53**:223–235, 1999.

[109] S. R. Raghavan, G. Fritz, and E. W. Kaler. *Wormlike micelles formed by synergistic self-assembly in mixtures of anionic and cationic surfactants. Langmuir*, **18**:3797–3803., (2002).

[110] H. Rehage and Hoffmann H. *Rheological Properties of viscoelastic surfactan Systems. J. of Phys. Chem.*, **92**:4712–4719., 1988.

[111] H. Rehage and H. Hoffmann. *Viscoelastic surfactant solutions: model systems for rheologycal research. Mol. Phys*, **74**(5):933–973., 1991.

[112] Götz Rienäcker, Martin Kröger, and Siegfried Hess. Chaotic orientational behavior of a nematic liquid crystal subjected to a steady shear flow. *Phys. Rev. E*, **66**(4):040702, Oct 2002.

[113] G. Rienäcker, M. Kröger, and S. Hess. Chaotic and regular shear-induced orientational dynamics of nematic liquid crystals. *Physica A: Statistical Mechanics and its Applications*, **315**(3-4):537 – 568, 2002.

[114] J. P. Rothstein. *Transient extensional rheology of wormlike micelle solutions. J.Rheol.*, **47**(5):1227–1247., (2003).

[115] J. P. Rothstein. *Strong flows of viscoelastic wormlike micelle solutions. Rheology Reviews*, 2009.

[116] C. R. Safinya, E. B. Sirota, and R. J. Plano. Nematic to smectic-a phase transition under shear flow: A nonequilibrium synchrotron x-ray study. *Phys. Rev. Lett.*, **66**(15):1986–1989, Apr 1991.

[117] Jean-Baptiste Salmon, Annie Colin, and Didier Roux. Dynamical behavior of a complex fluid near an out-of-equilibrium transition: Approaching simple rheological chaos. *Phys. Rev. E*, **66**(3):031505, Sep 2002.

[118] R. L. Scott. *J. Phys. Chem*, **69**(261), 1965.

[119] A. K. Sen and D. E. Sullivan. Landau–de gennes theory of wetting and orientational transitions at a nematic-liquid– substrate interface. *Phys. Rev. A*, **35**(3):1391–1403, Feb 1987.

[120] T. Shikata, H. Hirata, and T. Kotaka. *Micelle Formation of Detergent Molecules in Aqueous-Media- Viscoelastic Properties of Aqueous Cetyltrimethylammonium Bromide Solutions*. Langmuir, **3**(6):1081–1086., (1987).

[121] T Shikata and T Kotaka. *Entanglement network of thread-like micelles of a cationic detergent. J. Non-Crystal. Sol. 131 -133*, pages 831–835., (1991).

[122] K. Shundyak and R. van Roij. Isotropic-nematic interfaces of hard-rod fluids. *Journal of Physics Condensed Matter*, 13:4789–4800, May 2001.

[123] André M. Sonnet and Epifanio G. Virga. Dynamics of dissipative ordered fluids. *Phys. Rev. E*, **64**(3):031705, Aug 2001.

[124] N. A. Spenley, M. E. Cates, and T. C. B. McLeish. Nonlinear rheology of wormlike micelles. *Phys. Rev. Lett.*, **71**(6):939–942, Aug 1993.

[125] N. A. Spenley, X. F. Yuan, and M. E. Cates. Nonmonotonic Constitutive Laws and the Formation of Shear-Banded Flows. *Journal de Physique II*, **6**:551–571, April 1996.

[126] H. Stark and T. C. Lubensky. Poisson-bracket approach to the dynamics of nematic liquid crystals. *Phys. Rev. E*, **67**(6):061709, Jun 2003.

[127] Shigeyuki Tajima and Henry S. Greenside. Microextensive chaos of a spatially extended system. *Phys. Rev. E*, 66(1):017205, Jul 2002.

[128] Lloyd N. Trefethen. *Spectral Methods in Matlab*. SIAM, 2000.

[129] E. Velasco, L. Mederos, and D. E. Sullivan. Density-functional study of the nematic-isotropic interface of hard spherocylinders. *Phys. Rev. E*, **66**(2):021708, Aug 2002.

[130] R. L. C. Vink and T. Schilling. Interfacial tension of the isotropic-nematic interface in suspensions of soft spherocylinders. *Phys. Rev. E*, **71**(5):051716, May 2005.

[131] I. Waller and K. Kapral. Spatial and temporal structure in systems of coupled nonlinear oscillators. *Phys. Rev. A*, **30**:2047–2055, 1984.

[132] J. A. C. Weidemann and S. C. Reddy. *ACM Transactions on Mathematical Software*, **26**:465, 2000.

[133] Elizabeth K. Wheeler, Peter Fischer, and Gerald G. Fuller. Time-periodic flow induced structures and instabilities in a viscoelastic surfactant solution. *Journal of Non-Newtonian Fluid Mechanics*, **75**(2-3):193 – 208, 1998.

[134] S. Wolfsheimer, C. Tanase, K. Shundyak, R. van Roij, and T. Schilling. Isotropic-nematic interface in suspensions of hard rods: Mean-field properties and capillary waves. *Phys. Rev. E*, **73**(6):061703, Jun 2006.

[135] Tatsuo Yanagita and Kunihiko Kaneko. Modeling and characterization of cloud dynamics. *Phys. Rev. Lett.*, 78(22):4297–4300, Jun 1997.

[136] J. Yang. *Viscoelastic wormlike micelles and thier applications. Current Opinion in Colloidal and Interface Sci.*, **7**:276–281., 2002.

[137] J. L. Zakin, B. Lu, and N. W. Bewerdorff. *Surfactant drag reduction. Rev. Chem. Eng.*, **14**(45):253–320., 1988.